

# Introducing the Illustris Project: Simulating the coevolution of dark and visible matter in the Universe

Mark Vogelsberger<sup>1</sup>, Shy Genel<sup>2</sup>, Volker Springel<sup>3,4</sup>, Paul Torrey<sup>2</sup>, Debora Sijacki<sup>5</sup>, Dandan Xu<sup>3</sup>, Greg Snyder<sup>6</sup>, Dylan Nelson<sup>2</sup>, and Lars Hernquist<sup>2</sup>

<sup>1</sup> *Department of Physics, Kavli Institute for Astrophysics and Space Research, Massachusetts Institute of Technology, Cambridge, MA 02139, USA*

<sup>2</sup> *Harvard-Smithsonian Center for Astrophysics, 60 Garden Street, Cambridge, MA 02138, USA*

<sup>3</sup> *Heidelberg Institute for Theoretical Studies, Schloss-Wolfsbrunnengasse 35, 69118 Heidelberg, Germany*

<sup>4</sup> *Zentrum für Astronomie der Universität Heidelberg, ARI, Mönchhofstr. 12-14, 69120 Heidelberg, Germany*

<sup>5</sup> *Kavli Institute for Cosmology, Cambridge, and Institute of Astronomy, Madingley Road, Cambridge, CB3 0HA, UK*

<sup>6</sup> *Space Telescope Science Institute, 3700 San Martin Drive, Baltimore, MD 21218, USA*

27 March 2022

## ABSTRACT

We introduce the Illustris Project, a series of large-scale hydrodynamical simulations of galaxy formation. The highest resolution simulation, Illustris-1, covers a volume of  $(106.5 \text{ Mpc})^3$ , has a dark mass resolution of  $6.26 \times 10^6 M_{\odot}$ , and an initial baryonic matter mass resolution of  $1.26 \times 10^6 M_{\odot}$ . At  $z = 0$  gravitational forces are softened on scales of 710 pc, and the smallest hydrodynamical gas cells have an extent of 48 pc. We follow the dynamical evolution of  $2 \times 1820^3$  resolution elements and in addition passively evolve  $1820^3$  Monte Carlo tracer particles reaching a total particle count of more than 18 billion. The galaxy formation model includes: primordial and metal-line cooling with self-shielding corrections, stellar evolution, stellar feedback, gas recycling, chemical enrichment, supermassive black hole growth, and feedback from active galactic nuclei. Here we describe the simulation suite, and contrast basic predictions of our model for the present day galaxy population with observations of the local universe. At  $z = 0$  our simulation volume contains about 40,000 well-resolved galaxies covering a diverse range of morphologies and colours including early-type, late-type and irregular galaxies. The simulation reproduces the cosmic star formation rate density, the galaxy luminosity function, and baryon conversion efficiency at  $z = 0$ . It also qualitatively captures the impact of galaxy environment on the red fractions of galaxies. The internal velocity structure of selected well-resolved disk galaxies obeys the stellar and baryonic Tully-Fisher relation together with flat circular velocity curves. In the well-resolved regime the simulation reproduces the observed mix of early-type and late-type galaxies. Our model predicts a halo mass dependent impact of baryonic effects on the halo mass function and the masses of haloes caused by feedback from supernova and active galactic nuclei.

**Key words:** methods: numerical – cosmology: theory – cosmology: galaxy formation

## 1 INTRODUCTION

Over the last decade the amount of available astronomical data on the large-scale structure of the Universe has grown rapidly, locally, as in the the Two-degree-Field Galaxy Redshift Survey (2dFGRS) (Colless et al. 2001) and Sloan Digital Sky Survey (SDSS) (York et al. 2000), and in surveys at higher redshifts, such as DEEP (Weiner et al. 2005), DEEP2 (Davis et al. 2003) and the Cosmic Assembly Near-IR Deep Extragalactic Legacy Survey (CANDELS) (Grogin et al. 2011; Koekemoer et al. 2011). Upcoming programs and instruments like the Large Synoptic Survey Telescope (LSST) (LSST Science Collaboration et al. 2009) promise maps of the distribution and properties of galaxies in even

higher detail. This increasingly precise observational picture requires equally accurate theoretical models for understanding structure formation and the nature of dark matter (DM) and dark energy (DE) (Riess et al. 1999; Perlmutter et al. 1999). The prospects for such theoretical calculations are in principle bright, because the initial conditions for cosmic structure formation are tightly constrained through measurements of anisotropies in the cosmic microwave background radiation (Planck Collaboration et al. 2013). The  $\Lambda$  cold dark matter ( $\Lambda$ CDM) paradigm favored by these data implies that the cosmos is filled with three distinct components: baryons, DM and DE, and although the physical nature of DM and DE remain unknown, their evolution can be followed far into the non-linear regime using collisionless N-body simulations (e.g.,

Springel et al. 2005b, 2008; Boylan-Kolchin et al. 2009; Klypin et al. 2011; Angulo et al. 2012; Wu et al. 2013). However, such simulations by themselves cannot predict the distribution of galaxies made up of baryonic matter, severely limiting their utility as a means to directly connect with the observations.

There are two approaches for establishing this link: (i) Through a post-processing procedure known as semi-analytic modelling, in which the output of N-body simulations is combined with simple physical prescriptions to estimate the distribution of galaxies (e.g., White & Frenk 1991; Kauffmann et al. 1993; Somerville & Primack 1999; Cole et al. 2000; Croton et al. 2006; Bower et al. 2006; Guo et al. 2011). (ii) Through directly accounting for the baryonic component (gas, stars, supermassive black holes, etc.) in cosmological simulations that include hydrodynamics and gravity (e.g., Katz 1992; Katz et al. 1992; Bryan & Norman 1998; Davé et al. 2001; Springel et al. 2005a; Crain et al. 2009; Schaye et al. 2010; Brook et al. 2012; Khandai et al. 2014; Dubois et al. 2014), in principle offering a self-consistent and fully predictive approach. However, the vast computational challenges related to simulations of the baryonic component have thus far precluded wide-spread adoption of this approach. Large-scale predictions of the galaxy population have thus mainly been obtained with the semi-analytic method during the past few decades.

Hydrodynamical simulations of galaxy formation have become more prominent over the last several years, and a significant number of results have been published from them (e.g., Ocvirk et al. 2008; Crain et al. 2009; Schaye et al. 2010; Davé et al. 2011; McCarthy et al. 2012; Puchwein et al. 2013; Kannan et al. 2013). These cosmological simulations of the formation of representative galaxy populations are different from studies where the computational power is focused on a single galaxy (e.g., Governato et al. 2010; Agertz et al. 2011; Guedes et al. 2011; Scannapieco et al. 2012; Aumer et al. 2013; Marinacci et al. 2014a; Kim et al. 2014). Although such “zoom-in” simulations offer higher mass and spatial resolution, they do not yield a statistical sample of objects to compare to observations, which limits their ability to falsify certain model aspects. However, when used in conjunction with large-scale simulations, the zoom-in procedure is clearly essential for constructing more reliable sub-resolution models for characterising entire galaxy populations. Ideally both approaches should be pursued simultaneously to learn more about the complex problem of galaxy formation.

Hydrodynamical galaxy formation simulations typically include sub-resolution models for star formation (e.g., Ascibar et al. 2002; Springel & Hernquist 2003a; Schaye & Dalla Vecchia 2008; Dubois & Teyssier 2008; Few et al. 2012), radiative cooling processes (primordial and metal-line) (e.g., Katz et al. 1996; Wiersma et al. 2009a; Shen et al. 2010), stellar evolution and chemical enrichment procedures based on stellar synthesis calculations (e.g., Steinmetz & Mueller 1994; Mosconi et al. 2001; Lia et al. 2002; Springel & Hernquist 2003a; Kobayashi 2004; Scannapieco et al. 2005; Tornatore et al. 2007; Oppenheimer & Davé 2008; Wiersma et al. 2009b; Few et al. 2012), stellar feedback (e.g., Dekel & Silk 1986; Navarro & White 1993; Mihos & Hernquist 1994; Gerritsen & Icke 1997; Thacker & Couchman 2000; Kay et al. 2002; Kawata & Gibson 2003; Sommer-Larsen et al. 2003; Springel & Hernquist 2003a; Brook et al. 2004; Stinson et al. 2006; Dubois & Teyssier 2008; Dalla Vecchia & Schaye 2008; Okamoto et al. 2010; Piontek & Steinmetz 2011; Dalla Vecchia & Schaye 2012; Stinson et al. 2013), and feedback from active galactic nuclei (e.g., Springel et al. 2005b; Kawata & Gibson 2005; Di Matteo et al. 2005; Thacker et al. 2006; Sijacki & Springel 2006; Sijacki

et al. 2007; Di Matteo et al. 2008; Okamoto et al. 2008; Booth & Schaye 2009; Kurosawa & Proga 2009; Teyssier et al. 2011; Debuhr et al. 2011; Dubois et al. 2012). Small-scale simulations also have also included magnetic fields (e.g., Teyssier et al. 2006; Dolag et al. 2009; Collins et al. 2010; Pakmor et al. 2014), radiative transfer (e.g., Abel & Wandelt 2002; Petkova & Springel 2010; Cantalupo & Porciani 2011), cosmic ray physics (Jubelgas et al. 2008) and thermal conduction (Jubelgas et al. 2004; Dolag et al. 2004). Recently, more “explicit” forms of feedback have been included (e.g., Hopkins et al. 2013a), which require however much higher spatial and mass resolution, something which is currently out of reach for large-scale hydrodynamical simulations. Nevertheless, such detailed models might lead to new effective models, which can then be adapted for large-scale simulations.

Here we present first results of the Illustris Simulation, the most ambitious large-scale hydrodynamical calculation of structure formation to date, first described in Vogelsberger et al. (2014b). Our model incorporates a broad range of astrophysical processes that are believed to be relevant to galaxy formation (see Vogelsberger et al. 2013, for details): gas cooling with radiative self-shielding corrections, energetic feedback from growing supermassive black holes (SMBHs) and exploding supernovae (SNe), stellar evolution and associated chemical enrichment and stellar mass loss, and radiation proximity effects for active galactic nuclei (AGNs). The simulation starts at redshift  $z = 127$  ( $\sim 12$  million years after the Big Bang) and follows the evolution of  $2 \times 1820^3$  resolution elements in a volume of  $(106.5 \text{ Mpc})^3$ . We achieve a DM mass resolution of  $6.26 \times 10^6 M_\odot$ , and an initial baryonic mass resolution of  $1.26 \times 10^6 M_\odot$ . The smallest scale (corresponding to the smallest fiducial cell radius) over which the hydrodynamical Euler equations are solved with the moving-mesh technique AREPO (described in Springel 2010) is 48 pc at  $z = 0$ . The mass and spatial resolution are thus comparable to state-of-the-art large-scale N-body simulations (e.g., Boylan-Kolchin et al. 2009; Klypin et al. 2011) which do not include baryons. Further details of the redshift zero population of Illustris are presented in a companion paper (Vogelsberger et al. 2014b), where we focus on deep field mock observations, the distribution of satellites in clusters, the metal content of damped Lyman- $\alpha$  absorbers, the column density distribution of neutral hydrogen, and the impact of baryons on the total matter power spectrum. Here we extend this comparison to a broader range of observables of the local Universe. The high redshift galaxy population is discussed in another companion paper (Genel et al., in prep), where we demonstrate that many observables at high  $z$  are also reproduced by our model. Another companion paper (Sijacki et al., in prep) presents results on the population of SMBHs in Illustris.

This paper is organised as follows. In Section 2, we describe our galaxy formation model, the initial conditions and the simulation suite including post-processing procedures. Section 3 presents first results on the predicted large-scale structure focusing on the halo mass function and the impact of baryons on halo masses. The galaxy population is inspected more closely in Section 4. We demonstrate here that our model reproduces key observables of the local Universe and the cosmic star formation rate density over cosmic time. We also discuss the colours of galaxies and the impact of environment on galaxy evolution and specifically on the red fraction of galaxies. Section 5 focuses on the internal structure of galaxies based on well-resolved sample galaxies taken from the simulation, demonstrating that our model correctly predicts the velocity structure of galaxies and the morphological mix of early- and late-type galaxies. We give a detailed summary of our results in Section 6 and our conclusions in Section 7. Readers in-

interested in the main results are encouraged to read Section 6, which summarises the most significant findings of the present work. Finally, Section 8 briefly describes upcoming data releases and details about distribution of the simulation data to the community. All data distribution and project updates will be handled through <http://www.illustris-project.org>.

## 2 SIMULATION CODE AND GALAXY FORMATION MODEL

### 2.1 Simulation method

Following the dynamics of DM and gas accurately requires a highly reliable and efficient numerical scheme to solve the coupled system of partial differential equations describing gravity and hydrodynamics. We use the recently developed `AREPO` code (Springel 2010), which employs an unstructured Voronoi tessellation of the simulation volume, where the mesh-generating points of this tessellation are moved with the gas flow. The adaptive mesh is used to solve the equations of ideal hydrodynamics with a finite volume approach using a second-order unsplit Godunov scheme with an exact Riemann solver. It has been demonstrated that such an approach is typically superior to traditional smoothed particle hydrodynamics (SPH), and especially in the presence of large bulk velocities also to Eulerian adaptive mesh refinement (AMR) (Vogelsberger et al. 2012; Kereš et al. 2012; Sijacki et al. 2012; Torrey et al. 2012; Genel et al. 2013; Nelson et al. 2013). Gravitational forces are calculated using a Tree-PM scheme (Xu 1995) such that long-range forces are determined using a particle-mesh method while short-range forces are computed via a hierarchical octree algorithm (Barnes & Hut 1986).

### 2.2 Galaxy formation model

Besides calculating gravitational forces and hydrodynamical fluxes, our simulations account for astrophysical process known to be crucial for galaxy formation. The implementation is described in detail in Vogelsberger et al. (2013); Torrey et al. (2014), and we summarise the main characteristics below:

- **Gas cooling and photo-ionisation:** Gas cooling rates are calculated as a function of gas density, temperature, metallicity, the radiation fields of AGNs (see below), and the spatially uniform but time-dependent ionising background radiation from galaxies and quasars (Faucher-Giguère et al. 2009), which completes H I reionisation at a redshift of  $z \simeq 6$ . This background radiation is chosen to match constraints on the opacity of the Lyman- $\alpha$  forest (e.g., Faucher-Giguère et al. 2008b,a) and helium reionisation (e.g., McQuinn et al. 2009). Metal-line cooling is based on pre-calculated cooling rate tables using `CLOUDY` (Ferland et al. 1998). We include self-shielding corrections following Rahmati et al. (2013).

- **Star formation and physics of the interstellar medium:** We employ a numerically converged sub-resolution model of the interstellar medium (ISM) to achieve numerical closure below our resolution scale. Dense gas with hydrogen number density above  $0.13 \text{ cm}^{-3}$  follows an effective equation of state assuming that the ISM has a two-phase medium structure predominantly composed of cold clouds embedded in a tenuous, supernova (SN)-heated phase (Springel & Hernquist 2003b). We use a “softer” effective equation of state than has been sometimes employed earlier ( $q = 0.3$  instead of  $q = 1.0$ ). Star formation (SF) is based on a stochastic

prescription following the Kennicutt-Schmidt law (Kennicutt 1989) and adopting a Chabrier initial mass function (Chabrier 2003).

- **Stellar evolution, gas recycling and chemical enrichment:** Newly created stellar populations can lose mass through stellar winds and SNe, which is then returned to the gas phase and enriches the gas surrounding stellar populations. We track stellar evolution and model SNe of type Ia, type II, and the asymptotic giant branch phases of stars. We trace the evolution of nine elements in total (H, He, C, N, O, Ne, Mg, Si, Fe) each independently advected as a passive scalar. Furthermore, we also track the total amount of metals, and the total mass loss from stars.

- **Stellar SN feedback:** We employ a kinetic stellar feedback scheme, where the stellar wind velocity is scaled with the local halo environment ( $3.7 \sigma_{\text{DM}}^{\text{1D}}$ , where  $\sigma_{\text{DM}}^{\text{1D}}$  is the local one-dimensional DM velocity dispersion) and the mass loading is inferred from the available SN energy assuming energy-driven winds, where the energy is supplied by SNII ( $1.09 \times 10^{51}$  erg per SNII)<sup>1</sup>. For the enrichment of the winds we employ a sub-grid metal-loading scheme that regulates the degree of wind enrichment such that 40% of the local ISM metals are driven away by SN driven galactic winds. We previously found that this is required to simultaneously reproduce the stellar mass content of low mass haloes and their gas oxygen abundances (see also Zahid et al. 2014).

- **Supermassive black holes and associated feedback:** Our model includes procedures for supermassive black hole (SMBH) seeding, SMBH accretion and SMBH merging following Springel et al. (2005a). SMBHs are seeded in friends-of-friends (FOF) groups more massive than  $7.1 \times 10^{10} M_{\odot}$  with a SMBH seed mass of  $1.4 \times 10^5 M_{\odot}$ . The feedback of SMBHs distinguishes between quasar- and radio-mode feedback (Sijacki et al. 2007). We also added a novel prescription for radiative feedback from AGNs, that heats surrounding halo gas and modifies its ionisation state and hence the net cooling rate. This model assumes an average spectral energy distribution and a luminosity-dependent scaling of obscuration effects (see Vogelsberger et al. 2013, for details).

The free parameters of our model are set to physically plausible values and have been constrained based on the star formation efficiency using smaller scale simulations (Vogelsberger et al. 2013) and with minor modifications in high-resolution zoom-in simulations of individual Milky Way-like haloes (Marinacci et al. 2014a,b). They were also used in recent magneto-hydrodynamical simulations of Milky Way-like haloes (Pakmor et al. 2014).

### 2.3 Initial conditions and simulation suite

We use the Boltzmann code `CAMB` (Seljak & Zaldarriaga 1996; Lewis & Challinor 2011) to compute the linear power spectrum of a  $\Lambda$ CDM cosmology with the parameters  $\Omega_{\text{m}} = 0.2726$ ,  $\Omega_{\Lambda} = 0.7274$ ,  $\Omega_{\text{b}} = 0.0456$ ,  $\sigma_8 = 0.809$ ,  $n_s = 0.963$ , and  $H_0 = 100 h \text{ km s}^{-1} \text{ Mpc}^{-1}$  with  $h = 0.704$ . These parameters are consistent with the latest Wilkinson Microwave Anisotropy Probe (WMAP)-9 measurements (Hinshaw et al. 2013), but slightly offset from the recent first year results of the Planck mission (Planck Collaboration et al. 2013). We note, however, that a recent re-analysis of the Planck data (using a map-based foreground cleaning procedure, relying on a combination of 353 GHz and 545 GHz frequency maps to reduce residual

<sup>1</sup> The SNII energy for driving stellar winds used in our model was not stated correctly in Vogelsberger et al. (2013) and was corrected in a subsequent erratum (Vogelsberger et al. 2014a)

name	volume [(Mpc) <sup>3</sup> ]	DM particles / hydro cells / MC tracers	$\epsilon_{\text{baryon}}/\epsilon_{\text{DM}}$ [pc]	$m_{\text{baryon}}/m_{\text{DM}}$ [10 <sup>5</sup> M <sub>⊙</sub> ]	$r_{\text{cell}}^{\text{min}}$ [pc]	$m_{\text{cell}}^{\text{min}}$ [10 <sup>5</sup> M <sub>⊙</sub> ]	description
Illustris-1	106.5 <sup>3</sup>	3 × 1,820 <sup>3</sup> ≃ 18.1 × 10 <sup>9</sup>	710/1,420	12.6/62.6	48	0.15	full physics
Illustris-2	106.5 <sup>3</sup>	3 × 910 <sup>3</sup> ≃ 2.3 × 10 <sup>9</sup>	1,420/2,840	100.7/501.0	98	1.3	full physics
Illustris-3	106.5 <sup>3</sup>	3 × 455 <sup>3</sup> ≃ 0.3 × 10 <sup>9</sup>	2,840/5,680	805.2/4008.2	273	15.3	full physics
Illustris-Dark-1	106.5 <sup>3</sup>	1 × 1,820 <sup>3</sup>	710/1,420	−/75.2	—	—	DM only
Illustris-Dark-2	106.5 <sup>3</sup>	1 × 910 <sup>3</sup>	1,420/2,840	−/601.7	—	—	DM only
Illustris-Dark-3	106.5 <sup>3</sup>	1 × 455 <sup>3</sup>	2,840/5,680	−/4813.3	—	—	DM only
Illustris-NR-2	106.5 <sup>3</sup>	2 × 910 <sup>3</sup> ≃ 1.5 × 10 <sup>9</sup>	1,420/2,840	100.7/501.0	893.8	6.6	no cooling/SF/feedback
Illustris-NR-3	106.5 <sup>3</sup>	2 × 455 <sup>3</sup> ≃ 0.2 × 10 <sup>9</sup>	2,840/5,680	805.2/4008.2	2322.8	39.4	no cooling/SF/feedback

**Table 1.** Details of the Illustris simulation suite. Illustris-(1,2,3) are hydrodynamical simulations including our model for galaxy formation physics. Illustris-Dark-(1,2,3) are DM-only versions of the original Illustris simulations. They have the same initial conditions but do not include baryonic matter. Illustris-NR-(2,3) include baryons, but do not account for any feedback or cooling processes (non-radiative). Illustris-1 follows the evolution of 12,057,136,000 DM particles and hydrodynamical cells in total with the smallest fiducial cell size ( $r_{\text{cell}}^{\text{min}}$ ) below 50 pc and the least massive cells having masses of a few times 10<sup>4</sup> M<sub>⊙</sub> ( $m_{\text{cell}}^{\text{min}}$ ). In addition, we follow the evolution of 1,820<sup>3</sup> Monte-Carlo tracer particles (MC tracers).

foregrounds in the intermediate frequency maps used for cosmological inference) found cosmological parameters quite consistent with pre-Planck cosmic microwave background analyses and astronomical observations (Spergel et al. 2013).

We create a random realisation of this cosmology in periodic boxes with a side length of  $75 h^{-1} \text{Mpc} \simeq 106.5 \text{Mpc}$ , starting from an initial “glass-like” particle configuration (White 1996) composed of one thousand 182<sup>3</sup> particle tiles. We employ a 3,640<sup>3</sup> Fast Fourier Transform to calculate the displacement field and use Lagrangian perturbation theory (Zel’dovich approximation (Zel’dovich 1970)) to move particles. We de-convolve the input power spectrum for smoothing effects due to the interpolation off this grid. Initial conditions are generated at  $z = 127$  with gas particles/cells added to the initial conditions by splitting each original particle into a DM and gas cell pair, separating them from one another such that two interleaved grids are formed, keeping the centre-of-mass of each pair fixed. We use the total linear matter power spectrum to displace both particle species. The initial gas temperature at  $z = 127$  is set to 245 K based on a RECFAST (Seager et al. 1999, 2011) calculation. Although Illustris samples a large region, its volume is still subject to cosmic variance (see, Genel et al., in prep, for more details). We have, therefore, generated 100 different random fields and inspected their power spectra and mass functions at  $z = 0$  to make sure that we do not simulate an unusual or extreme density field that is dominated by a few large clusters or voids.

The main simulations of the Illustris project are summarised in Table 1. Illustris-(1,2,3) represent our principal simulations which include hydrodynamics and our galaxy formation model. The different resolution levels (1,2,3) provide a convergence study in which the mass resolution is changed by a factor of 64 in total, and the spatial force resolution by a factor of 4. The level-1 simulation initially consists of 6,028,568,000 hydrodynamic cells and the same number of DM particles. At  $z = 0$ , it contains 5,280,615,062 gas resolution elements, 595,243,070 stellar particles, and 32,552 SMBH particles. The number of DM and tracer particles (see below) is fixed as a function of time (i.e. 1,820<sup>3</sup> each). The gravitational softening length of DM particles is kept fixed in comoving coordinates ( $\epsilon_{\text{DM}}$ ). For baryonic collisionless particles (stars and SMBHs), we limit the softening length to a maximum physical scale ( $\epsilon_{\text{baryon}}$ ). Gas cells use an adaptive soft-

ening length tied to their cell size with a floor given by the softening length of the other collisionless baryonic particles. We employ a (de-) refinement scheme which keeps the cell masses typically within a factor of two of a specified target mass ( $m_{\text{baryon}}$ ), and a regularisation scheme steering the mesh towards a computationally efficient centroidal configuration (as described and used in Springel 2010; Vogelsberger et al. 2012, 2013).

Illustris-1 has a large dynamic range, resolving gravitational dynamics down to about 710 pc (at  $z = 0$ ), while at the same time following the large-scale evolution in the full (106.5 Mpc)<sup>3</sup> volume. At  $z = 0$  the smallest cells in Illustris-1 have a typical extent (fiducial radius) of only 48 pc, which is the smallest scale over which the gas hydrodynamics and baryonic processes are resolved. For the least massive cells we achieve a mass resolution of  $1.5 \times 10^4 M_{\odot}$ . 16 million CPU hours were needed to evolve the simulation from the starting redshift  $z = 127$  to  $z = 0$ , using 8192 cores and an equal number of MPI-ranks on the CURIE supercomputer at CEA/France and the SuperMUC machine at the Leibniz Computing Centre in Germany. An additional 3 million CPU hours were spent on carrying out the on-the-fly galaxy identification with the SUBFIND algorithm (see below). The peak memory use of our production code was slightly more than 25 TB of RAM with a maximum imbalance in the memory use of 5%.

The Illustris-Dark-(1,2,3) simulations use the same initial conditions but do not include the baryonic component. Illustris-NR-(2,3) include baryons, but do not include any feedback, SF, or cooling processes (non-radiative). Through this combined set of simulations we can, for example, study the impact of baryons and feedback processes on the distribution of DM, as we will demonstrate below.

## 2.4 Post-processing

DM haloes were identified on-the-fly for each snapshot using a friends-of-friends (FOF) algorithm (Davis et al. 1985) with a linking length of 0.2 times the mean particle separation and a minimum particle number of 32. Other particle types (stellar particles, gas cells, SMBH particles) were attached to these FOF primaries in a secondary linking stage (Dolag et al. 2009). Subsequently, gravitationally bound substructures are identified in each halo using the SUBFIND algorithm with its extension for the treat-



ment of non-DM particles (Springel et al. 2001; Dolag et al. 2009). Each subhalo has a well defined mass based on the particles which are bound to it. However, haloes are composed of many subhaloes and different mass definitions for haloes are commonly used. The most basic definition assigns the total FOF mass to a halo ( $M_{\text{FOF}}$ ). Another common approach defines the halo mass to be the mass  $M_{\Delta}$ , defined as the mass which is contained in a spherical region with average density  $\Delta$  times the critical density of the universe at that time. There are different choices for  $\Delta$  possible, for example:  $\Delta = 200$ ,  $\Delta = 200 \Omega_m(z)$ , or  $\Delta_v(z)$ , where the last value comes from a spherical top-hat collapse model (Bryan & Norman 1998). In the following we will mainly use  $\Delta = 200$ , and refer to  $M_{200,\text{crit}}$  for the corresponding mass and  $R_{200,\text{crit}}$  for the enclosing radius. Whenever we refer to a virial mass and virial radius we mean  $M_{200,\text{crit}}$  and  $R_{200,\text{crit}}$ , respectively. For more massive haloes (groups and clusters) we will also quote  $M_{500,\text{crit}}$  and  $R_{500,\text{crit}}$ , which are more closely related to observationally derived quantities of clusters.

The structure finding procedure yields 7,713,601 FOF groups with more than 32 particles and 4,366,546 individual (sub)haloes at  $z = 0$  in Illustris-1. The largest FOF group at  $z = 0$ , a cluster-mass halo with a total mass of  $4.6 \times 10^{14} M_{\odot}$ , contains over 66.5 million DM particles, 22.2 million Voronoi cells, and 14.4 million stellar particles. Based on the snapshots and group catalogues, we have constructed different types of merger trees, for example using an extended and updated version of LHalOTree (also used for the Millennium simulations Springel et al. 2005b), and ROCKSTAR (Behroozi et al. 2013b), and the newly developed SubLink code (Rodríguez-Gomez et al., in prep). Each snapshot of Illustris-1 amounts to about 1.5 TB of raw particle data, whereas a snapshot of Illustris-Dark-1 adds up to 0.2 TB. For each simulation we generate 136 snapshots, yielding a cumulative data volume of more than 230 TB. To facilitate efficient access to individual groups, (sub)haloes, and galaxies, the raw particle data are stored in sorted order in output files according to the SUBFIND grouping. With the help of an offset table, this allows for a quick retrieval of any bound structure in the snapshots with minimal I/O requirements. We have furthermore extended SUBFIND to also group non-FOF particle/cell data such that the environment of specific haloes can be easily read from disk. Furthermore, SUBFIND was extended to compute and store many galaxy properties, such as stellar luminosities in various broadband filters (SDSS and Johnson), galaxy masses, galaxy stellar metallicities, gas metallicities, neutral hydrogen content, etc., which greatly simplifies subsequent analysis.

For definiteness, we derive the various galaxy properties from the gravitationally bound mass that is contained within a radius  $r_*$  that equals twice the stellar half mass radius of each SUBFIND (sub)halo. Using this definition, the galactic stellar mass does not differ significantly from the total stellar mass for low mass systems, but some of the intra-cluster light for massive systems is excluded. We have checked this definition against surface brightness cuts in different bands and find it to give similar results as such more elaborate methods for excluding intra-cluster light. Unless mentioned otherwise, we will always measure galactic properties (masses, light, SF rates, etc.) within the  $r_*$  radius.

Besides writing snapshots for the total simulation volume at 136 specific times, we have selected four disjoint small subboxes (denoted as SUB-A, SUB-B, SUB-C, SUB-D) for writing their data at every high-level synchronisation point of the simulations. This yields 3,976 snapshots for each of the four subboxes in Illustris-1; i.e. the time spacing is about 30 times finer than in our standard snapshots. At  $z = 2$  the time spacing between two subbox

outputs is therefore about 3 Myr, and at  $z = 0$  about 8 Myr. The different subboxes cover nearly the same volumes at different places in the simulation volume: SUB-A:  $(10.65 \text{ Mpc})^3$ , SUB-B:  $(11.36 \text{ Mpc})^3$ , SUB-C:  $(7.10 \text{ Mpc})^3$ , SUB-D:  $(7.10 \text{ Mpc})^3$ . At  $z = 0$ , these subboxes contain in SUB-A 33,638,720, in SUB-B 4,361,433, in SUB-C 1,872,848, and in SUB-D 1,651,277 DM particles. The large variation in the number of resolution elements in these subboxes is mainly due to the very different regions they sample, although the box sizes are also slightly different. The present day matter density  $\Omega_m^{\text{sub}}$  in the volumes is 1.47, 0.16, 0.29 and 0.25, for SUB-A to SUB-D, respectively. The stellar content  $\Omega_*^{\text{sub}}$  is also different, amounting to 0.0244, 0.0013, 0.0025, and 0.0027 for SUB-A to SUB-D. These numbers demonstrate that SUB-A samples an overdense region, whereas the other regions are underdense with the most extreme case given by SUB-B. The fine time spacing of these subboxes can be used for detailed studies of dynamical processes in different environments.

All hydrodynamical Illustris simulations include Monte Carlo tracer particles to follow the gas flow accurately (Nelson et al. 2013; Genel et al. 2013; Vogelsberger et al. 2013). For each tracer, we record 13 different hydrodynamical quantities (e.g., maximum past temperature and maximum past density), and we follow the evolution of  $1,820^3 \sim 6$  billion Monte Carlo tracer particles in total. These tracers faithfully follow all conversion and exchange processes in the baryonic component of the simulation (e.g. gas turning into stars, stars returning mass to the gas phase, ejection into the stellar wind state, accretion into SMBHs, etc). The inclusion of tracer particles increases the total particle number of Illustris-1 to more than 18 billion. We note that we use explicitly only MC tracer particles instead of traditional velocity field tracer particles typically employed in AMR codes to avoid biases in the mass fluxes (see Genel et al. 2013, for details).

We need to transform stellar information of our simulations into photometric properties, i.e. stellar light in different filters, to compare the simulated galaxy population with observations. Stellar population synthesis models (e.g., Bruzual & Charlot 2003) provide a straightforward way to associate the stars in our simulations with observable spectra or broad band luminosities. Producing stellar images of galaxies requires assigning colour values to specific bands. Specifically, we make an RGB mapping of the (g,r,i) bands using a commonly employed asinh scaling of Lupton et al. (2004).

### 3 LARGE-SCALE STRUCTURE

The volume of Illustris is sufficiently large to measure large-scale statistics. We demonstrate this below for a few selected quantities, and especially highlight the importance of taking baryonic effects into account since they affect structure formation in a way that cannot be captured by DM-only simulations or semi-analytic models applied to them in post-processing. Before presenting these statistics we will first give some visual overview of the simulation and one of the subboxes, demonstrating their power in disentangling physical processes on short time-scales.

#### 3.1 Visual impression

Figure 1 gives a pictorial overview of our simulation volume at the present day, redshift  $z = 0$ . Dark matter forms the backbone of the cosmic structure, as displayed in the top portion of the figure. This invisible form of matter, potentially made up of neutralinos or axions, is arranged in an intricate cosmic web (e.g. Bond et al.



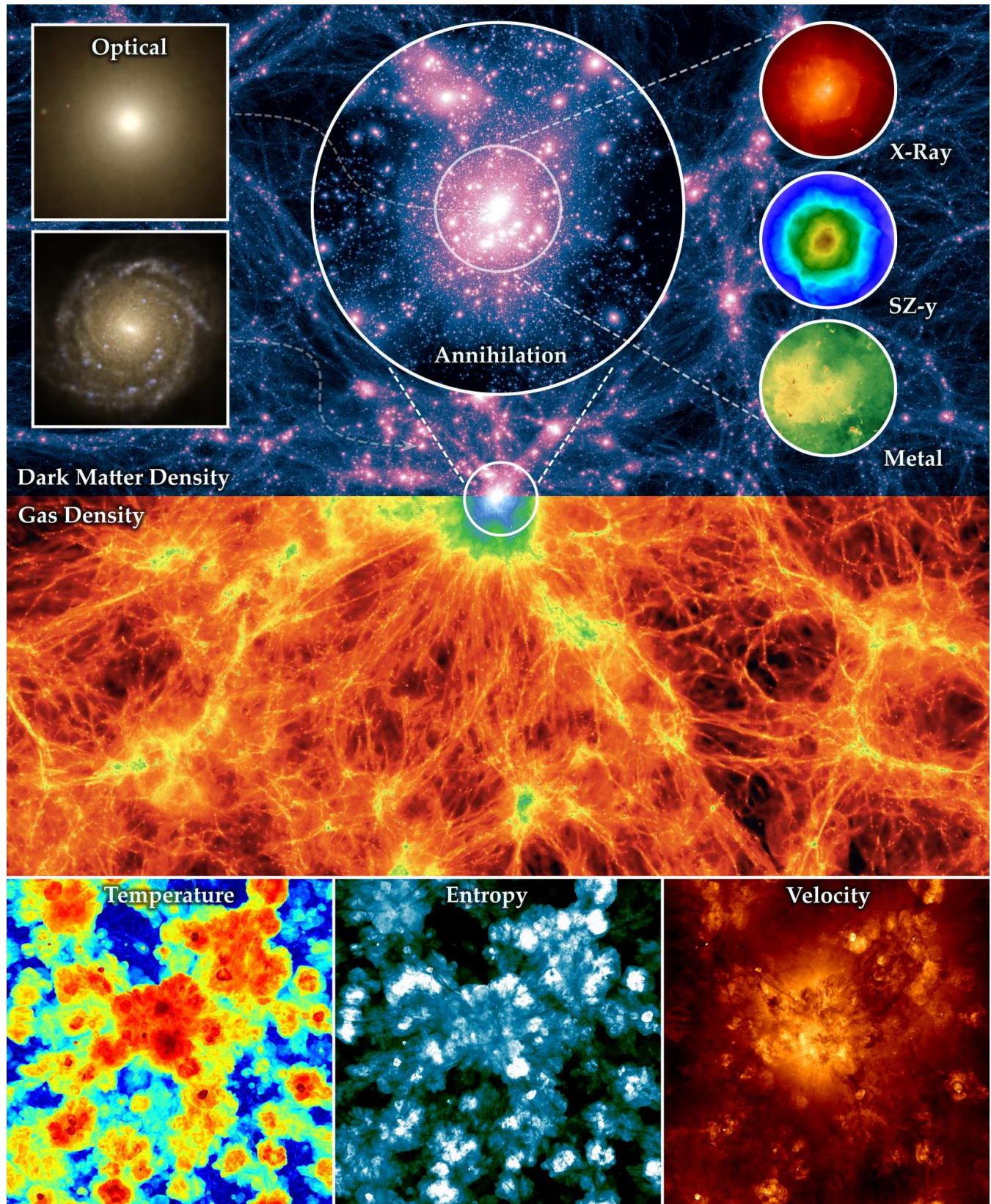


**Figure 1.** Simulated present-day dark and baryonic matter structures. Top panel: Dark matter mass distribution in a slice (21.3 Mpc thickness, 106.5 Mpc width) centered on the most massive halo. Lower panels: gas distribution shown in density, temperature, entropy, and velocity. On the right in the top panel we show (from top to bottom): X-ray emission of hot intra-cluster gas; thermal Sunyaev-Zel'dovich signal; and the distribution of metals in the gas (all within one virial radius). The central circle shows the expected annihilation signal from self-annihilating DM particles within three virial radii. On the left in the top panel we present optical images (g,r,i SDSS broadband filter composites) of the central galaxy of the cluster (top) and a random disk field galaxy (bottom).



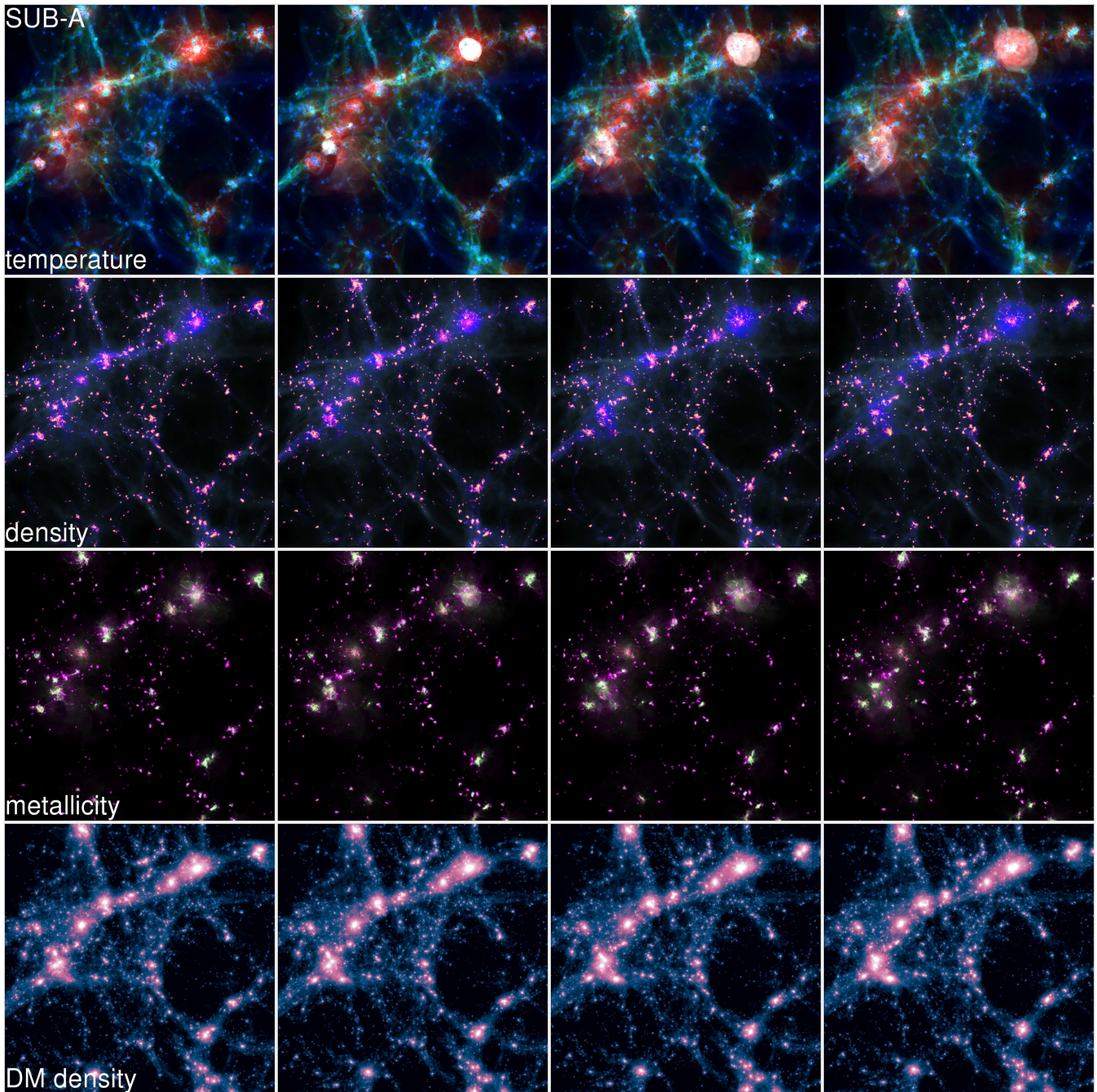


**Figure 2.** Short-time evolution of subbox SUB-A (top to bottom: gas temperature, gas density gas metallicity, DM density). The time evolution starts at  $z = 1.47$  (left) and ends at  $z = 1.36$  (right). We output the subbox data 100 times over this time span yielding a time resolution of less than 3 Myr. The more massive halo in the upper right shows strong AGN activity leading to heating and expansion of large amounts of gas.

1996), with tenuous filaments surrounding large voids and connecting gravitationally bound haloes in which galaxies form through gas condensation and star formation (White & Rees 1978). On large scales, the gas density follows the evolution of the DM (middle panel), which dictates the gravitational field with its five times higher mass density. Hydrodynamical simulations provide important additional information about the gas besides the density, e.g., its temperature, entropy and velocity fields, as illustrated (from left to right) in the bottom panels of the figure.

The DM and gas slice shown in Figure 1 is centered on a galaxy cluster with a virial radius ( $R_{200,\text{crit}}$ ) of 1.26 Mpc and a

virial mass ( $M_{200,\text{crit}}$ ) of  $2.32 \times 10^{14} M_{\odot}$ . This particular cluster, shown enlarged in different figure insets with some of its predicted observational signals, contains 5, 116 resolved subhaloes within its virial radius (16, 937 within its larger FOF group), consistent with the expected population of such subhaloes in a CDM model (Moore et al. 1999; Springel et al. 2008). The large inset on top shows the cluster's expected  $\gamma$ -ray annihilation signal within three virial radii if the elusive DM consists of a Majorana particle that can self-annihilate.

The three insets in the top right of Figure 1 show maps of various observational diagnostics of the central cluster. They include

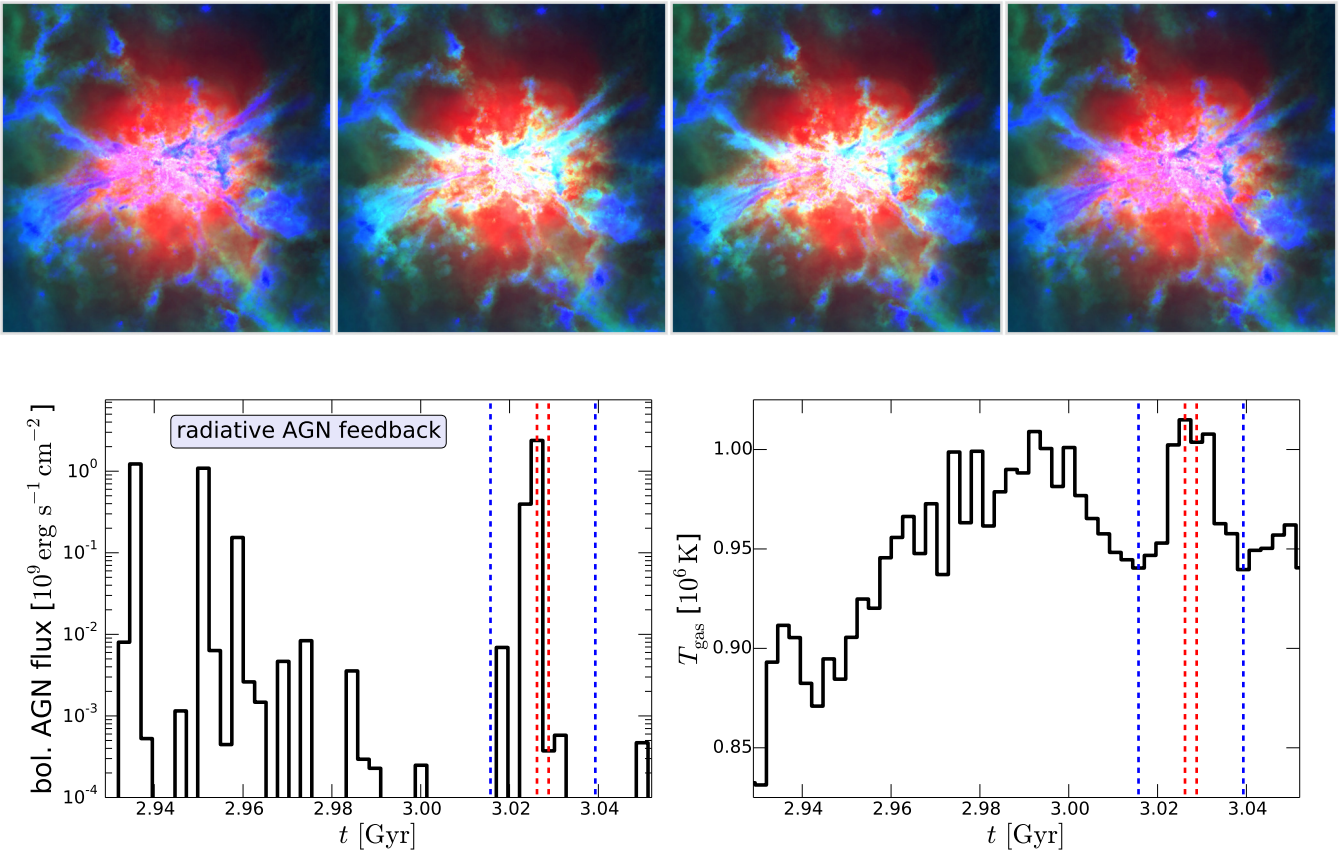


**Figure 3.** Impact of radiative AGN feedback on halo gas. Top panels: Gas temperature projections of a halo within SUB-A. The time separation of the three temperature projections is (in Myr): 10.46, 2.62, 10.51 capturing a brief episode of quasar activity, where AGN radiation alters the cooling rates and heats up the gas. Bottom left panel: Bolometric AGN flux within this halo. Right panel: Temperature evolution of gas belonging to the halo. The four dashed vertical lines correspond to the times of the temperature projections shown in the top. The blue dashed lines capture the system at times of low radiative AGN activity, whereas the red dashed lines show moments of high activity (especially the first dashed red line). AGN radiation heats up the gas for a short amount of time during maximum quasar activity. However, the heating phase is rather short such that this energy injection does not influence the gas significantly on longer time scales due to efficient cooling.

the X-ray emission from hot gas in the cluster within one virial radius (top right inset), where the main contribution comes from bremsstrahlung ( $\propto \sqrt{T}$ ) emission from the hot ( $T > 10^6$  K) intra-cluster gas. We also show the expected thermal Sunyaev-Zel’dovich signal (Sunyaev & Zeldovich 1980), which is due to inverse Compton scattering of background photons of the cosmic microwave background by hot electrons in the cluster plasma. The thermal Sunyaev-Zel’dovich signal of clusters is an important cosmological probe that is being measured, for example, by the Planck satellite (Planck Collaboration et al. 2013), the South Pole Telescope (SPT) (Ruhl et al. 2004), and the Atacama Cosmology Telescope (ACT) (Kosowsky 2003). Thirdly, we show the expected distribution of metals in cluster gas in the lower right inset. These predictions are possible because our simulation traces the evolution of nine different chemical elements as they are synthesised in stars and dispersed by galactic winds. Ionisation states of these elements can be calculated in post-processing and can be compared in detail to quasar spectra probing the circum-galactic medium (Suresh et al, in prep).

Finally, in the upper left panel we show an optical image (in *g*, *r*, *i* SDSS broadband filters) of the central galaxy that formed in the cluster; a massive red elliptical galaxy. For comparison, we also show a typical disk galaxy (lower on the left) that we preferentially

find in the field, away from clusters. These two galaxies differ not only in their morphologies and colours, but also in their present-day star formation rates. The red elliptical galaxy has essentially no ongoing star formation whereas the blue disk still forms stars.

The subboxes can be used to study the time evolution of different large-scale environments in great detail. We demonstrate this in Figure 2, where we show for SUB-A the time evolution of the full temperature projection starting at  $z = 1.47$  ending at  $z = 1.36$  (top row). We output the subbox data 100 times over this time span, yielding a time resolution of less than 3 Myr. One halo in the upper right shows strong radio-mode AGN activity leading to significant heating and expansion of gas around the central SMBH; an effect that can be studied in detail due to the fine time-spacing. The other rows in Figure 2 show density, metallicity, and DM density projections. Some of these quantities, for example the metallicity distribution, is also affected by the outflows generated by SMBH feedback.

The high time resolution of the subbox outputs also makes it possible to understand the impact of physical effects, which occur on even shorter time scales. One such effect is the impact of radiative electro-magnetic AGN feedback on nearby halo gas, which is included in our model using various approximations (see Vogelsberger et al. 2013, for more details). The top panels of Figure 3



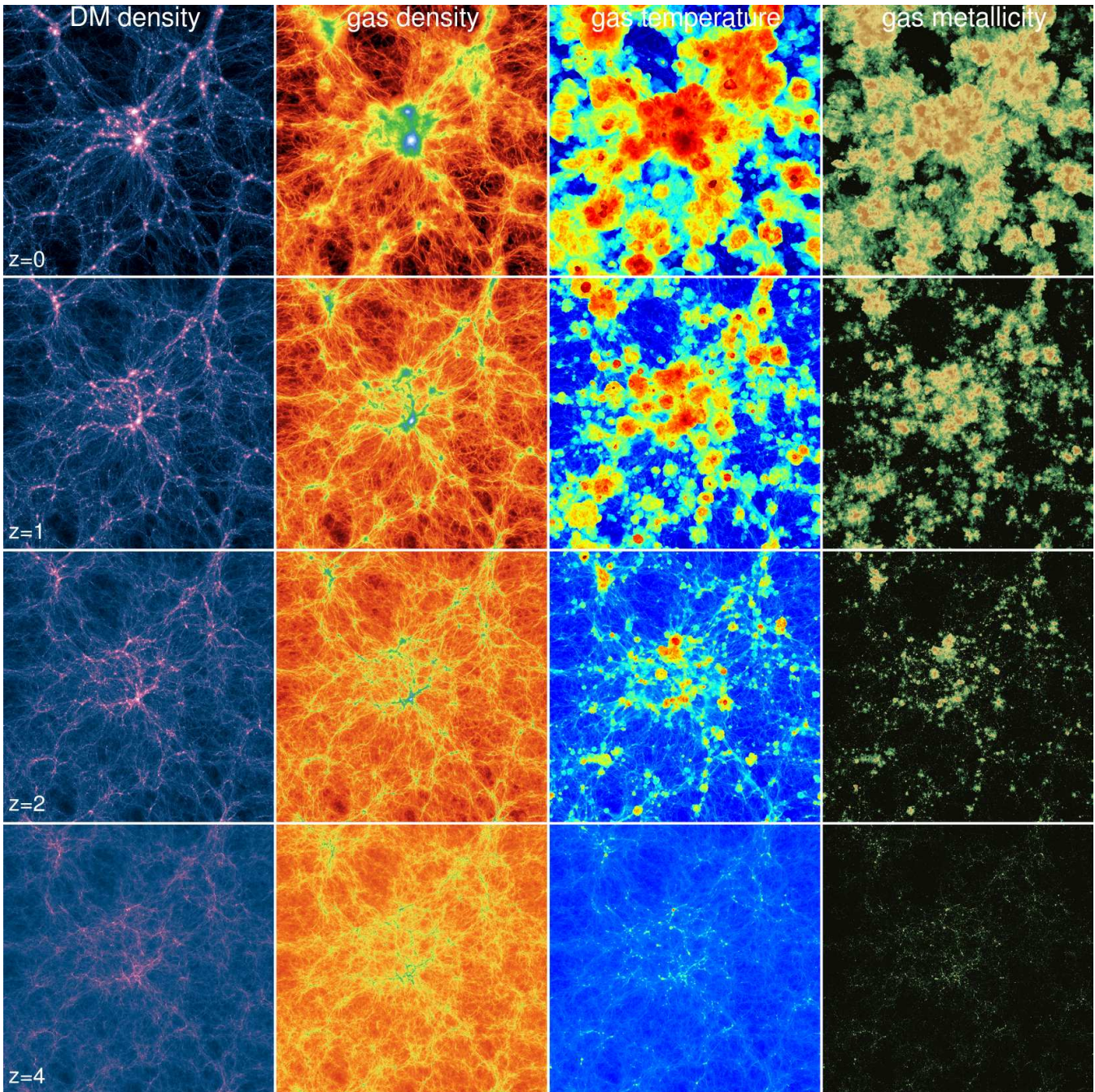


**Figure 4.** Redshift evolution of the DM density, gas density, gas temperature, and gas metallicity for  $z = 0, 1, 2,$  and  $4$  in a projected slice with a thickness of  $21.3$  Mpc (comoving). The slice is centered on the most massive cluster at  $z = 0$  and covers the entire simulation volume ( $106.5$  Mpc width). This is the same slice that was presented in Figure 1. All distributions are fairly uniform at early times. Gravity drives the collapse of haloes as a function of time. Gas heats up when it falls into these haloes, and it then cools down and eventually forms stars. Stellar SN feedback leads to the enrichment of the IGM, as can be seen in the evolving metal distribution.

show the projected gas temperature of a halo within SUB-A. The time separation of the four temperature projections is (from left to right in Myr):  $10.46, 2.62, 10.51$ . This is sufficiently short to capture a brief episode of strong quasar activity, where AGN radiation alters the cooling rates of nearby gas and heats up this gas on a very short time scale. The bottom left panel of Figure 3 shows the bolometric flux within this halo, and the right panel shows the temperature evolution of gas belonging to the halo. The four dashed vertical lines correspond to the times of the temperature projections above.

The blue dashed lines capture the system at times of low radiative AGN activity, whereas the red dashed lines show moments of high activity (especially the first dashed red line). The temperature panel demonstrates that this also increases the gas temperature within the halo. However, this effect is still rather weak compared to thermal and mechanical AGN feedback and furthermore it is only relevant on a very short time scale of about  $10$  Myr due to efficient gas cooling. This form of feedback is therefore not able to inject significant amounts of energy into the gas on longer time scales, and



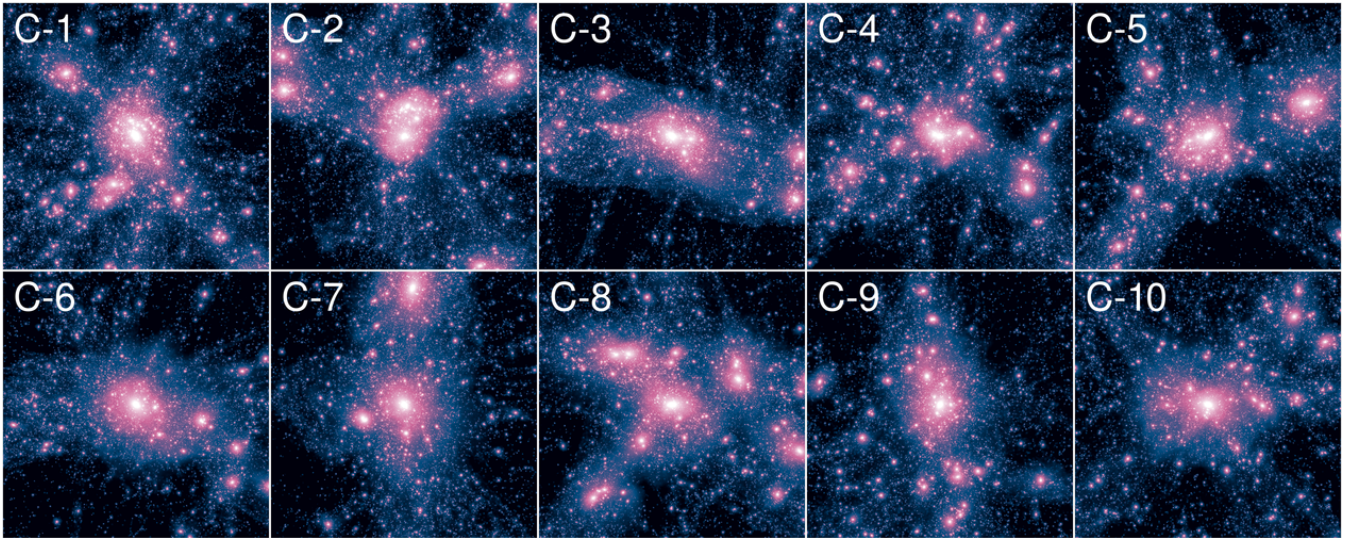


**Figure 5.** Annihilation maps ( $\propto \int dl \rho^2$ , where  $l$  is the distance along the line-of-sight) of the ten most massive haloes (C-1 to C-10, ordered by mass) at  $z = 0$ . The most massive cluster C-1 has a mass of  $2.32 \times 10^{14} M_{\odot}$  and the least massive (lower right) has a mass of  $1.04 \times 10^{14} M_{\odot}$ . They have virial radii of the order of  $\sim 1$  Mpc. Basic parameters of these haloes are summarised in Table 2. In Illustris-1 the clusters are resolved with up to  $\sim 30$  million DM particles within the virial radius, which is sufficient to resolve up to  $\sim 7,000$  subhaloes within this region. Each cluster projection shows a cube with side length of ten times the cluster’s virial radius.

cluster	$M_{200,\text{crit}}$ [ $10^{14} M_{\odot}$ ]	$M_{500,\text{crit}}$ [ $10^{14} M_{\odot}$ ]	$R_{200,\text{crit}}$ [Mpc]	$R_{500,\text{crit}}$ [Mpc]	$N_{\text{sub}}$	$N_{\text{DM}}^{\text{FOF}}$ [ $10^6$ ]	$N_{\text{stars}}^{\text{FOF}}$ [ $10^6$ ]	$N_{\text{cells}}^{\text{FOF}}$ [ $10^6$ ]	$N_{\text{DM}}^{200}$ [ $10^6$ ]	$N_{\text{stars}}^{200}$ [ $10^6$ ]	$N_{\text{cells}}^{200}$ [ $10^6$ ]
C-1	2.32	1.54	1.26	0.81	5,116	66.53	14.40	22.20	32.94	8.33	12.68
C-2	2.23	0.87	1.25	0.67	6,792	56.13	10.69	14.74	32.83	5.94	8.12
C-3	2.18	1.24	1.24	0.75	5,285	44.44	9.08	11.22	32.25	7.21	6.40
C-4	1.69	0.94	1.14	0.69	4,906	32.58	5.90	7.48	24.96	4.74	5.55
C-5	1.36	0.85	1.06	0.67	3,716	29.29	6.13	7.66	19.90	4.84	4.64
C-6	1.28	0.80	1.04	0.65	2,753	30.29	6.77	7.36	18.80	4.73	4.38
C-7	1.17	0.77	1.01	0.64	2,150	27.82	6.39	7.65	17.17	4.19	4.66
C-8	1.17	0.80	1.01	0.65	2,722	42.53	8.54	11.01	17.08	3.25	5.17
C-9	1.12	0.71	0.99	0.63	2,841	27.29	5.47	5.78	16.67	3.22	2.98
C-10	1.04	0.76	0.97	0.64	2,369	24.24	4.95	5.50	15.34	3.48	2.74

**Table 2.** Basic characteristics of the ten most massive clusters presented in the ten right panels of Figure 4. The different columns list: mass (200 critical), mass (500 critical), radius (200 critical), radius (500 critical), number of resolved subhaloes within  $R_{200,\text{crit}}$ , number of DM particles in FOF group, number of stellar particles in FOF group, number of hydrodynamical cells in FOF group, number of DM particles within virial radius, number of stellar particles within virial radius, and number of hydrodynamical cells within virial radius.

it is particularly not able to quench SF in massive clusters (see also Vogelsberger et al. 2013). This is in disagreement with previous statements that this form of feedback has a significant impact on the thermodynamic state of halo gas (e.g., Gnedin & Hollon 2012).

The full simulation volume of Illustris is stored at the 136 major output times. This is sufficient for studying the large-scale evolution and allows also for the computation of detailed merger trees (Illustris stored twice as many snapshots as the Millennium-I and Millennium-II simulations). An overview of the time evolution of the large-scale structure of the Illustris-1 simulation is presented in Figure 4 where we show snapshots of the DM density, gas density, gas temperature, and gas metallicity for redshifts  $z = 0, 1, 2,$  and  $4$ . The displayed slice is centered on the same most massive halo in the simulation volume and has a thickness of  $21.3$  Mpc (comoving). The gradual build-up of cosmic structure is evident in all panels. The matter distribution at  $z = 4$  is still comparatively smooth and uniform, and the gas temperature is mostly cold around  $10^4$  K.

Metals are not spread around much yet; instead they are mainly concentrated at the centers of forming haloes, where they were created as a product of SF and subsequent stellar evolution processes. The gas is significantly heated over time by virial shocks and feedback, and a population of haloes forms through the hierarchical growth process as predicted by the  $\Lambda$ CDM cosmological model. SN and AGN feedback enrich the circum-galactic medium (CGM) and the intergalactic medium (IGM) by dispersing metals even into regions outside of haloes. This can clearly be seen in the metallicity map, where the metal distribution at  $z = 0$  appears more diffuse compared to earlier times, indicating that metals have become much less concentrated towards halo centers. Gas heating at  $z \gtrsim 2$  is largely driven by virial shocks and partially also by SN heating. At later times around  $z = 1$  and  $z = 0$ , radio-mode AGN feedback leads to significant gas heating especially in more massive haloes, where SMBH feedback is relevant to regulating SF. We note that this feedback is only relevant for low SMBH accretion rates, and it

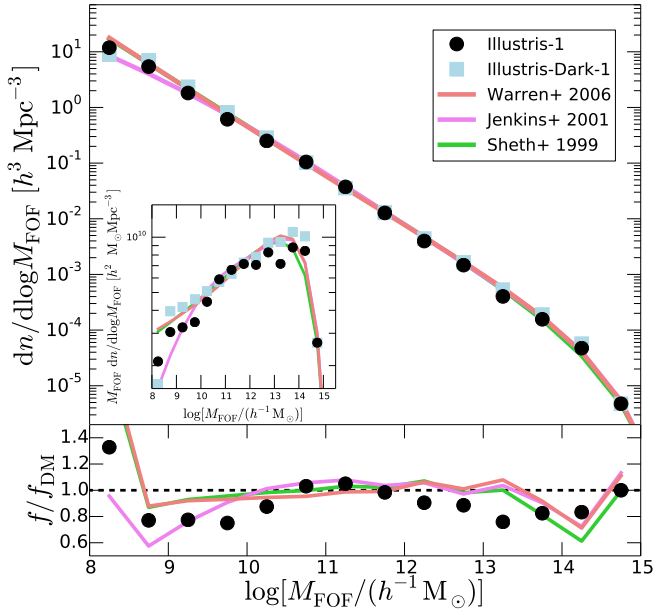


**Figure 6.** Differential halo mass function of Illustris-1 and Illustris-Dark-1, where we define the halo mass as the total FOF mass, compared to some recent empirical fitting formulae (Sheth & Tormen 1999; Jenkins et al. 2001; Warren et al. 2006). The inset shows the halo mass function multiplied with  $M_{\text{FOF}}$  to reduce the dynamic range and show differences more clearly. The lower panel shows the relative differences between the various curves in the upper panel. The halo mass function of the full physics simulation deviates at low and high halo masses from the Illustris-Dark-1 prediction. Both differences are due to efficient feedback affecting the structure of low mass and high mass haloes.

is crucial in regulating SF in massive clusters. Quasar-mode feedback is not efficient in quenching these systems (see Sijacki et al. 2007; Vogelsberger et al. 2013, for details).

At the present epoch, Illustris-1 contains 3, 237, 813, 076 DM particles in FOF groups (53.7%) and 2, 790, 754, 924 DM particles (46.3%) which do not belong to any FOF group. The most massive haloes in our simulation reach cluster scale masses and are particularly well-resolved. We demonstrate this in Figure 5, where we show annihilation radiation maps of the ten most massive haloes. C-1 is the most massive halo, which is at the center of Figure 1. Table 2 contains some basic simulation characteristics of these clusters. All of them have virial masses ( $M_{200,\text{crit}}$ ) above  $10^{14} M_{\odot}$  and virial radii ( $R_{200,\text{crit}}$ ) close to or above  $\sim 1$  Mpc. The most well-resolved cluster (C-1) contains nearly 33 million DM particles within the virial radius, and more than 12.6 million gas resolution elements. SF led to the creation of more than 8.3 million stellar particles by  $z = 0$ .

### 3.2 Large-scale structure statistics

The total matter power spectrum of Illustris-1 and Illustris-Dark-1 was presented and discussed in Vogelsberger et al. (2014b). There we have demonstrated that baryons can lead to significant changes in the matter distribution even on larger scales due to energetic AGN feedback, which affects, for example, future weak lensing based precision measurements of cosmological parameters.

Another important way to infer cosmological parameters lies in measurements of the halo mass function, which are ulti-

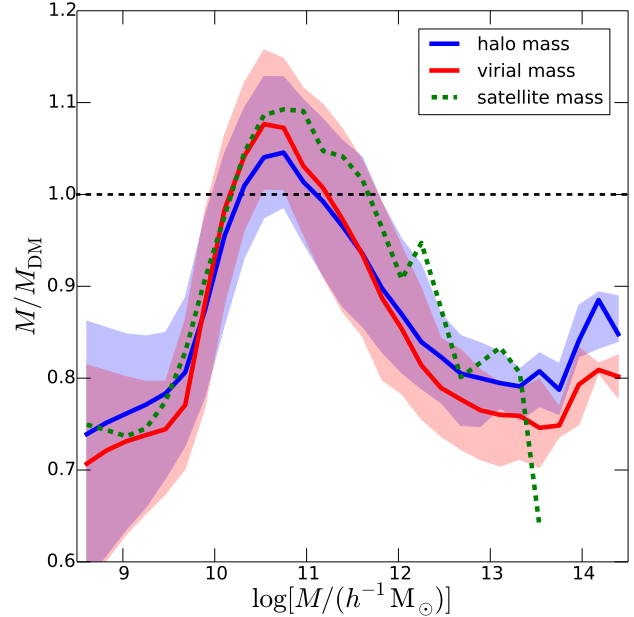


**Figure 7.** Feedback induced changes in gravitationally bound and virial halo masses between Illustris-1 and Illustris-Dark-1 for matched haloes between the two simulations. Unlike most previous studies we find that feedback reduces the halo masses not only for low mass systems, but also in massive haloes, which is caused by our AGN feedback implementation. In both cases the mass deviates by up to  $\sim 30\%$  compared to the DM-only result of the matched Illustris-Dark-1 haloes. The blue line shows this relation for all haloes (main and subhaloes), whereas the red lines focuses on the virial masses of main haloes (centrals). The green line shows the result for satellites. Blue and red contours show the  $1\sigma$  spread.

mately based on a “counting procedure” of some kind, for example using surveys of galaxy clusters in X-ray emission (e.g., the upcoming eROSITA mission (Predehl et al. 2006), or thermal Sunyaev-Zel’dovich observations (e.g., by the South Pole Telescope (SPT) (Ruhl et al. 2004), and the Atacama Cosmology Telescope (ACT) (Kosowsky 2003)). However, taking advantage of current and upcoming surveys to improve cosmological parameter constraints requires theoretical mass function predictions that are accurate to high precision (Wu et al. 2010). Recent theoretical predictions of the halo mass function based on dissipationless N-body simulations have reduced the statistical uncertainties to a very small level (Tinker et al. 2008), but they have not yet addressed the systematic uncertainty associated with the effect of baryons on DM haloes, which depends sensitively on the feedback models (Rudd et al. 2008; Stanek et al. 2009; Cui et al. 2012).

In Figure 6 we present the differential halo mass functions of Illustris-1 and Illustris-Dark-1 along with empirical fitting formulae (Sheth & Tormen 1999; Jenkins et al. 2001; Warren et al. 2006). Here we define halo mass as FOF mass. The main panel of Figure 6 shows the unscaled differential halo mass function. Although the dynamic range of this figure is large, some differences between Illustris-1 and Illustris-1-Dark are already visible. Multiplying the halo mass function by mass reduces the displayed dynamic range significantly and makes the differences clearer (see inset). The bottom panel shows the relative differences between the simulations. This reveals some interesting features in the halo mass function. Baryons affect the mass function strongly at low and high halo masses, leading to a reduction of the overall abundance at both

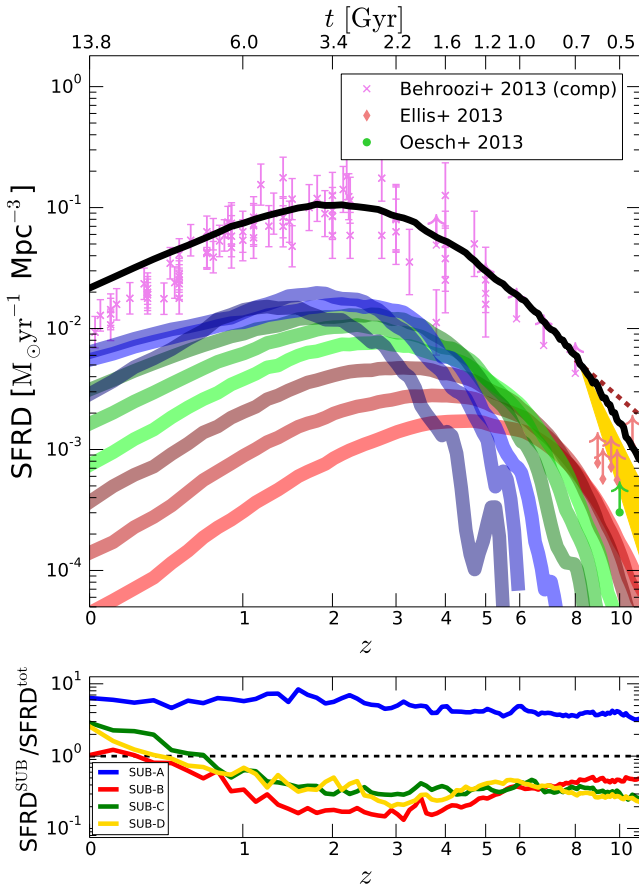


**Figure 8.** Top panel: Cosmic star formation rate density (SFRD) compared to observations (Behroozi et al. 2013a; Ellis et al. 2013; Oesch et al. 2013) (arrows show lower observational limits). The black solid line shows the total SFRD; coloured thick lines show the contributions from galaxies of different stellar masses ( $10^7 M_\odot$  to  $10^{11} M_\odot$ ) ranging from low mass (red lines:  $M_\star = 10^{7.7,5,8} M_\odot$ ) to intermediate mass (green lines:  $M_\star = 10^{8.5,9,9.5} M_\odot$ ) to the most massive systems (blue lines:  $M_\star = 10^{10,10.5,11} M_\odot$ ). The thick coloured lines have colours from bright to dark to distinguish the different masses (low to high) within the range. In general, star formation at early times is dominated by low mass systems (red lines), whereas late time star formation is mainly caused by massive systems (blue lines), although the highest mass systems are quenched by AGN feedback. The dashed line at high  $z$  shows the extrapolated observational high redshift trend ( $\propto (1+z)^{-3.6}$ ) and the yellow contour brackets the best-fit slopes for combined  $z \geq 8$  measurements ( $\propto (1+z)^{-10.9 \pm 2.5}$ ) in this redshift regime (Oesch et al. 2013). For these high redshifts beyond  $z \sim 8$  our model agrees best with the shallowest slope ( $-10.9 + 2.5$ ) of Oesch et al. (2013). Bottom panel: Ratio of SFRD in individual subboxes (SUB-A to SUB-D) and total SFRD. SUB-A has a high overdensity, and therefore produces more stars compared to the total volume. SUB-B, SUB-C, and SUB-D are less dense and produce fewer stars until  $z \sim 1$ .

ends. This is the regime where baryonic feedback processes are strongest: reionisation, SN feedback, and AGN feedback. The effects are different if no strong feedback processes are included. For example, neglecting AGN feedback leads to an increase of the halo mass function at the massive end (e.g., Cui et al. 2012).

Related effects can be identified when comparing the masses of matched individual haloes as presented in Figure 7. Here we find that haloes with masses around  $10^{11} M_\odot$  are typically more massive than their DM-only counterparts. This is close to the halo

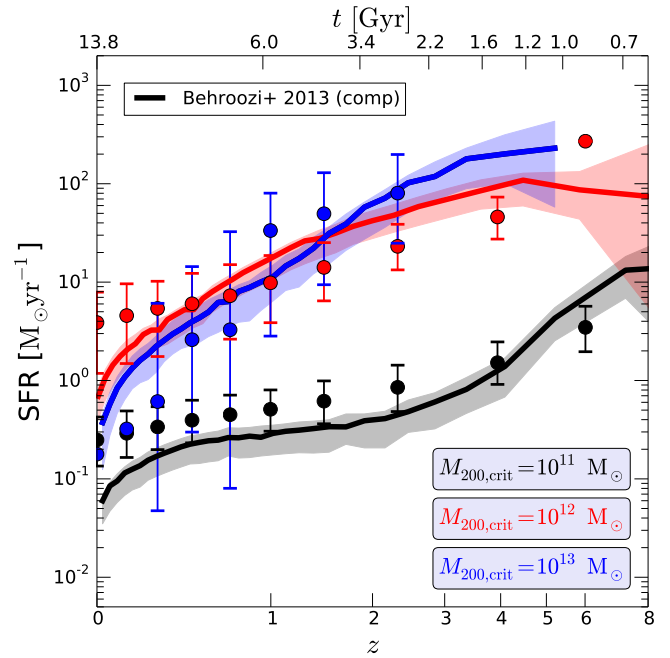


**Figure 9.** Average star formation rates for galaxies in haloes at a given instantaneous halo mass and redshift. Symbols with error bars show the simulation results, whereas observationally inferred results are shown by lines with uncertainty bands. We recover the observed redshift trends. However, at  $z \lesssim 0.5$  less massive haloes below  $M_{200,\text{crit}} \sim 10^{12} M_\odot$  tend to overproduce stars. Nevertheless our results are still consistent within the uncertainties. Interestingly, our model tends to slightly underproduce stars in the most massive haloes shown for a short period of time towards lower redshifts, but the SFR at  $z = 0$  is consistent with observations for the most massive haloes shown.

mass scale where SF is most efficient (see below). However, below and above this mass scale we find that feedback processes lead to a significant redistribution of matter such that lower and higher mass haloes tend to be less massive in Illustris-1 compared to the matched haloes from Illustris-Dark-1. This decrease in mass can reach  $\sim 30\%$  for the lowest and highest halo masses probed by our simulation. We note that the findings in Figure 7 are different from many previous predictions (e.g., Sawala et al. 2013; Velliscig et al. 2014) since we find mass suppression also for massive haloes, which is caused by our strong AGN feedback. This also leads to a significant baryon fraction suppression in these systems (Genel et al., in prep). We caution that this effect likely depends on the detailed implementation of AGN feedback, specifically, the form of radio-mode AGN feedback, and may not be present for implementations that do not lead to a significant suppression of the baryon fraction (see also Genel et al., in prep). A detailed study of the impact of baryonic processes on the halo masses will be presented in Rodriguez-Gomez et al. (in prep).

#### 4 THE GALAXY POPULATION

A primary goal of galaxy formation models lies in explaining the stellar content of the Universe. We will in the following demonstrate that our simulation yields a realistic galaxy and stellar population which is in reasonable agreement with various recent observations.



#### 4.1 The formation of galaxy stellar masses

We start by looking at the global history of star formation over cosmic time. Figure 8 shows the evolution of the cosmic SF rate density (SFRD), a key prediction that can be tested against a plethora of measurements at different epochs, extending back to just a few hundred million years after the Big Bang. The compiled data points in Figure 8 are based on different types of surveys, including inferences from narrowband (e.g.,  $H\alpha$ ), broadband (UV-IR), and radio (1.4 GHz) observations. We also include recent estimates for the very early SFRD beyond  $z = 8$ . These are based on the Cluster Lensing And Supernova survey with Hubble (CLASH) (Postman et al. 2012), near-infrared Wide-Field Camera 3 (WFC3/IR) (Kimble et al. 2008) images of the Hubble Ultra Deep Field (UDF), and CANDELS WFC3/IR Great Observatories Origins Deep Survey (GOODS) (Giavalisco et al. 2004)-N imaging data. Reliable SFRD estimates at these high redshifts are extremely difficult to obtain, and it is still under debate how this quantity evolves towards higher  $z$ . Our predicted SF history is in good agreement with the observations, including the recent lower limits (Ellis et al. 2013; Oesch et al. 2013) beyond  $z \sim 8$ . The dashed line shows the extrapolated observational lower redshift trend ( $\propto (1+z)^{-3.6}$ ) and the yellow contour brackets the best-fit slopes for combined  $z \geq 8$  measurements ( $\propto (1+z)^{-10.9 \pm 2.5}$ ) (Oesch et al. 2013). Interestingly, our model prediction agrees best with the shallowest slope ( $-10.9 + 2.5$ ). Towards lower redshifts we find some tension between the observational data and our predictions, where our model tends to produce too many stars. It seems that our AGN feedback is not efficient enough to quench SF sufficiently at these times. Specifically, radio-mode AGN feedback still seems to be too weak to regulate SF sufficiently in massive haloes. This is despite the fact that our radio-mode feedback parameters are chosen to result in more energetic AGN feedback compared to previous studies (see Vogelsberger et al. 2013, for details).

Splitting the SFRD into contributions from galaxies in different stellar mass bins (various coloured bold lines) reveals that the early SF is dominated by low mass systems, whereas at late times more massive systems are most important (see also, Genel et al., in prep, for a break down in halo mass). However, in the most massive objects AGN feedback from central SMBHs has quenched star formation activity, and so they do not contribute significantly to present-day star formation. The largest contribution to the present-day SFRD comes from galaxies which have stellar masses of about  $M_* \sim 10^{10-10.5} M_\odot$ . We note that this is close to the regime where SF is most efficient (see below) and it is the transition region below which SN feedback is responsible for regulating SF. Above that mass scale radio-mode AGN feedback is the main driver of SF quenching our our simulation.

The bottom panel of Figure 8 shows the ratios of the SFRD in the individual subboxes (SUB-A to SUB-D) and the total SFRD. SUB-A has a high overdensity, and therefore produces more stars compared to the total volume. SUB-B, SUB-C, and SUB-D are less dense and produce fewer stars until  $z \sim 0.7$ . After that SF is also more efficient in these subboxes compared to the total SFRD. The subboxes therefore show a significant variation in SFRD compared to the global SFRD, sampling significantly different regions of the simulation volume.

In addition to inspecting the global SFRD of the total simulation volume, we can also compare star formation rates within haloes of a given mass and compare to observationally derived results. This is shown in Figure 9, where we compare star formation rates for three different instantaneous halo masses  $M_{200,\text{crit}} =$

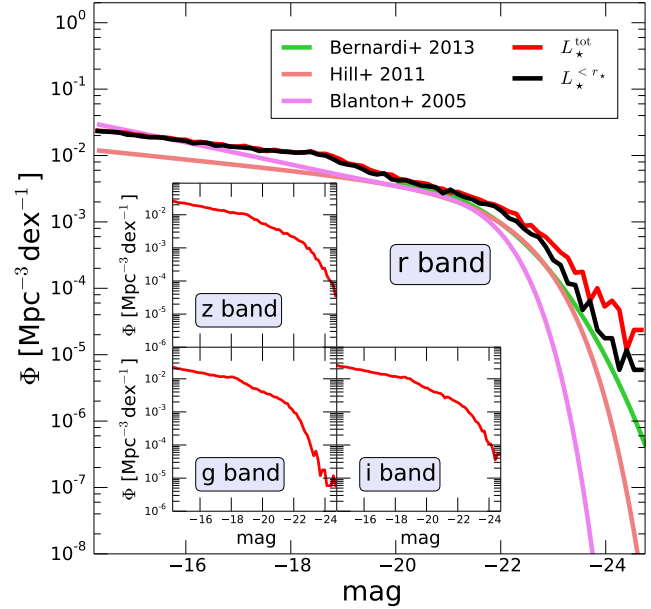


**Figure 10.** Low redshift SDSS galaxy luminosity functions (GLFs) in g,r,i,z bands. The main panel compares the predicted r band GLF to recent observations (Blanton et al. 2005b; Hill et al. 2011; Bernardi et al. 2013), which probe the light distribution out to different radii. We present the predicted total light emission excluding satellites ( $L_*^{\text{tot}}$ ) and the emission from the central galaxy ( $L_*^{<r_*}$ ) to take into account observational uncertainties in the light assignment for massive galaxies (see Bernardi et al. 2013, for details). We note that simulation luminosities shown here do not include dust effects.

$10^{11-11.2}$ ,  $10^{12-12.2}$ ,  $10^{13-13.2} M_\odot$ . The symbols with error bars show the simulation results, whereas observational estimates are shown by lines with uncertainty bands. We recover the general trends of the observations although not all data points agree. At late times our model tends to produce slightly too many stars compared to observations, especially in the  $M_{200,\text{crit}} \sim 10^{12} M_\odot$  halo mass range. We saw this already in Figure 8, where the late time SFRD was slightly too high for the corresponding stellar mass range. As shown in Genel et al. (in prep) this halo mass range is also exactly the one that contributes the most to the overestimated global SFRD.

The galaxy population can be quantified through the galaxy luminosity function (GLF). In Figure 10 we examine the present-day GLF for four broadband SDSS filters (g,r,i,z) and compare to observations (Blanton et al. 2005b; Hill et al. 2011; Bernardi et al. 2013) for the r-band based on SDSS data. Different observations probe the stellar distribution out to various radii depending on the assumed light profile. Particularly for the bright end of the luminosity function this adds measurement uncertainties, because the assigned light can differ significantly depending on whether, for example, Petrosian-like or Sersic-fit based magnitudes are extracted (see Bernardi et al. 2013, for details). To crudely mimic these uncertainties, we measure the predicted stellar light in the simulation also within different radii, and present the predicted total stellar light excluding satellites ( $L_*^{\text{tot}}$ ) as well as the light associated with the central galaxy ( $L_*^{<r_*}$ ), where  $r_*$  is our fiducial galaxy radius defined as twice the stellar half mass radius. Taking this into account we find reasonable agreement with the shape and normalisation of the observed luminosity function if we compare to recent Sersic-fit based GLFs (Bernardi et al. 2013).

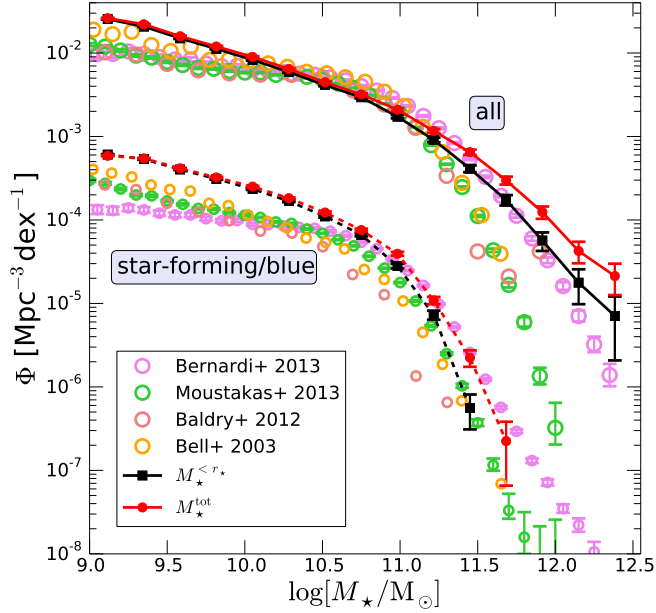


**Figure 11.** Galaxy stellar mass function (GSMF) compared to observationally derived values (Bell et al. 2003; Baldry et al. 2012; Moustakas et al. 2013; Bernardi et al. 2013). The star-forming GSMFs ( $\log[\text{SFR}/(\text{M}_\odot \text{yr}^{-1})] > -0.6 + 0.65 \log[M_*/10^{10} \text{M}_\odot]$ ) are shifted down by 1.5 dex for graphical clarity. We present the simulated GSMF using two measurements of stellar mass: total stellar mass excluding satellite contributions ( $M_*^{\text{tot}}$ ) and the central stellar mass ( $M_*^{<r_*}$ ) to compare with observations which are uncertain towards the massive end (see Bernardi et al. 2013, for details).

The abundance of faint galaxies follows a power-law whereas brighter galaxies are exponentially suppressed in their abundance (Schechter 1976). This shape is caused by scale-dependent feedback processes: Low mass systems are affected mostly by stellar SN feedback, whereas star formation in massive systems is suppressed through SMBH-related AGN feedback (Bower et al. 2006). Our model slightly overpredicts the number of massive and bright galaxies. This is related to the disagreement we found for the SFRD, and potentially caused by slightly insufficient AGN feedback. Measurements of the luminosity function hence provide important constraints on galaxy formation, and the agreement found here demonstrates that a self-consistent treatment of the physics that is thought to be relevant can indeed reconcile the rather different shapes of the CDM halo mass function and the galaxy luminosity function. We note that we find a similar level of agreement in the other bands (g,i,z), and therefore only show the simulation results in the inset panels.

Observationally, the GLF can be “directly” obtained. However, simulations have to make certain assumptions and use stellar population synthesis models to assign luminosities to stellar particles. Furthermore, the modelling of dust, which we neglected in our analysis, adds further uncertainties. Alternatively, stellar population synthesis models fitted to broadband spectral energy distributions can be used to transform an observed luminosity function into a galaxy stellar mass function (GSMF). This quantity can be straightforwardly compared to simulations, where the stellar masses of galaxies are a direct output.

Figure 11 adopts this complimentary view and compares the predicted GSMF to current observations (Bell et al. 2003;

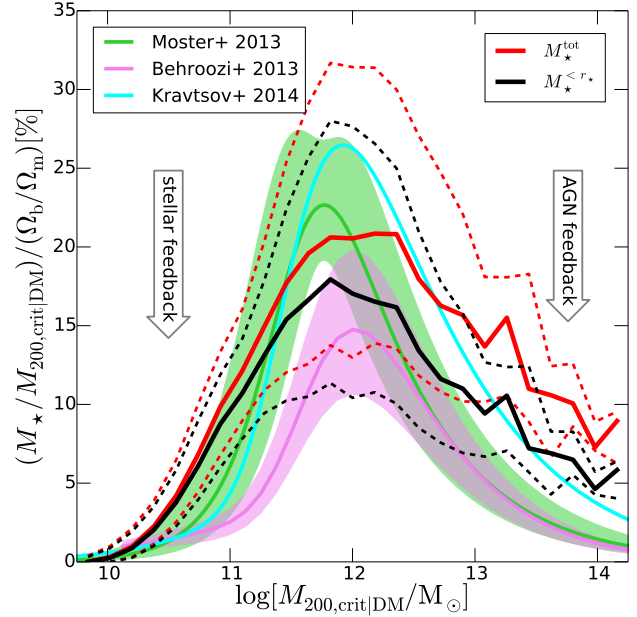


**Figure 12.** Stellar mass to halo mass ratio as a function of halo mass compared to observationally derived abundance matching results (Moster et al. 2013; Behroozi et al. 2013a; Kravtsov et al. 2014). The thick line shows the median simulation relation. The shaded areas show the  $1\sigma$  regions around the abundance matching relations, and dashed lines around the predicted ratio from the simulation.  $M_*^{\text{tot}}$  includes all stars except satellites, whereas  $M_*^{<r_*}$  includes only the stellar mass within  $r_*$ .

Baldry et al. 2012; Moustakas et al. 2013; Bernardi et al. 2013) based on data from SDSS, and the PRISM Multi-object Survey (PRIMUS) (Coil et al. 2011; Cool et al. 2013). To bracket uncertainties in the observational estimates for bright and massive galaxies (Bernardi et al. 2013) we calculate the total stellar mass excluding satellites ( $M_*^{\text{tot}}$ ) and for just the central stellar mass ( $M_*^{<r_*}$ ) for the simulated galaxies following the approach used above for the GLF. Given these uncertainties, the theoretically estimated stellar mass function agrees reasonably well with observations, even though the predicted faint end is slightly overpopulated around  $M_* \sim 10^9 \text{M}_\odot$ . We note, however, that these galaxies are relatively poorly resolved in the simulation (with only  $\sim 1000$  stellar resolution elements). The stellar mass function of star-forming galaxies with  $\log[\text{SFR}/(\text{M}_\odot \text{yr}^{-1})] > -0.6 + 0.65 \log[M_*/10^{10} \text{M}_\odot]$  also matches the observations (Moustakas et al. 2013) well. In particular, we recover the finding that the total galaxy stellar mass function at the massive end is almost entirely comprised of non-star forming galaxies. For  $M_* > 10^9 \text{M}_\odot$  we estimate that about 52% of all stellar mass at  $z = 0$  is in galaxies with a low SF rate, while observations (Baldry et al. 2004; Moustakas et al. 2013) report 54% – 60%. However, here we also find that the low mass end is even more pronounced for the SF population than for the total GSMF, indicating that we specifically over-produce star-forming galaxies at those masses.

Feedback and cooling processes control the baryon conversion efficiency from the gas phase to the stellar phase, and are required to match the GLF and GSMF. Regulating SF is therefore a key ingredient in modern galaxy formation simulations, since without feedback galaxies would have significantly too high stellar masses. Abundance matching techniques have over the last decade used

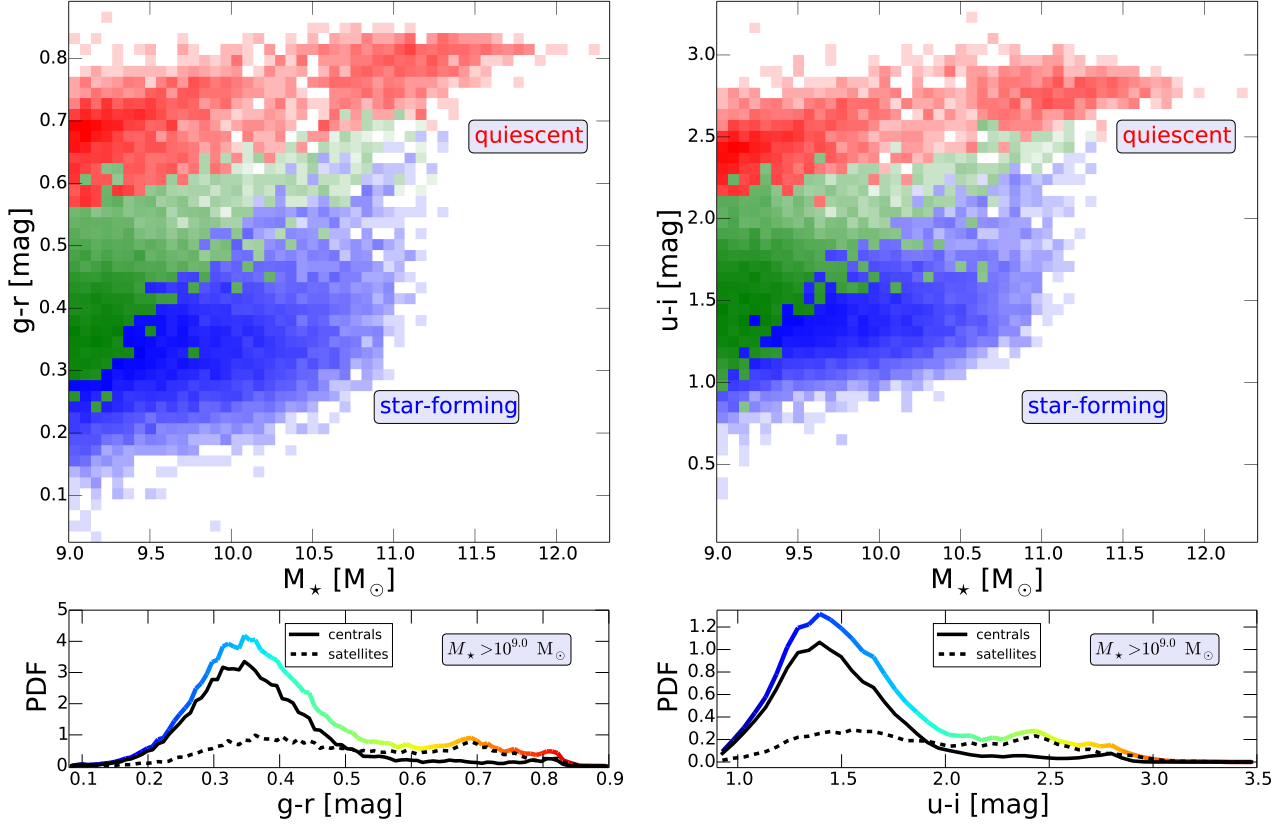


**Figure 13.** Distribution of  $g-r$  and  $u-i$  colours as a function of stellar mass. Top panels: Two-dimensional histograms showing galaxy  $g-r$  (left) and  $u-i$  (right) colour versus stellar mass. We do not take dust effects into account and only show intrinsic galaxy colours. The histograms are divided into three different galaxy populations: star-forming, quiescent, and a mixed region, where both types of galaxies occur. The distinction between star-forming and quiescent is made based on the star formation rate threshold employed above for the GSMF (see Figure 11). Bottom panels: Distribution of  $g-r$  (left) and  $u-i$  (right) colours for all galaxies with  $M_* > 10^9 M_\odot$  (coloured lines). The integrals over the histograms are normalised to one. The black dashed and solid lines split the total sample in centrals and satellites.

DM-only N-body simulations combined with large galaxy surveys like SDSS to constrain the expected baryon conversion efficiency as a function of halo mass. We present a comparison of our simulation to recent abundance matching estimates (Moster et al. 2013; Behroozi et al. 2013a; Kravtsov et al. 2014) in Figure 12. Here we show the stellar mass to halo mass ratio as a function of halo mass. Abundance matching results are derived by simultaneously ranking DM haloes obtained through DM-only N-body simulations and observed stellar masses. This implies, however, that a proper comparison to hydrodynamical simulations should be based on the relation of halo masses obtained from DM-only simulations and the associated stellar masses as predicted by the corresponding hydrodynamical simulation (Sawala et al. 2013; Munshi et al. 2013). We follow this procedure using the matched halo sample discussed above.

In Figure 12, we present therefore the stellar mass content of central galaxies in units of the universal baryon fraction ( $\Omega_b/\Omega_m$ ) as a function of the matched DM-only halo mass ( $M_{200,\text{crit}|DM}$ ) for our galaxy population at  $z=0$ ; the redshift evolution of this relation is presented in Genel et al. (in prep). Here, we use two stellar mass estimates: total ( $M_*^{\text{tot}}$ ) and the stellar mass contained within our fiducial galaxy radius  $r_*$  ( $M_*^{<r_*}$ ). This is to take again into account uncertainties in the stellar mass estimates for more massive systems (see Kravtsov et al. 2014, for more details). Figure 12 demonstrates that we find a reasonable agreement with the

abundance matching results; SF is most efficient close to the mass-scale of the Milky way ( $\sim 10^{12} M_\odot$ ), where the observationally inferred baryon conversion efficiency reaches  $\sim 20 - 30\%$  over a large redshift range. Lower and higher mass haloes have orders of magnitude smaller baryon conversion efficiencies so that most of the stellar mass is found in haloes around this mass scale. Reproducing this result is crucial, for example, for predicting the correct total amount of stellar mass in the Universe. Our simulation results are well within the  $1\sigma$  observational uncertainties (shaded regions) demonstrating that our feedback implementation leads to a stellar mass growth consistent with observations. The  $1\sigma$  regions of the simulation data are indicated through thin dashed lines. The abundance matching result of Kravtsov et al. (2014) agrees reasonably well with our results taking into account all stellar mass of haloes excluding the mass residing in satellites of the host.

We conclude that our feedback models both for SN and AGN feedback are sufficient to reduce SF roughly to the observed level. However, we stress that uncertainties in the stellar light assignment affect the GLF function and GSMF as discussed above. Since abundance matching techniques rely on observationally derived stellar mass estimates, we have to consider this effect also when comparing the stellar mass content of haloes to that derived through abundance matching. Taking these effects into account we find reasonable agreement for the GLF, the GSMF, and the amount of stellar

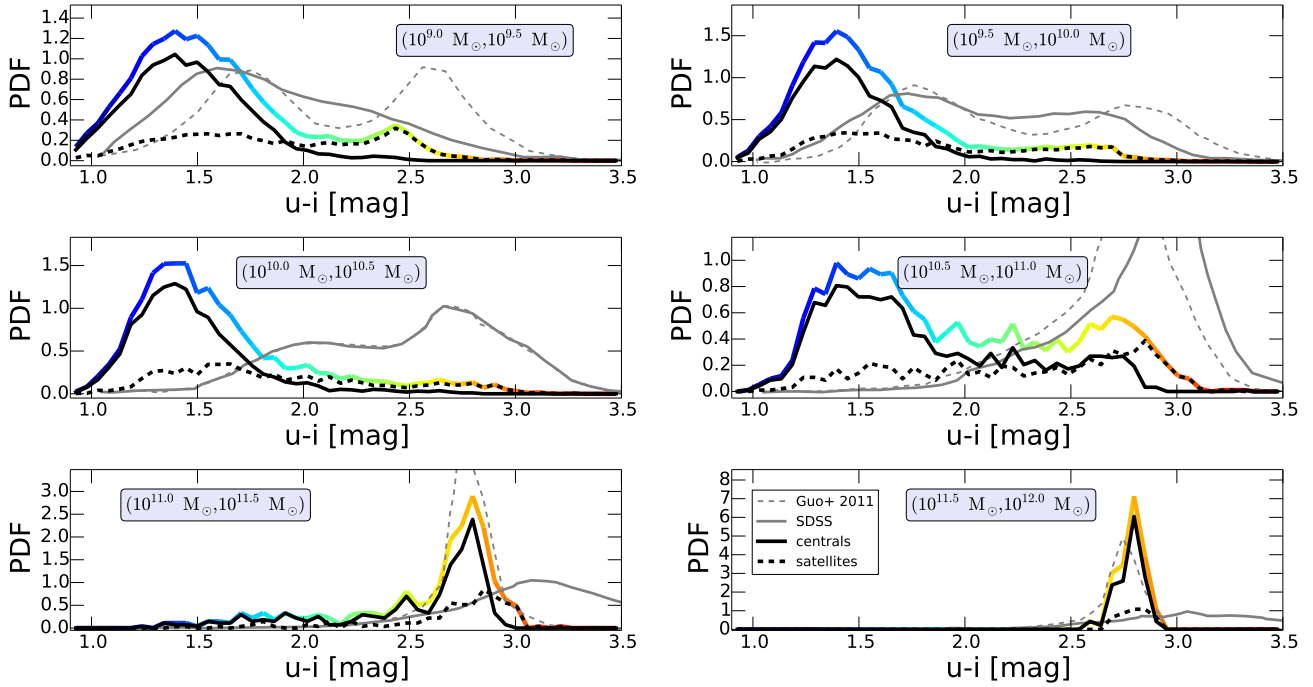


**Figure 14.** Distribution of  $u-i$  colours for galaxies split into bins of stellar mass ( $M_*$ ) as indicated. The integral over the histograms is normalised to one, and the coloured lines indicate the colour value. The distributions demonstrate that the simulated galaxy population clearly reddens towards the massive end. We note that the colours do not include the effects of dust reddening. We split the sample into centrals (black solid) and satellites (black dashed). We also show observational results based on SDSS (gray solid), and results from the semi-analytic model of Guo et al. (2011) (gray dashed).

mass for a given halo mass. Most importantly our model shows a maximum SF efficiency at the observationally inferred mass scale, which is achieved through the interplay of SN and AGN feedback.

We stress that it is dangerous to construct and tune galaxy formation models such that they exactly reproduce observations like the galaxy stellar mass function. For example, the systematic errors at the bright end of the galaxy stellar mass function have to be considered when constructing models. The same is true for matching the stellar to halo mass relationship. These relations are also uncertain at higher mass and different abundance matching results differ also towards lower halo masses. Most recently, Sawala et al. (2014) demonstrated that classical abundance matching breaks even down below halo masses of  $3 \times 10^9 M_\odot$ . It is therefore not advisable to construct large-scale galaxy formation models such, that they are tuned to reproduce these observations exactly.

## 4.2 Distribution of colours

Our simulation also predicts galaxy colours in different bands. In this first analysis we do not take into account dust effects on the emitted galaxy light and colours, but rather focus on the intrinsic color distributions. However, we note that dust can substantially affect colours of galaxies. The distribution of colours against stellar mass is shown in two-dimensional histograms in the two top panels of Figure 13, where we present the  $g-r$  colours (left) and  $u-i$  colours (right) as a function of stellar mass. We divide the histograms further in three different galaxy populations: star-forming (blue), quiescent (red), and a mixed region (green), where both types of galaxies occur. The distinction between star-forming and quiescent is made based on the star formation rate threshold employed for the GSMF above (see Figure 11). We stress that the three regions are strictly disjoint, e.g., the quiescent region (red) does not include any

star-forming galaxies (blue) according to our cut in the specific star formation rate. Green bins in Figure 13 contain both star-forming and quiescent galaxies. The histogram therefore illustrates that the reddest galaxies are typically quiescent, especially at the massive end, where all red galaxies are quiescent. However, there is also a substantial fraction of quiescent low mass galaxies, which are also red. On the other hand, star-forming galaxies are typically much bluer, and more biased towards less massive systems. In between these two regimes we identify a narrow region where we find both types of galaxies: quiescent and star-forming.

The coloured lines in the bottom panels of Figure 13 show one-dimensional distributions of  $g-r$  colours (left) and  $u-i$  colours (right) for all galaxies with  $M_* > 10^9 M_\odot$ , i.e. galaxies resolved with more than  $\sim 1000$  stellar resolution elements. All histograms are normalised such that the integral over the distribution sums up to unity. The simulation predicts a slightly bimodal distribution both in  $g-r$  and  $u-i$  colours. However, the second maximum for red galaxies in both distributions is not as pronounced as found in observations (e.g., Blanton et al. 2005a). This can be caused by different effects probably related to quenching in massive haloes.

Firstly, it seems that our radio-mode AGN feedback is not efficient enough to suppress SF sufficiently in massive haloes as mentioned above. Too little quenching can lead to stellar populations which are too young and therefore biased towards bluer colours. A second reason for the less pronounced second maximum lies potentially in the rather small sample of massive objects in our simulation volume. For example, we have only ten haloes with masses above  $10^{14} M_\odot$  (C-1 to C-10, see above). The massive part of the galaxy population is therefore not captured well, and could potentially be biased due to the initial density field that is sampled by the simulation. A final reason is related to the effects of dust, which renders galaxies redder than intrinsically expected. Since we do not



include this effect here, we naturally find a smaller number of red galaxies. Also the maximum “redness” of galaxies is expected to be lower compared to real galaxies. Only the first of these three reasons is inherent to our model, and it remains to be seen whether other mechanisms or a different AGN radio-mode model need to be introduced to quench SF more efficiently in massive systems like groups and clusters. Assuming that the second and third reasons are not the main driver of the discrepancy, our results seem to indicate that radio-mode AGN feedback alone may not be sufficient to quench massive haloes enough. However, the exact duty cycle of the radio-mode will also affect this behaviour. Below, we will demonstrate a fourth possibility, namely that the quenching and reddening of intermediate mass haloes is also not sufficiently strong in our model.

The bottom panels of Figure 13 also split the galaxy population into centrals (solid black line) and satellites (dashed black line). Here we find that the red part of the distribution is actually dominated by satellite galaxies, and not by centrals. Centrals clearly dominate the blue part of the distribution. To inspect this behaviour further we show in Figure 14  $u-i$  colour distributions for different stellar mass cuts going from low to higher mass systems (coloured lines). Our results agree qualitatively with observations in the sense that more massive systems tend to have significantly redder colours compared to low mass systems. In fact, the most massive systems included in Figure 14 peak around  $u-i \sim 2.8$ . The  $10^{10.5} M_{\odot}$  to  $10^{11.0} M_{\odot}$  mass range shows a clear bimodal distribution with broad maxima at  $u-i \sim 1.5$  and  $u-i \sim 2.75$ . We split all distributions again into centrals (solid black) and satellites (dashed black), and find that the general trend is that the red population at low stellar masses is made up by satellite galaxies, whereas centrals dominate the red population towards higher stellar masses. Centrals start to become more relevant in the red part of the distribution above  $M_{\star} \gtrsim 10^{10.5} M_{\odot}$ .

Although we do not include dust effects, we also show observational SDSS results (thin gray lines) in the different panels of Figure 14. This reveals another qualitative agreement of our model with observations: only intermediate mass galaxies show a bimodal distribution. Despite the fact that we do not include dust effects, we find for some mass ranges reasonable agreement with the observed colour distribution. However, in the intermediate mass regime the predicted quantitative colour distribution clearly deviates from the observed samples. Here we miss a significant fraction of red and quenched galaxies, which are observed, but not present in our model. This relates to the fourth reason for why our total colour distribution is not as bimodal as found observationally: we miss a significant fraction of red and quenched galaxies in the intermediate mass range. A similar conclusion is reached by looking at the quenched fraction as a function of galaxy mass (see Genel et al., in prep).

We have also added model predictions from Guo et al. (2011) based on a semi-analytic model run on the Millennium-I and -II simulations N-body simulations. At higher masses our simulation results agree well with the semi-analytic predictions from Guo et al. (2011). However, both models tend to produce too few red galaxies at the massive end, and the maximum  $u-i$  values agree well between the two models, but are too low compared to observations. Furthermore, both models predict a rather narrow and peaked distribution, which is not observed. Instead in the massive mass bins observations favor a broad distribution extending to  $u-i$  colours larger than 3.5. At lower masses we find galaxies which are bluer than observationally found, but dust effects can in principle compensate for this.

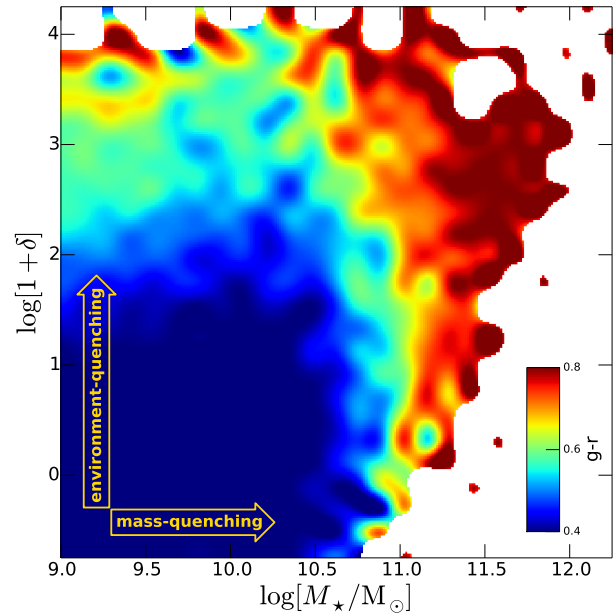


**Figure 15.** Average  $(g-r)$  colour of galaxies as a function of stellar mass and galaxy overdensity  $1 + \delta$ . We find mass-quenching along the horizontal axis and environment-quenching along the vertical axis. Along both axes galaxies tend to become redder. The overdensity field  $(1 + \delta)$  is based on the fifth nearest galaxy considering only systems with  $r < -19.5$ .

### 4.3 The impact of environment

As demonstrated above, SN and AGN feedback are key processes in regulating SF and in determining the stellar mass content of haloes. However, many studies have also established the view that the evolution of galaxies is a strong function of environment, both observationally (e.g., Hogg et al. 2003; Kauffmann et al. 2004; Blanton et al. 2005a; Baldry et al. 2006; Peng et al. 2010) and theoretically (e.g., Crain et al. 2009), based on various measures used to quantify galaxy environments (see Haas et al. 2012, for an overview). Galaxies entering high density regions like clusters are prone to processes like ram pressure stripping, starvation, strangulation, and tidal stripping, which are captured self-consistently by hydrodynamical simulations, a major advantage over ad hoc treatments employed in semi-analytic models. These physical processes are significant because they influence, for example, the SF rates and colours of galaxies as a function of environment.

We demonstrate this in Figure 15, where we present the average  $(g-r)$  colours of galaxies as a function of stellar mass and local galaxy overdensity  $1 + \delta$  at  $z = 0$ . The overdensity field is calculated based on the fifth nearest galaxy considering only systems with  $r$ -band magnitude  $< -19.5$  for the construction of the galaxy density field at  $z = 0$ . This leaves us with 11, 112 galaxies from which we calculate the local overdensity field  $(1 + \delta)$  for each other galaxy that we can correlate with other galaxy properties. We note that this procedure is commonly adopted in observational studies (e.g., Peng et al. 2010). Figure 15 demonstrates that galaxies tend to be redder at larger stellar masses and at higher galaxy overdensities, in accord with observations. These two “reddening axes” are however related to entirely different physical processes. Quenching of massive galaxies proceeds mostly through AGN feedback in large haloes, which is associated with the heating and removal of large amounts of interstellar gas so that star forma-

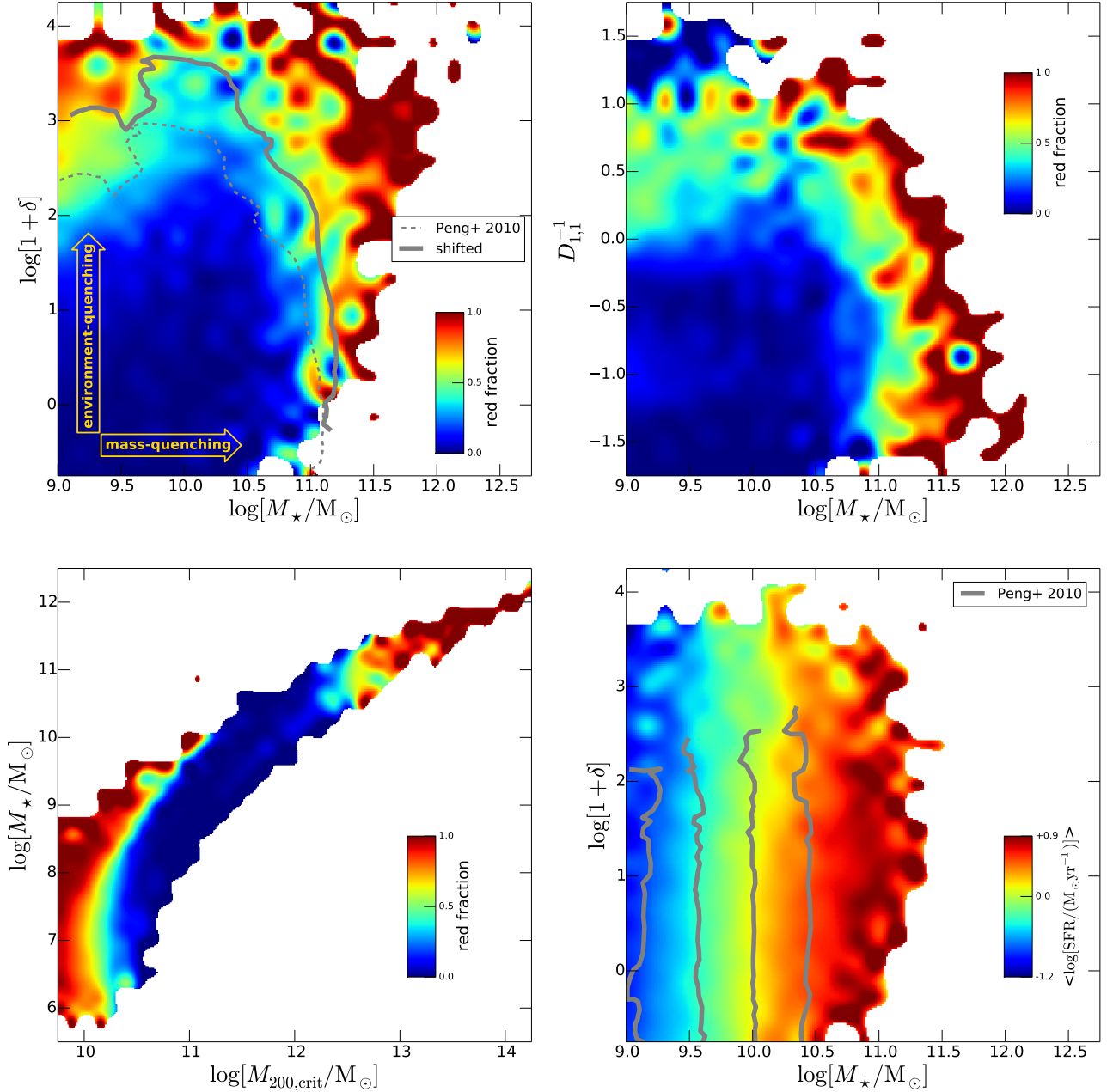


**Figure 16.** Environmental dependence of the galaxy population. Upper left panel: Red fraction of galaxies as a function of stellar mass and galaxy overdensity. Reddening occurs along the mass and overdensity axes. We also include observational contour lines for a red fraction of 0.9 from Peng et al. (2010) (dashed). The shifted solid line represents a mass and overdensity shift to better fit our data. Upper right panel: Red fraction of galaxies as a function of stellar mass and galaxy overdensity, but now using a theoretically motivated environment estimator described in Haas et al. (2012), which has only little halo mass dependence. Lower left panel: Stellar mass as a function of halo mass colour coded according to red fraction. SF is most efficient around  $M_{200,\text{crit}} \sim 10^{12} M_\odot$  where we find blue star forming galaxies sitting on the SF main sequence. Lower right panel: Mean SF rate as a function of stellar mass and galaxy overdensity. We include here only star forming galaxies. For these, the SF does not depend on  $\delta$ , but instead is a pure function of stellar mass through the SF main sequence. Observational contour lines from Peng et al. (2010) are also shown, and those tend to show no dependence on the overdensity either. Combined with the findings in the other panels this implies that the rate of SF does not depend on environment, but the probability of a galaxy being quenched and becoming redder does.

tion ceases and the galaxy starts to redden as its stellar population ages. Environmental quenching due to denser surroundings primarily affects lower mass satellite galaxies, which are stripped of their gas as they experience ram pressure when falling into larger haloes.

Next we explore more quantitatively the dependence of the

red fraction on stellar mass and  $1 + \delta$  in the upper left panel of Figure 16. Here we present the un-weighted average red fraction in each bin with a threshold of  $(g - r) = 0.65 - 0.03(r + 20)$  (see Blanton et al. 2005b). The results again demonstrate that galaxies tend to be redder for larger stellar masses and higher galaxy

overdensities as defined through  $1 + \delta$ . We stress that the trends we recover in this panel are qualitatively in good agreement with recent observations (e.g., Peng et al. 2010). To make this clearer we also include observational contour lines for a red fraction of 0.9 from Peng et al. (2010). The dashed line is the original result from Peng et al. (2010), whereas the shifted line represents a mass and overdensity shift to fit better to our data. The observational contour line was defined based on a different galaxy overdensity  $1 + \delta$ , and a different definition of red fraction. We have therefore shifted this line by  $+0.1$  dex in mass, and  $+0.7$  dex in overdensity. Interestingly, this brings the general shape of the contour line into good agreement with our results. Most importantly, we recover the drop in the red fraction around  $M_* \sim 10^{10} M_\odot$  at higher overdensities.

Many of the observationally employed overdensity estimators do not strictly probe the galaxy environment. In fact, it has been pointed out that most of the common environment indicators, among them  $1 + \delta$ , are to some degree correlated with halo mass (see Haas et al. 2012). They are therefore not strictly probing environmental effects, but are “contaminated” also by the halo mass dependence. Other characteristics of probing the impact of the environment on galaxy properties have therefore been proposed by Haas et al. (2012).

We consider this in the upper right panel of Figure 16, where we use  $D_{1,1}$ , the three-dimensional distance to the nearest neighbour with a virial mass that is at least that of the halo under consideration, divided by the virial radius of the nearest neighbour, to probe the environment (see Haas et al. 2012, for more details). This estimator aims to minimise any halo mass dependence in the direction of the vertical axis. Using this estimator we still recover two different quenching mechanisms: mass-quenching along the horizontal axis and environment-quenching along the vertical axis. Although the upper left and upper right panels of Figure 16 look similar, they differ in the dependence of the red fraction as a function of  $1 + \delta$  and  $D_{1,1}$  for fixed stellar masses around  $M_* \sim 10^{10} M_\odot$ . The estimator  $D_{1,1}$  does not show an equally strong drop in the red fraction towards higher overdensities compared to  $1 + \delta$ . This might be related to the fact that  $1 + \delta$  is still contaminated by a remaining halo mass dependence as pointed out by Haas et al. (2012). Interestingly, the two upper panels of Figure 16 also differ at the highest overdensities and lowest masses, but in the opposite direction: the  $D_{1,1}$  measure has its upper-left corner very blue again, which is not the case for  $1 + \delta$ .

The lower left panel of Figure 16 combines the stellar mass halo mass relation and the fraction of red galaxies. SF is most efficient around  $M_{200,\text{crit}} \sim 10^{12} M_\odot$  where the galaxy population is dominated by blue star forming galaxies which populate the SF main sequence (see below). Towards lower and higher masses, SF becomes less efficient and the fraction of red galaxies increases in both directions due to quenching, which is consistent with observations (Woo et al. 2013). Although the red fraction depends on environment, it is observationally found that the SF rate of star forming galaxies does not depend on  $1 + \delta$ , but only varies as a function of mass in the  $M_* - \delta$  plane (Peng et al. 2010). The lower right panel of Figure 16 demonstrates that we recover the same trend in the simulation. Here we present the average SF rate as a function of stellar mass and galaxy overdensity  $1 + \delta$  for star-forming galaxies using the same cut as discussed above (see discussion of the GSMF, and colours). Gray lines in the lower right panel represent contour lines from Peng et al. (2010). These lines are essentially parallel to the contour lines predicted by the simulation demonstrating that our model describes the observational finding correctly. We note that this result is not in conflict with those presented in the upper

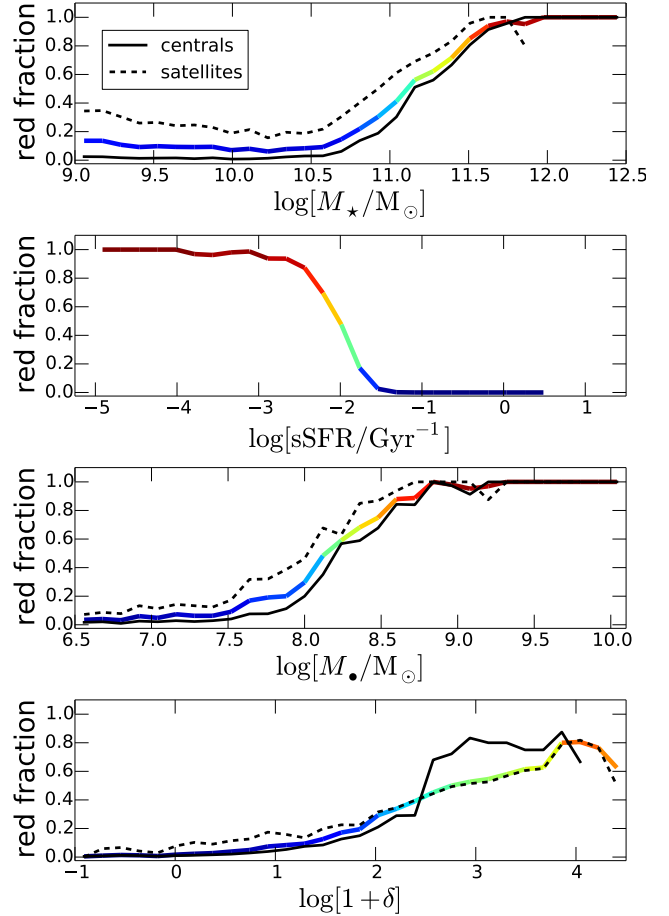


**Figure 17.** Red fraction as (from top to bottom) a function of stellar mass, specific SFR, BH mass, and galaxy overdensity for all galaxies more massive than  $10^9 M_\odot$ . The coloured line represents the total galaxy population, whereas the solid and dashed black lines denote centrals and satellites, respectively. The colour of the line simply reflects the red fraction on the y-axis. The dependence of the red fraction on sSFR does not show any strong dependence on galaxy type (centrals and satellites), and we do therefore not include the central and satellite lines.

panels. The fact that the red fraction of galaxies increases with  $1 + \delta$  combined with a  $1 + \delta$ -independent SF rate only implies that the SF rate itself does not depend on environment, whereas the quenching and reddening probability is a strong function of environment. Both observationally and theoretically this points towards a rather rapid process that quenches and reddens galaxies in higher density environments.

We summarise the dependence of the galaxy red fraction on the stellar mass, the specific star formation rate, the BH mass, and galaxy overdensity in the four panels of Figure 17. The coloured line represents the total galaxy population, whereas the solid and dashed black lines denote centrals and satellites, respectively. The dependence of the red fraction on sSFR does not show any strong dependence on the galaxy type (centrals and satellites), and therefore we do not include the central and satellite lines. Figure 17 reveals some clear trends of the red fraction.

The first panel emphasises the strong increase of the red fraction with increasing stellar mass. As emphasised above red galaxies have typically only little ongoing SF which can also be seen from the second panel. Here we find a rather steep drop of the red fraction around a specific SFR of about  $\sim 10^{-2} \text{ Gyr}^{-1}$ . Below (above)

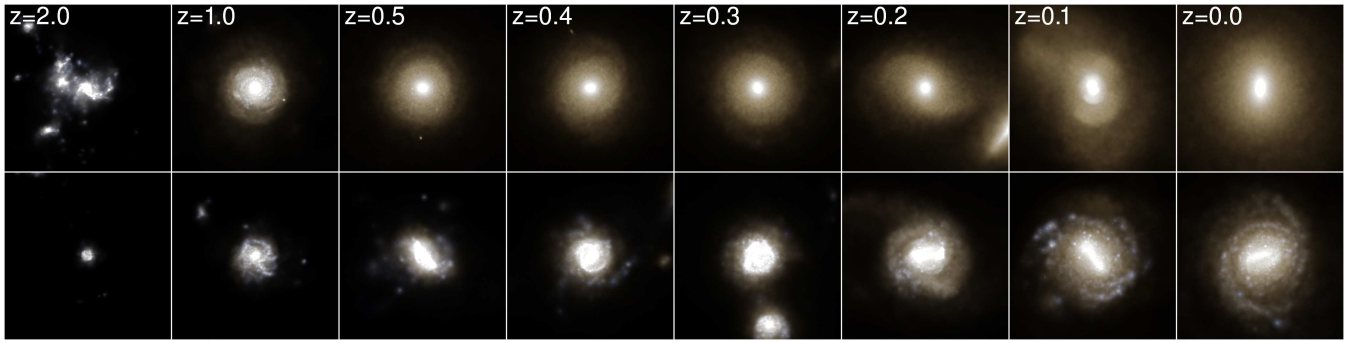


**Figure 18.** Evolution of two selected galaxies across cosmic time. The images show rest-frame  $g,r,i$  band composite images of the stellar light for the two galaxies at various redshifts as indicated. The top galaxy evolves into a red elliptical galaxy, which has only very little remaining star formation at  $z = 0$ . The bottom galaxy evolves into a blue star-forming spiral with a bar-like structure in the center. Both galaxies experienced recent mergers, which leads to the formation of shells in the stellar light distribution of the elliptical galaxy. The merger of the blue galaxy leads to the formation of a central bar. Both galaxies are distinct at  $z = 0$  in their morphology, their colour, and their present star formation rate. At higher  $z$  both galaxies are significantly bluer.

this threshold, we find only a low number of blue (red) galaxies. Also as discussed above AGN feedback of SMBHs plays an important role in quenching star formation towards more massive halo masses. It is therefore not surprising that the red fraction increases with black hole mass as shown in the third panel. The galaxy environment also shapes the galaxy colours and affects the red fraction as demonstrated above. The last panel of Figure 17 demonstrates this clearly. Interestingly, the red fraction in centrals and satellites differs significantly towards higher overdensities. For an observationally employed density estimator like  $1 + \delta$  we find that around  $1 + \delta \sim 10^3$  centrals tend to be significantly redder than satellites of the same overdensity.

The results in this section demonstrate that SF formation, quenching, and reddening are deeply connected through feedback processes and environment effects, most of which are recovered by our model reasonably well.

## 5 CHARACTERISTICS OF INDIVIDUAL GALAXIES

Although our effective ISM model prevents us from making detailed predictions about the internal gas structure of galaxies, we can still estimate coarse grained quantities, and test those predictions against observations. We will demonstrate this in what follows for a few observables, and we will also show that our model produces a reasonable mix of early- and late-type galaxies. Furthermore, the more massive galaxies in our simulation volume are resolved well enough to study the detailed distribution of stars in them.

Before studying specific details of the galaxy population we present in Figure 18 the redshift evolution of two galaxies based on stellar images in rest frame  $g,r,i$  bands. One of the galaxies evolves into a red elliptical galaxy (top), and the other one (bottom) into a blue star-forming spiral galaxy. We trace these galaxies back in time for more than 10 Gyr until  $z = 2$  as indicated in the figure. The images reveal that both galaxies undergo some mergers. For example the red galaxy experienced a dry merger around  $z \sim 0.2$  resulting in shell like structures in the stellar image at  $z \sim 0.1$ . The shells are not prominent anymore at  $z = 0$ , where we find a smooth and featureless light distribution. The blue late-type galaxy in the bottom of the figure also undergoes a merger around  $z \sim 0.3$  resulting in the formation of a dominant bar, which is clearly visible around  $z \sim 0.2 - 0.1$  and still noticeable at  $z = 0$ . Some of the

blue galaxy’s images also show star-forming regions as knots in the light distribution. By  $z = 0$  these systems have evolved into very different galaxies, which differ strongly in their morphology, colour, and specific star formation rates.

We trace the history of these two galaxies more quantitatively in Figure 19, where we show their evolutionary paths together with the distributions of all galaxies at  $z = 0$ . In the left panel of Figure 19 we present the distribution of all galaxies as a function of stellar mass and SF rate at  $z = 0$ . The colour coding in the histogram shows the average  $(g-r)$  colour of galaxies in each bin. The green band shows the observed SF main sequence (Elbaz et al. 2007) which is in good agreement with the predictions of our model. We also include the evolutionary paths of the two galaxies shown in Figure 18. The early-type red galaxy (circle symbol) shows a rapid late-time drop in SF, which is absent for the blue galaxy (star symbol). This is caused by quenching through radio-mode AGN feedback. The star formation rate decreases by more than one order of magnitude from  $z = 0.8$  to  $z = 0.4$  ( $\Delta t \sim 2.6$  Gyr) and subsequently by a similar factor from  $z = 0.4$  to  $z = 0.2$  ( $\Delta t \sim 1.9$  Gyr) at which point SF of the central galaxy shuts off completely, which is why we show no data point for the early-type galaxy at  $z = 0$ . The colour of the symbols indicates the actual  $g-r$  colour of the galaxy at the particular time. One can clearly see how the elliptical galaxy reddens while its SF is reduced by feedback. On the other hand, the blue galaxy has  $g-r \sim 0.4$  until about  $z \sim 0.2$ . Then SF is slightly reduced and the galaxy turns slightly redder, but is still significantly bluer than the red elliptical at late times. The symbol sizes for the two galaxies are proportional to the stellar half mass radius normalised for each galaxy evolution track individually. The red galaxy seems to grow substantially from  $z = 0.4$  to  $z = 0.2$ . This is due to the dry merger happening around that time leading to a more extended stellar distribution. The growth of the blue galaxy is less dramatic, but it also grows continuously until  $z = 0$ .

The right panel of Figure 19 shows the central gas fraction ( $M_{\text{gas}}/(M_{\star} + M_{\text{gas}})$ ) as a function of stellar mass. The colour coding indicates the average specific SF rate in each bin. As galaxies become more massive, their gas content is reduced by AGN feedback and, as a result, star formation becomes less efficient. The left panel demonstrates that this is accompanied by a reddening of the galaxy (increasing  $(g-r)$  values). This effect can also be seen visually in Figure 18: both galaxies are blue at earlier times owing to their young stellar populations and ongoing star formation.



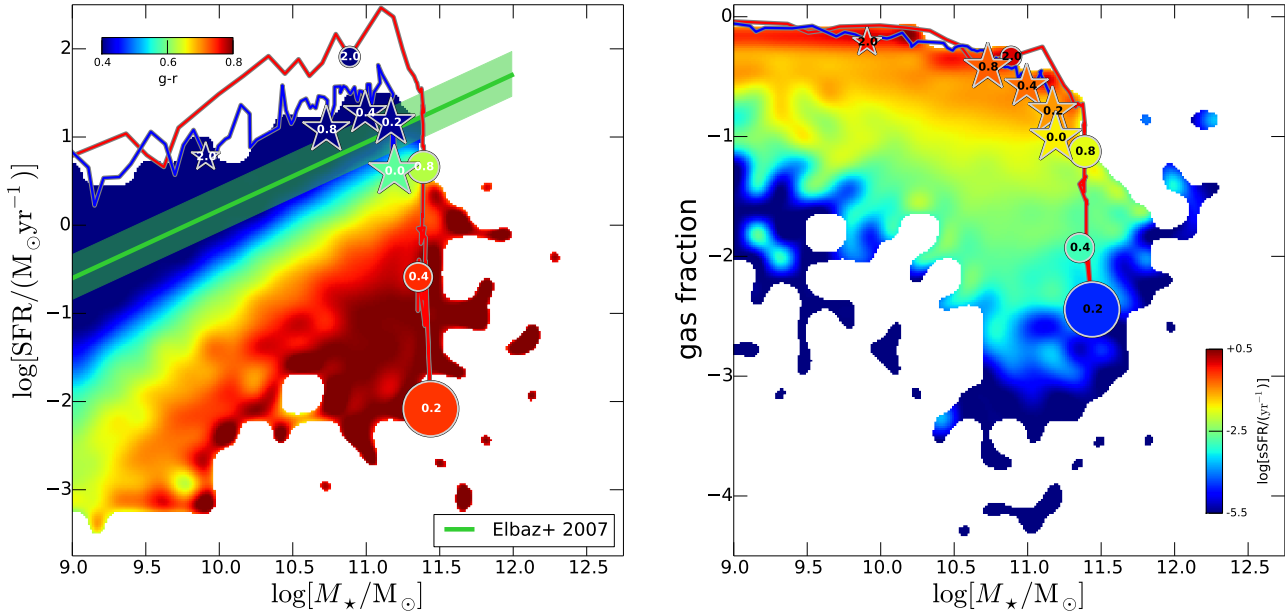


**Figure 19.** Galaxy evolution across cosmic time. Left panel: Star formation rate versus stellar mass at  $z = 0$  ( $g-r$  colour coded). The green band shows the observed SF main sequence (Elbaz et al. 2007). Symbols connected by lines trace the evolution of the two sample galaxies shown in Figure 18: one evolving into an elliptical (circles / red line) and the other one ending as a disk galaxy (stars / blue line). Numbers in the symbols show the redshift and the symbol colour represent the galaxy’s  $g-r$  colour. Symbol sizes are proportional to the stellar half mass radius normalised for each galaxy evolution track individually. Right panel: Central gas fraction versus stellar mass at  $z = 0$  (specific SF rate colour coded). Symbol colours are chosen according to the specific SF rates. We do not show the elliptical galaxy beyond  $z = 0.2$  since the SFR is essentially zero after that time. Symbol sizes in the right panel are the same as in the left panel.

Feedback quenches star formation in the more massive system and leads to reddening towards  $z = 0$ . Both the gas fraction and the central gas content drop quickly from  $z = 0.8$  to  $z = 0.2$  along with a significant reduction of the specific star formation rate. At early times both galaxies have an approximately constant gas fraction (right panel) along with a slowly increasing star formation rate (left panel).

Figure 18 and Figure 19 demonstrate two different evolutionary tracks of galaxies, which lead to a very distinct galaxy type at  $z = 0$ . We stress that these differences in the evolutionary history are largely driven by the feedback processes included in our model. Specifically, the late time evolution of the early-type galaxy is strongly influenced by energetic radio-mode AGN feedback. Such processes are therefore responsible for producing a diverse galaxy population at  $z = 0$  in our simulation.

At  $z = 0$  Illustris-1 contains 41,416 galaxies which are resolved with more than 500 stellar particles. For many coarse-grained galaxy properties like total metal content (see Vogelsberger et al. 2014b) or total luminosity  $\sim 1000$  particles are typically enough to get reasonable estimates. For example, we can reliably probe the GLF down to this mass limit. However, quantifying the internal structure of the stellar and gas distribution requires significantly more resolution elements to achieve accurate results. For example, probing the internal velocity structure, morphology or detailed sizes of galaxies requires substantially more resolution elements than a few thousand. The resolution of Illustris-1 is therefore only sufficient to roughly describe the morphology and internal kinematics of the more massive galaxies  $M_* \gtrsim 10^{10-11} M_\odot$  where the stellar population is sampled by about  $\sim 10^4 - 10^5$  stellar particles. Although this resolution is still rather low compared to state-

of-the-art zoom-in simulations, we will demonstrate below that internal characteristics of galaxies like the circular velocity curves are described reasonably well with this resolution. Specifically, we will inspect in the following the structure of a few well-resolved galaxies.

We present a sample of “by eye” selected “blue” and “red” central galaxies in Figure 20 (blue) and Figure 21 (red). These images show composite  $g,r,i$  SDSS-band light distributions. Most of the blue galaxies are star-forming disk galaxies, whereas most of the red galaxies in the sample are ellipticals with only little or essentially no ongoing SF. We refrain from showing a larger sample here, but illustrate the basic features of our galaxy population based on these two samples. The composite images of the blue galaxies (B-1 to B-42) in Figure 20 reveal several interesting features. Firstly, the sample includes barred and non-barred spirals. Star-forming regions in spiral arms clearly stand out as blue connected knots. The opening angle and winding of the spiral arms varies similarly to what is found observationally along the Hubble sequence. Interesting features can also be found in the light distribution of the redder galaxy sample (R-1 to R-42) in Figure 21. Since we did not make any cuts on morphology some galaxies appear to have disk like features. A few of the galaxies like R-2, R-7, and R-11 show shell like structures. Most likely these are remnants of recent dry mergers as discussed above.

Some characteristics of these galaxies are summarised in Table 3, where we list virial masses, stellar masses, SMBH masses, star formation rates, specific star formation rates, ( $g-r$ ) colors,  $r$  band magnitudes, and local galaxy overdensities. One can also see that the selected red objects are on average more massive and brighter ( $r$  band magnitude). Furthermore, the ( $g-r$ ) color values are,

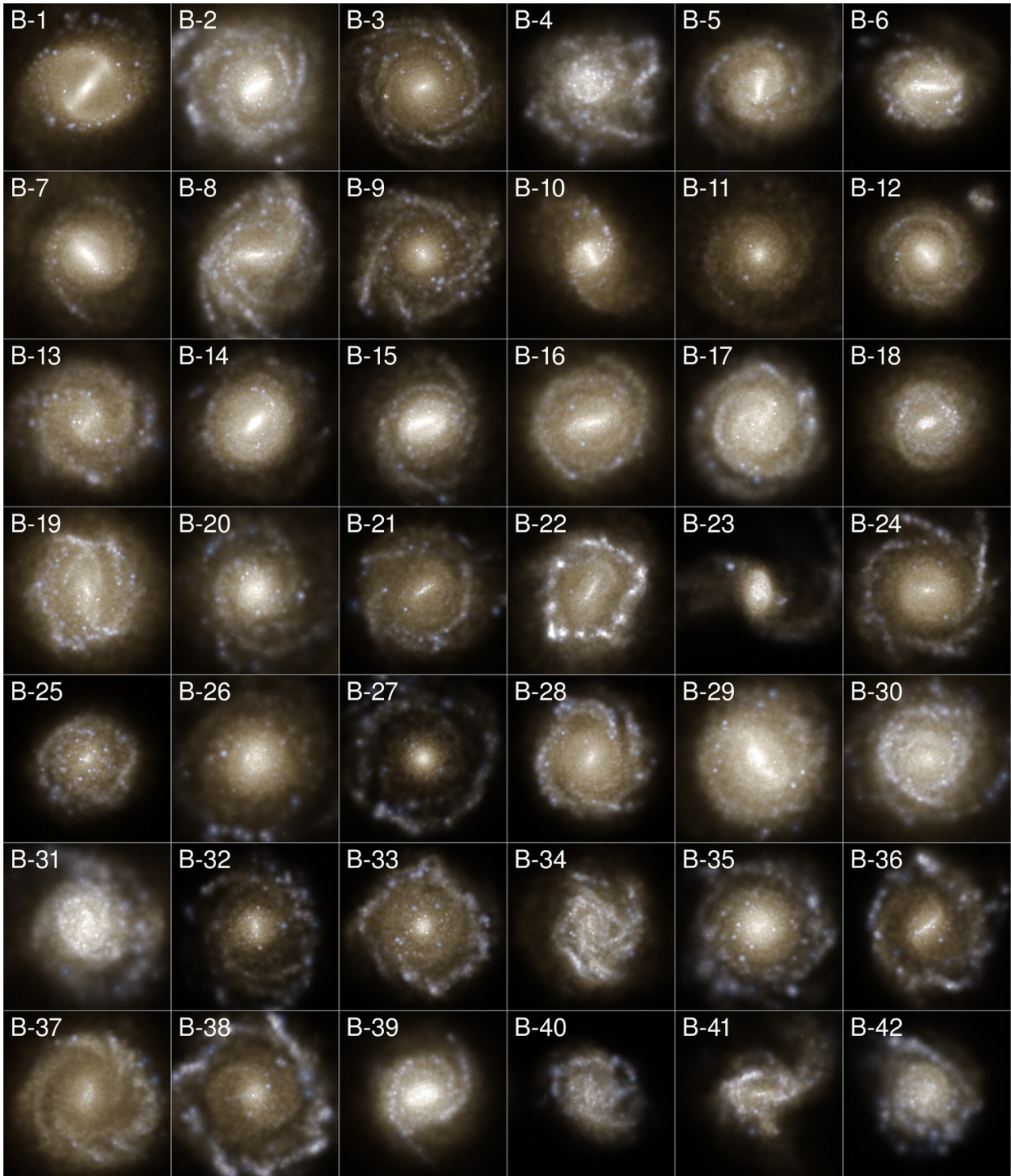


**Figure 20.** Blue galaxies: Stellar light distribution (g,r,i SDSS band composites) of a few selected blue galaxies. These blue galaxies have typically high present-day SF rates and most of them are disk-like. Basic characteristics of these galaxies are listed in Table 3. The blue star-forming ‘rings’ in some galaxies are star-forming regions, which are exaggerated in significance due to the employed colour scale.

by selection, also consistently higher for the red sample compared to the blue galaxies. The reddening of the red galaxies is due to quenched SF which leads to the older stellar population and therefore redder stellar light. The red galaxies have massive SMBHs which cause AGN feedback, a key process in quenching massive systems. In fact, the SMBH population for the blue galaxies is sig-

nificantly less massive than the population of the red galaxies. We note that some of the red massive systems are quenched so strongly that they have essentially no on-going star formation anymore (e.g., R-2, R-3, etc.). Galaxies are ordered by halo mass in Table 3. Blue galaxies listed below B-33 are Milky Way-like galaxies in terms of halo mass. Most of these galaxies host SMBH which are signifi-



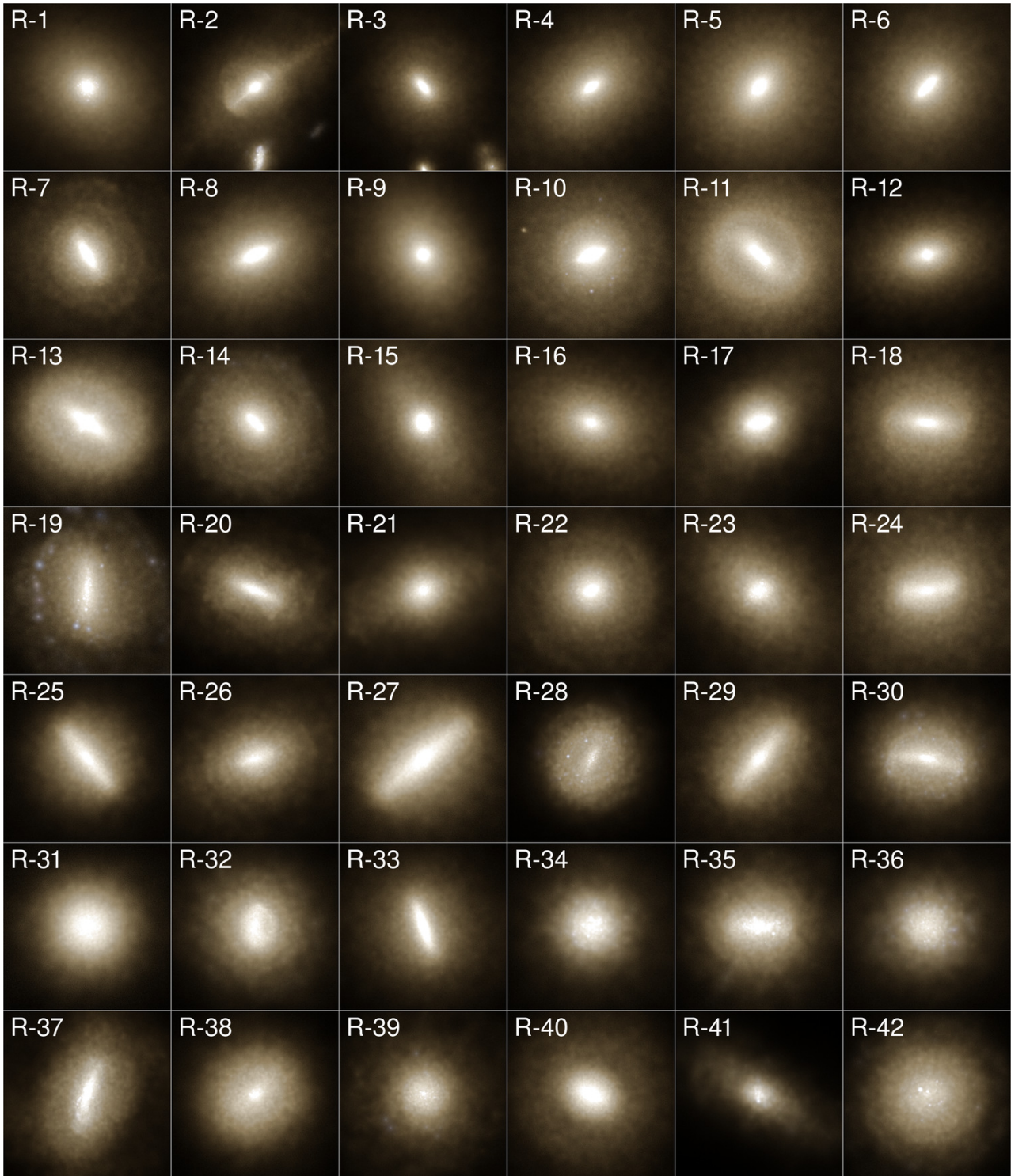


**Figure 21.** Red galaxies: Stellar light distribution (g,r,i SDSS band composites) of a sample of red galaxies. Most of the red galaxies have little on-going SF and are ellipticals. Basic characteristics of these galaxies are listed in Table 3. Some of the galaxies (e.g., R-2, R-7, and R-11) show shell-like structures in the stellar light distribution.

cantly more massive than the SMBH at the Galactic center. Only B-40 has a relatively low SMBH mass of about  $9 \times 10^6 M_{\odot}$ . All other blue galaxies in the Milky Way's halo mass regime have more massive SMBHs.

The galaxies presented in Table 3 all have stellar masses above  $10^{10} M_{\odot}$ , and most of them have  $M_{\star} \gtrsim 10^{11} M_{\odot}$ . This

means that the stellar population in these systems is resolved with  $\sim 10^5$  resolution elements. As argued above, this resolution is sufficient to explore the internal structure of the galaxies. We demonstrate this by inspecting the internal mass structure of some of the blue galaxies by constructing circular velocity profiles,  $V_{\text{circ}}(r) = \sqrt{GM(< r)}/r$ . The results are presented in Figure 22. There we

galaxy	$M_{200,\text{crit}}$ [ $10^{12} M_{\odot}$ ]	$M_{\star}$ [ $10^{11} M_{\odot}$ ]	$M_{\bullet}$ [ $10^8 M_{\odot}$ ]	SFR [ $M_{\odot} \text{ yr}^{-1}$ ]	$\log[\text{sSFR}/\text{Gyr}^{-1}]$	g-r [mag]	r [mag]	$\log[1 + \delta]$
B/R-1	11.07 / 59.21	2.92 / 6.19	10.53 / 25.16	2.3718 / 1.0746	-1.09 / -1.76	0.72 / 0.75	-23.38 / -24.30	2.41 / 2.83
B/R-2	10.51 / 41.60	1.97 / 4.60	2.68 / 17.42	10.8637 / 0	-0.26 / ---	0.53 / 0.76	-23.58 / -24.00	3.65 / 3.47
B/R-3	7.69 / 36.50	2.69 / 3.80	2.20 / 32.63	4.5586 / 0	-0.77 / ---	0.65 / 0.75	-23.56 / -23.74	1.95 / 3.13
B/R-4	5.46 / 26.69	0.73 / 4.02	0.15 / 41.81	11.9022 / 0	0.21 / ---	0.35 / 0.77	-22.82 / -23.67	0.63 / 2.25
B/R-5	5.13 / 24.87	1.17 / 5.41	1.48 / 36.30	2.1489 / 0.0235	-0.74 / -3.36	0.60 / 0.79	-22.87 / -23.95	0.89 / 2.46
B/R-6	4.60 / 24.62	1.57 / 3.97	1.25 / 19.64	7.7917 / 0	-0.30 / ---	0.54 / 0.77	-23.33 / -23.77	1.22 / 3.21
B/R-7	4.57 / 19.79	1.87 / 2.23	3.03 / 18.86	1.8975 / 0.0393	-0.99 / -2.75	0.68 / 0.76	-23.35 / -23.13	0.51 / 2.24
B/R-8	4.45 / 16.50	1.40 / 3.13	0.66 / 16.82	9.9469 / 0	-0.15 / ---	0.50 / 0.77	-23.26 / -23.51	3.00 / 2.58
B/R-9	4.24 / 14.19	1.09 / 3.40	1.69 / 22.86	4.0928 / 0.0162	-0.43 / -3.32	0.56 / 0.79	-22.51 / -23.45	0.70 / 2.20
B/R-10	4.13 / 14.03	0.93 / 3.85	2.07 / 23.22	1.2217 / 0.2478	-0.88 / -2.19	0.69 / 0.78	-22.28 / -23.78	2.58 / 1.80
B/R-11	3.81 / 12.40	1.10 / 4.92	2.50 / 11.94	0.6194 / 0.1505	-1.25 / -2.51	0.67 / 0.79	-22.44 / -23.82	1.50 / 1.89
B/R-12	3.71 / 12.23	1.43 / 3.30	1.15 / 11.37	2.3570 / 0.0015	-0.78 / -4.36	0.67 / 0.78	-22.92 / -23.51	1.23 / 2.24
B/R-13	3.65 / 11.72	0.95 / 3.02	1.02 / 11.06	3.5973 / 0.5288	-0.42 / -1.76	0.58 / 0.77	-22.42 / -23.32	0.90 / 2.55
B/R-14	3.24 / 10.66	1.94 / 2.56	1.27 / 11.99	3.7626 / 0.2000	-0.71 / -2.11	0.63 / 0.76	-23.32 / -23.25	0.91 / 2.09
B/R-15	3.19 / 9.80	1.55 / 2.53	1.49 / 21.56	4.0788 / 0	-0.58 / ---	0.58 / 0.77	-23.25 / -23.34	1.80 / 1.49
B/R-16	3.01 / 9.08	1.08 / 2.65	1.51 / 8.02	1.5833 / 0.1344	-0.83 / -2.29	0.64 / 0.78	-22.53 / -23.17	1.46 / 1.36
B/R-17	2.99 / 7.45	1.30 / 1.14	1.11 / 12.61	3.3859 / 0	-0.58 / ---	0.56 / 0.77	-22.94 / -22.35	0.85 / 0.90
B/R-18	2.99 / 5.66	1.05 / 2.17	1.09 / 6.61	5.8264 / 0	-0.26 / ---	0.53 / 0.80	-22.83 / -22.85	0.66 / 1.08
B/R-19	2.94 / 5.56	1.81 / 1.54	0.75 / 2.05	7.9209 / 1.1771	-0.36 / -1.12	0.56 / 0.70	-23.18 / -22.90	0.45 / 1.67
B/R-20	2.73 / 5.53	0.78 / 1.84	1.16 / 3.22	2.9106 / 0.2241	-0.43 / -1.91	0.58 / 0.74	-22.41 / -23.12	0.04 / 2.87
B/R-21	2.64 / 5.52	0.97 / 1.05	0.82 / 4.36	4.4156 / 0.2280	-0.34 / -1.66	0.55 / 0.74	-22.62 / -22.39	0.70 / 0.67
B/R-22	2.59 / 5.36	1.73 / 2.55	0.51 / 5.78	9.4646 / 0.4769	-0.26 / -1.73	0.51 / 0.76	-23.33 / -23.38	2.55 / 1.84
B/R-23	2.53 / 5.22	0.66 / 1.09	0.67 / 4.91	3.7511 / 0.2894	-0.25 / -1.57	0.50 / 0.75	-22.58 / -22.28	1.22 / 0.15
B/R-24	2.51 / 4.71	1.26 / 1.85	0.70 / 3.41	2.8558 / 0.0054	-0.65 / -3.53	0.59 / 0.77	-22.80 / -23.03	1.00 / 1.16
B/R-25	2.46 / 4.13	0.74 / 0.93	0.49 / 5.69	4.2743 / 0	-0.24 / ---	0.50 / 0.78	-22.25 / -21.93	2.12 / 0.76
B/R-26	2.41 / 4.09	0.65 / 1.28	0.66 / 2.70	1.0882 / 0.0813	-0.77 / -2.20	0.60 / 0.77	-22.02 / -22.55	0.86 / 1.47
B/R-27	2.40 / 3.08	0.42 / 1.22	1.50 / 4.63	0.5720 / 0	-0.86 / ---	0.47 / 0.80	-21.88 / -22.20	0.07 / 0
B/R-28	2.38 / 2.89	1.43 / 1.18	0.67 / 1.18	4.9461 / 0.7463	-0.46 / -1.20	0.55 / 0.73	-22.82 / -22.47	0.78 / 1.39
B/R-29	2.28 / 2.65	1.45 / 1.10	0.84 / 2.38	2.9813 / 0.0131	-0.69 / -2.92	0.63 / 0.78	-22.91 / -22.32	0.86 / 0.61
B/R-30	2.12 / 2.65	1.13 / 1.34	0.72 / 1.89	7.5327 / 0.7895	-0.18 / -1.23	0.48 / 0.74	-22.98 / -22.61	0.80 / 1.36
B/R-31	2.04 / 2.29	0.65 / 0.67	0.49 / 3.55	8.5263 / 0	0.12 / ---	0.42 / 0.79	-22.74 / -21.55	0.33 / 0.19
B/R-32	2.03 / 2.23	0.59 / 0.73	0.88 / 1.81	3.0271 / 0.0984	-0.29 / -1.87	0.49 / 0.77	-22.15 / -21.81	1.54 / 1.35
B/R-33	1.92 / 2.12	0.97 / 1.41	1.08 / 3.51	5.5084 / 0	-0.25 / ---	0.48 / 0.79	-22.52 / -22.61	1.01 / 0.72
B/R-34	1.89 / 2.09	0.88 / 0.40	0.58 / 2.10	11.4449 / 0.3732	0.12 / -1.03	0.39 / 0.69	-22.86 / -21.34	1.84 / 1.64
B/R-35	1.74 / 1.97	0.80 / 0.84	0.76 / 0.99	1.7241 / 0.6094	-0.67 / -1.14	0.51 / 0.70	-22.38 / -22.10	0.91 / 0.72
B/R-36	1.72 / 1.93	0.66 / 0.52	0.37 / 1.08	4.7982 / 0.7674	-0.14 / -0.83	0.44 / 0.71	-22.32 / -21.67	-0.54 / 0.06
B/R-37	1.68 / 1.87	1.11 / 1.44	0.50 / 1.15	1.0564 / 1.3607	-1.02 / -1.03	0.62 / 0.67	-22.55 / -22.95	1.03 / 1.32
B/R-38	1.65 / 1.84	0.54 / 0.64	0.40 / 0.94	3.8845 / 0.1060	-0.14 / -1.78	0.46 / 0.78	-22.07 / -21.47	0.25 / 1.05
B/R-39	1.55 / 1.83	1.08 / 0.51	1.19 / 2.43	5.4434 / 0.1860	-0.30 / -1.43	0.54 / 0.75	-22.92 / -21.38	1.85 / 0.59
B/R-40	1.50 / 1.80	0.33 / 1.26	0.09 / 1.81	5.6719 / 0.2119	0.23 / -1.77	0.29 / 0.75	-22.11 / -22.83	0.91 / 1.60
B/R-41	1.48 / 1.68	0.49 / 0.28	0.27 / 0.80	8.0608 / 0.3356	0.22 / -0.93	0.39 / 0.65	-22.41 / -21.26	0.22 / 0.43
B/R-42	0.84 / 1.65	0.27 / 0.70	0.13 / 1.20	4.7164 / 0.1817	0.24 / -1.59	0.34 / 0.74	-21.94 / -21.76	0.76 / 0.25

**Table 3.** Basic structural parameters of the galaxy sample presented in Figure 20 (blue galaxies, B) and Figure 21 (red galaxies, R). The different columns list: virial mass (200 critical), stellar mass, SMBH mass, star formation rate, specific star formation rate, (g-r) color, r band magnitude, and local galaxy overdensity. Colours do not include the effects of dust. The local galaxy overdensity is the same density as used in Figure 16. Some of the red galaxies are quenched so strongly that they have no ongoing star formation, e.g., R-2 or R-3. The stellar component of the galaxies presented here is typically resolved with  $\sim 10^5$  stellar particles, and the DM halo with about  $\sim 10$  times more DM particles. Galaxies are ranked according to their virial mass.

present circular velocity curves for stars, gas, DM, and the total circular velocity as a function of radius.

Late-type spiral galaxies are characterised by nearly flat circular velocity curves without signs of a very significant bulge. The galaxies presented in Figure 22 all show a rapid rising and then nearly flat circular velocity curve with a total amplitude depending on the total enclosed mass of the galaxy. In all cases the contribution of the gas component is sub-dominant compared to the stellar and DM contribution. Similar results were found by Marinacci et al. (2014a) using zoom-in simulations of eight Milky Way-sized haloes from the Aquarius project (Springel et al. 2008) using the Illustris galaxy formation model. The largest gas contribution over

the sample is  $\sim 70 \text{ km s}^{-1}$ , however in most cases the maximum contribution from the gas component is around  $\sim 50 \text{ km s}^{-1}$ . The vertical lines in Figure 22 show our fiducial galaxy radius ( $r_{\star}$ ) corresponding to twice the stellar half-mass radius. The various panels of Figure 22 also demonstrate how the stellar circular velocity curve and the DM circular velocity curve add up to a very flat total circular velocity curve. The inner parts of the galaxy are clearly dominated by the stellar mass. Beyond  $r_{\star}$  the DM contribution to the circular velocity curve dominates for all galaxies over the stellar contribution. The circular velocity curves stay flat out to 50 kpc for all galaxies shown in Figure 22. We also include in each panel the same eight circular velocity curves for the Aquila haloes taken

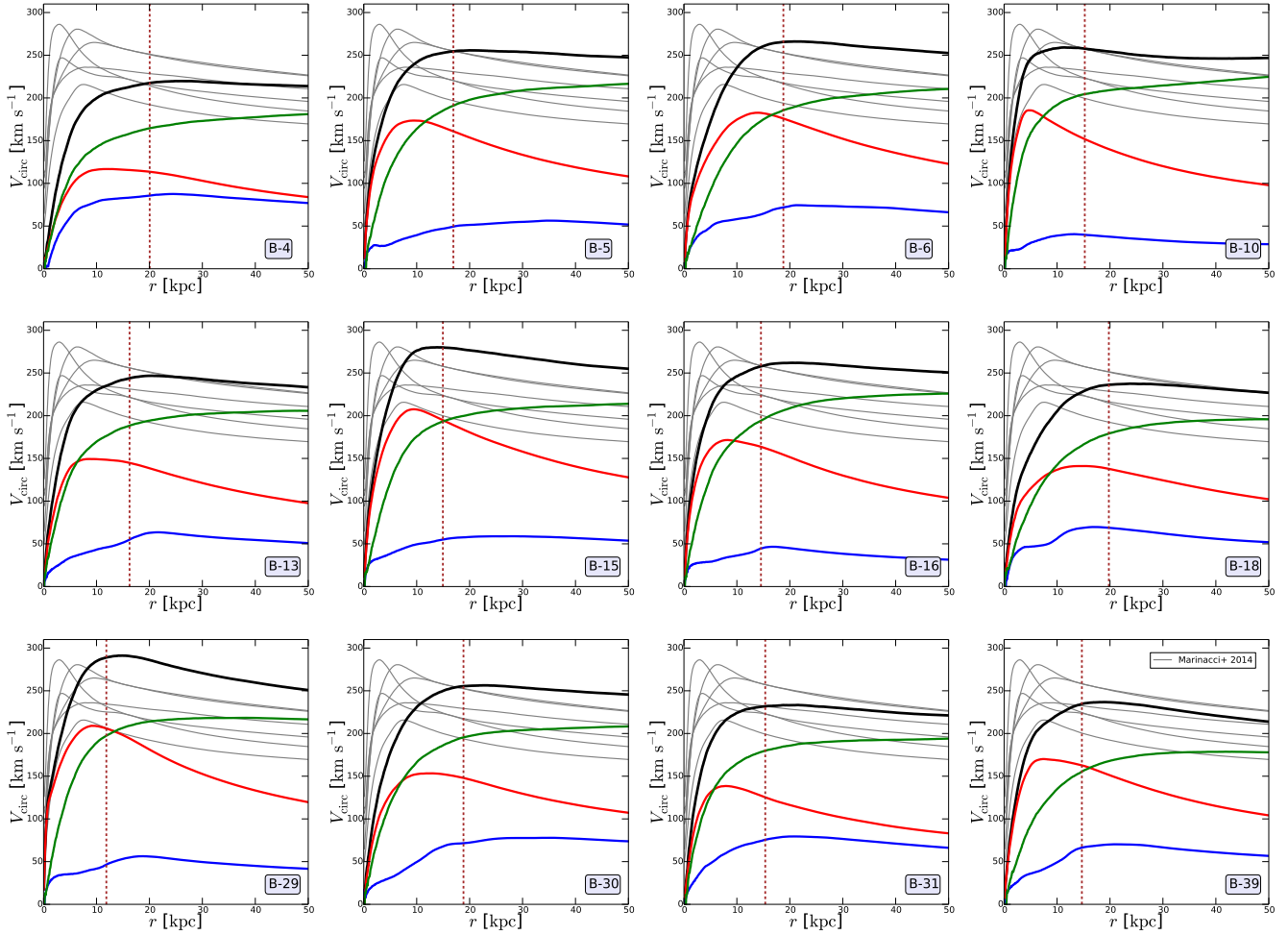


**Figure 22.** Circular velocity curves of a few selected disk galaxies from the sample presented in Figure 20. All of these galaxies show a steeply rising and then nearly flat circular velocity curve (black line), which is characteristic of late-type spiral galaxies. The different lines show the contributions from different mass components: gas (blue), stars (red), and DM (green). The gas contribution is typically small with maximum circular velocities around  $\sim 70 \text{ km s}^{-1}$  for some cases, and for most systems around  $\sim 50 \text{ km s}^{-1}$ . The dashed brown vertical lines shows our fiducial galaxy radius  $r_*$ , i.e. twice the stellar half-mass radius. This is the radius where we measure the circular velocity for the construction of the baryonic Tully-Fisher relation (see below). We also show in each panel the eight circular velocity curves for the Aquila haloes taken from Marinacci et al. (2014a) (gray thin lines). We note that those are based on the level-5 Aquarius haloes; i.e. sampled at higher spatial and mass resolution than the samples selected from the Illustris volume.

from Marinacci et al. (2014a) (gray thin lines). We note that our mass and spatial resolution is inferior to these simulations. However, Marinacci et al. (2014a) demonstrated that the circular velocity curves are reasonably well converged even if the mass resolution is changed by a factor of 64. Nevertheless, the initial rise and the exact location of the maximum of the circular velocity curve can still vary to some degree (see Marinacci et al. 2014a, for details). A study of the full galaxy population is provided in Genel et al. (in prep), where average circular velocity curves for the whole population, for a wide range of masses, and several redshifts are presented. There we also study the impact of baryons on the maximum circular velocity.

Disk galaxies are observationally found to follow the Tully-Fisher relation (TFR) (Tully & Fisher 1977) relating stellar luminosities (masses) to internal kinematics via the circular velocities. It has been shown that this relation becomes even tighter when the circular velocities are correlated with the total baryonic mass instead of the luminosities or stellar masses, leading to a very tight baryonic TFR (BTFR) (McGaugh 2012). We note that the BTFR is a strong

prediction of Modified Newtonian Dynamics (MoND) (Milgrom 1983) as an alternative of CDM. We present the BTFR of the 42 disk like galaxies of Figure 20 in the left panel of Figure 23 along with recent observations including  $1\sigma$  uncertainty bands (Avila-Reese et al. 2008; Hall et al. 2012; McGaugh 2012). We measure the total baryonic mass within  $r_*$ , and for the circular velocity we take the total mass within that radius and calculate the associated circular velocity (see also Scannapieco et al. 2012). The  $r_*$  radii are shown as dashed brown lines in the circular velocity curves of Figure 22, demonstrating that this radius lies already within the flat regime of the circular velocity curve. Our results for the TFR are therefore not very sensitive to this choice.

The BTFR of the disk galaxies in our simulation (represented here by this small sample) agrees well with the overall observational constraints, demonstrating that the internal structure of the stellar disks are characterised reasonably well, and that CDM models can reproduce the observed BTFR. Interestingly, our model predicts a BTFR which is closer to the tightest observational constraints (McGaugh 2012) than recent state-of-the-art zoom-in sim-

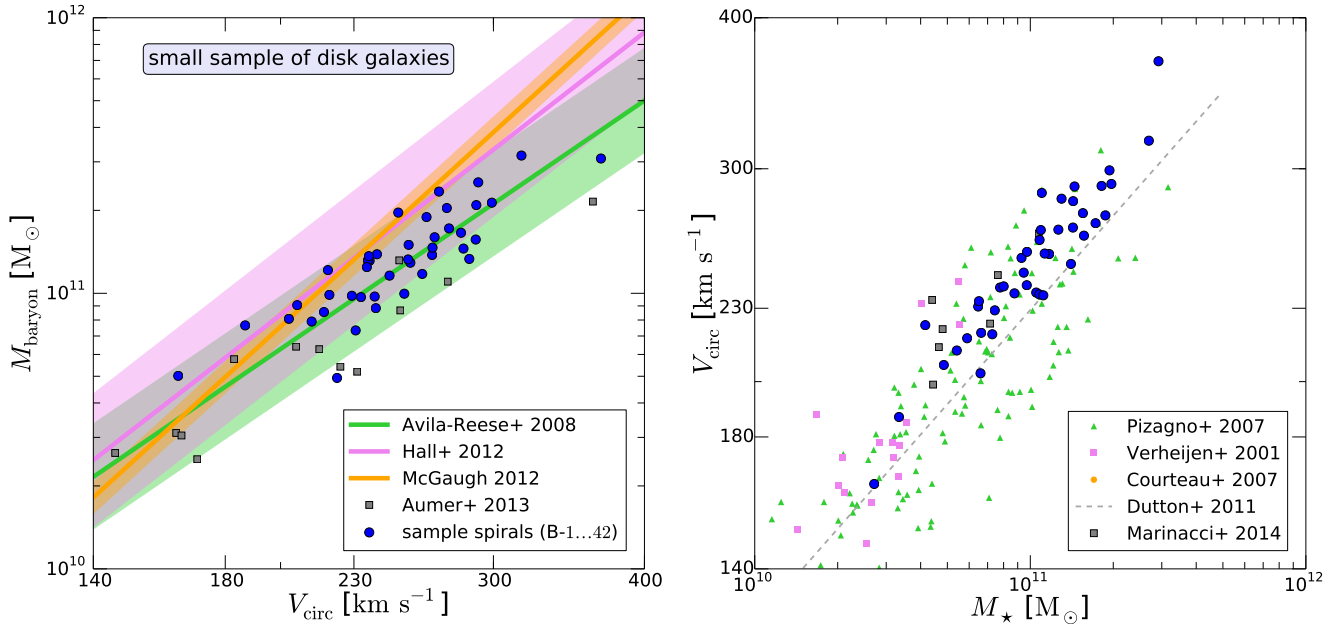


**Figure 23.** Tully-Fisher relations. Left panel: Baryonic Tully-Fisher relation for the 42 disk galaxies shown in Figure 20. We compare to observational mean trends (solid lines) with  $1\sigma$  scatter bands (Avila-Reese et al. 2008; Hall et al. 2012; McGaugh 2012). We note that this is only a small sub-sample of well-resolved simulated disk galaxies. Our simulation contains, for example, 4, 177 Milky Way halo analogs with virial masses in the range  $10^{11.5-12.5} M_{\odot}$  which are resolved similarly well as the galaxies presented here. We also include simulation points from a recent sample of high-resolution zoom-in simulations from Aumer et al. (2013). Right panel: Stellar Tully-Fisher relation for the same sample compared to observations (Verheijen 2001; Pizagno et al. 2007; Courteau et al. 2007; Dutton et al. 2011). We also show the theoretical predictions of Marinacci et al. (2014a) for the Aquila haloes.

ulations (Aumer et al. 2013) although our numerical resolution for these galaxies is significantly below the resolution of the zoom-in results. The very tight and steep BTFR is observed for a gas-rich galaxy sample, which is expected to give a more accurate measure of the slope and the normalisation of the BTFR than obtained from star-dominated spiral galaxies. Although our simulation results agree with the predicted scatter of Avila-Reese et al. (2008); Hall et al. (2012) the spread of our BTFR is still much larger than the results of McGaugh (2012). Also the slope is not as steep as predicted by that study. We note that a more detailed exploration of the BTFR has to take into account the full sample of well-resolved spiral galaxies, and also take into account the actual rotation velocities.

The right panel of Figure 23 shows the stellar TFR for the same selected disk galaxy sample compared to different observations (Verheijen 2001; Pizagno et al. 2007; Courteau et al. 2007; Dutton et al. 2011); i.e. we plot the same velocity as in the left panel now as a function of stellar mass instead of total baryonic mass. We also show the theoretical predictions of Marinacci et al. (2014a) for the Aquila haloes. Our galaxies follow a similar trend as the high-resolution Aquila haloes: we recover the correct slope and amount of scatter in the relation. However, it seems that our results indicate slightly too high circular velocities. This is also true for the Aquila galaxies of Marinacci et al. (2014a).

The blue and red galaxy samples discussed so far were selected “by eye” to be representative for distinct classes of galaxies. In the following we would like to characterise in more detail the morphological galaxy mix as a function of stellar mass. However, we are severely limited by our mass resolution to properly model and characterise galaxy types of systems that are only resolved by a few tens of thousands of stellar resolution elements. In fact, reliably

identifying the type of a galaxy requires substantially more particles, and we will not attempt to quantify the morphological type of galaxies for systems that are resolved with less than  $\sim 10^5$  stellar particles resulting in a lowest stellar mass of about  $\sim 10^{11} M_{\odot}$ . Automatically classifying galaxy types for less well-resolved objects is rather difficult and the obtained results are highly uncertain.

For the well-resolved objects with  $M_{\star} > 10^{11} M_{\odot}$  we will apply a kinematic bulge-to-disk decomposition. Specifically, we follow Abadi et al. (2003) and define for every star particle with specific angular momentum  $j_z$  around a selected  $z$ -axis a circularity parameter  $j_z/j(E)$ , where  $j(E)$  is the maximum specific angular momentum possible at the specific binding energy  $E$  of the star. We define a  $z$ -axis based on the star-forming gas, or the stars, if there is no star-forming gas in the system, which can occur in more massive and heavily quenched systems. Having the circularities of all stellar particles of the system we can then determine the fraction,  $f_{>0.7}$ , of particles with circularities above 0.7. These stars are typically classified as disk stars (see also Marinacci et al. 2014a). We then calculate the bulge-to-total ratio (B/T) as  $1 - f_{>0.7}$  for each galaxy. This gives for every galaxy a bulge-to-total ratio for the stellar component based on the circularities of the stars. Based on those values we can then split the distribution of galaxies into different types. Here we follow the cuts applied in Guo et al. (2011), where the morphological types of galaxies based on the Millennium-I and -II (MS-I, MS-II) simulations combined with a semi-analytic model were compared to observations from Conselice (2006). As described above we can probe the morphological types only for the most massive galaxies in our sample due to the resolution requirements, i.e. we can probe the types only over a much smaller range than Guo et al. (2011), for example.

We present our results in Figure 24, where we compare our



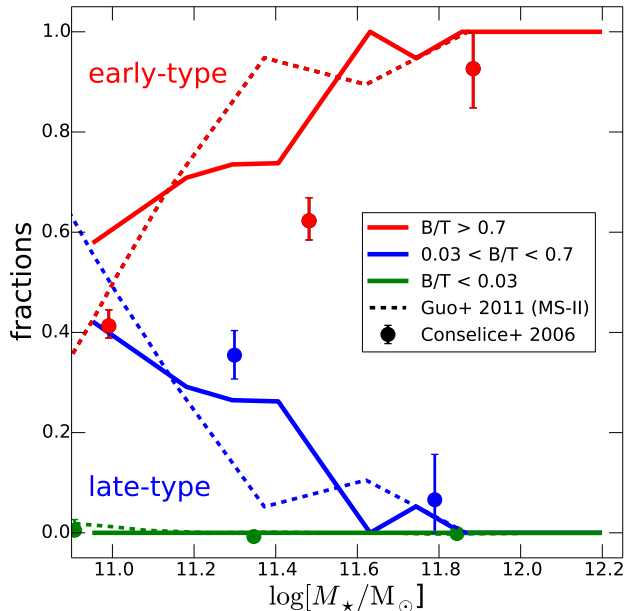


**Figure 24.** Distribution of galaxy types based on a kinematic classification using thresholds in bulge-to-disk (B/T) ratios. The red line represents bulge-dominated systems like early type galaxies. The blue line represents spiral galaxies with some bulge contribution, whereas the green line shows the fraction of pure-disk galaxies. We compare our results to observations from Conselice (2006). We also show the predictions of the semi-analytic model of Guo et al. (2011) based on the Millennium-II (MS-II) simulation. We can probe only massive systems due to resolution limitations. Objects with  $M_* \lesssim 10^{11} M_\odot$  contain fewer than  $10^5$  stellar particles which is insufficient for a reliable galaxy type classification. Despite the small mass range covered, we find that the simulation correctly describes the transition from the bulge-dominated regime for more massive systems to the disk-dominated regime for lower mass galaxies. We employ the same B/T cut as Guo et al. (2011) and find that the ‘crossing point’ of the galaxy types is predicted to be at nearly the same mass within the two galaxy formation models.

findings to the observations of Conselice (2006) and to the predictions of the semi-analytic model of Guo et al. (2011) (based on the MS-II). Although Figure 24 only probes the most massive systems in our simulations, we find that we recover the observed trends for the mass dependence of the different galaxy types. Most importantly, we find the correct transitional behaviour from more disk-like systems at lower masses to bulge-dominated systems towards larger stellar masses. Over this mass range we find a similar level of agreement with the observations as the predictions of Guo et al. (2011). However, this should not be over-interpreted since the comparison to observations is not unique due to the different techniques that were applied to extract the morphological types in the observations and the simulations. Our cuts are identical to those applied in Guo et al. (2011), and it is therefore interesting that we find a similar ‘crossing-mass’ of about  $M_* \sim 10^{11} M_\odot$  as the semi-analytic prediction.

As a final point of comparison between our model and an observable of the local Universe, we also investigate the age of the stellar populations in galaxies. This quantity can be inferred observationally and can therefore be used to test our model. Simply speaking, SF in galaxies is either biased towards earlier or later periods of structure formation, depending on the galaxy type: early-

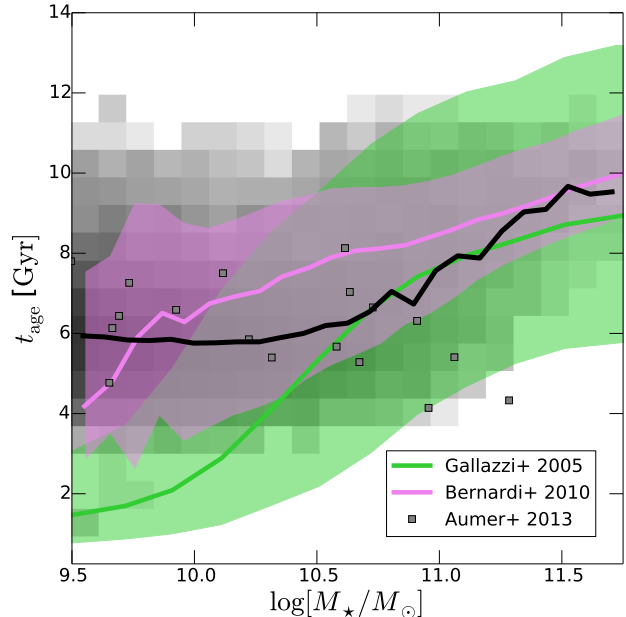


**Figure 25.** Stellar age as a function of stellar mass. The black line shows the simulation median, and the background histogram all simulated galaxies. Colored lines show two observational samples: one covering a large fraction of SDSS galaxies (Gallazzi et al. 2005), and one showing a subsample of early-type galaxies (Bernardi et al. 2010). We also include the simulation results from Aumer et al. (2013). Our model predicts the mean ages of galaxies correctly for systems more massive than  $\sim 10^{10.5} M_\odot$ . However, low mass systems tend to be too old compared to the full observational sample. They seem to agree better with the early-type subset. This problem of low mass galaxies being too old is shared with the model of Aumer et al. (2013), which predicts even older galaxies around  $M_* \sim 10^{10} M_\odot$ .

type galaxies form most of their stellar content early, whereas late-type galaxies show more late SF activity. This ‘downsizing’ effect, which is ultimately caused by baryonic processes like feedback, works therefore contrary to the hierarchical bottom-up build-up of CDM, where larger systems like clusters assemble later. We can inspect downsizing in our model by plotting the mass-weighted stellar age of simulated galaxies against their stellar mass, as shown in Figure 25. We compare here to two observational datasets: one derived from a large SDSS sample (Gallazzi et al. 2005), and a second one based on a SDSS subset biased towards early-type galaxies (Bernardi et al. 2010). We find reasonable agreement within the scatter and the total sample. Most importantly, we recover the correct trend of age downsizing. However, low-mass systems ( $M_* \lesssim 10^{10.5} M_\odot$ ) tend to form their stars too early in our simulation; i.e. they are too old compared to observations. We stress that this tension is shared by semi-analytic models and other state-of-the-art hydrodynamical simulations alike, pointing towards an open problem in low-mass galaxy formation (Weinmann et al. 2012). It remains to be seen whether new more explicit feedback models can resolve this problem (Hopkins et al. 2013b).

## 6 SUMMARY

We have introduced the Illustris Project, a series of large-scale hydrodynamical and DM-only simulations of galaxy formation. The highest resolution simulation, Illustris-1, covers a volume of

(106.5 Mpc)<sup>3</sup>, has a dark mass resolution of  $6.26 \times 10^6 M_\odot$ , and an initial baryonic matter mass resolution of  $1.26 \times 10^6 M_\odot$ . At  $z = 0$  gravitational forces are softened on scales of 710 pc, and the smallest hydrodynamical gas cells have a fiducial radius of 48 pc. The simulation follows the evolution of  $2 \times 1820^3$  resolution elements and additionally evolves  $1820^3$  passive Monte Carlo tracer particles reaching a total particle count of more than 18 billion. The free parameters of our model are set to physically plausible values and have been constrained based on the star formation efficiency using smaller scale simulations (Vogelsberger et al. 2013) and with minor modifications in high-resolution zoom-in simulations of individual Milky Way-like haloes (Marinacci et al. 2014a,b). They were also used in recent magneto-hydrodynamical simulations of Milky Way-like haloes (Pakmor et al. 2014).

In this first paper and a companion paper Vogelsberger et al. (2014b), we have presented initial results focusing on the galaxy population at  $z = 0$ . High redshift results are presented in Genel et al. (in prep). We will summarise in the following our main results.

**Impact of baryons on the halo mass function:** We find that galaxy formation physics affects the halo mass function at low and high halo masses, leading to a reduction of the overall abundance by up to  $\sim 30\%$  at both ends. In these mass ranges baryonic feedback processes are strongest. For intermediate mass haloes we find deviations below  $\lesssim 10\%$ . Our radio-mode implementation leads to a significant reduction in halo mass also towards higher masses, which is different from previous findings (e.g. Sawala et al. 2013), which do not include AGN feedback. We note, however, that other implementations of radio-mode feedback may yield a different outcome at higher halo masses.

**Impact of baryons on halo masses:** Related to the change in the mass function we also find that individual halo masses are significantly affected by baryonic physics: haloes less or more massive than  $\sim 10^{11} M_\odot$  have up to  $\sim 20 - 30\%$  less mass in Illustris-1 compared to matched haloes in the corresponding DM-only simulation. These trends differ from most previous results, where the strongest impact of baryonic physics was found towards lower halo masses (e.g., Sawala et al. 2013). However, our energetic AGN feedback also causes halo masses to differ substantially in more massive systems. Intermediate mass haloes around  $\sim 10^{11} M_\odot$  tend to be more massive in the hydrodynamical simulation by about  $\sim 10\%$ .

**Cosmic star formation rate density:** By construction, the build-up of stellar mass predicted by our galaxy formation model agrees well with observations. We have tested our results against recent measurements of the cosmic star formation rate density. We find good agreement with observations up to  $z \sim 10$ , although our model predicts slightly too much present-day star formation which is dominated by galaxies with stellar masses about  $M_\star \sim 10^{10-10.5} M_\odot$ . At high redshifts we find good agreement of our model with recent lower limits of the cosmic star formation rate densities. Beyond  $z \sim 8$  our model agrees best with the shallowest slope ( $-10.9 + 2.5$ ) of recent best-fit slopes for combined  $z \geq 8$  measurements ( $\propto (1+z)^{-10.9 \pm 2.5}$ ) by Oesch et al. (2013).

**Galaxy stellar mass and luminosity functions:** The present-day abundance of galaxies both as a function of stellar mass and stellar luminosity agrees well with observations of the local Universe as indicated by a comparison with SDSS based observations. We stress that for both quantities there are significant observational

measurement uncertainties in the stellar light assignment at the bright and massive end (see Bernardi et al. 2013) that we take into account by providing two stellar light and mass estimates. We find reasonable agreement of our simulation with observations over a substantial mass ( $M_\star \sim 10^9 - 10^{12.5} M_\odot$ ) and luminosity range ( $M_r \sim -15.0 - -24.5$ ). We also find good agreement with the stellar mass function of star-forming galaxies, and reproduce the measured fraction of “red and dead” galaxies at the massive end: for  $M_\star > 10^9 M_\odot$  we find that about 52% of all stellar mass at  $z = 0$  is in galaxies with a low SF rate, which agrees reasonably well with observations of Moustakas et al. (2013),

**Baryon conversion efficiency:** We have compared the baryon conversion efficiency of our model to recent abundance matching results, where we recover the inferred observation results within the  $1\sigma$  uncertainties. Baryon conversion is most efficient around halo masses  $M_{200,\text{crit}} \sim 10^{12} M_\odot$ , and drops quickly for lower and higher mass systems due to SN and AGN feedback. Our model predicts a maximum efficiency of about  $\sim 20\%$  at halo masses slightly above  $10^{12} M_\odot$  in reasonable agreement with the findings of abundance matching techniques, although the results of Behroozi et al. (2013a) peak at higher masses than those of Moster et al. (2013). The exact amplitude and location of the peak predicted by our model also depends on the exact definition of stellar mass: considering the total stellar mass of the halo, excluding satellites, peaks at a slightly higher mass than the efficiency based on the galactic stellar mass only. However, this uncertainty is smaller than the differences between different abundance matching results. We stress that the interplay of SN and AGN feedback is crucial to reproduce this result and especially the shape of the stellar mass to halo mass relation.

**Colours of galaxies:** In this first paper we have studied only intrinsic g-r and u-i colours of galaxies neglecting the important effect of dust. Given this caveat, we find a bimodal colour distribution which has a significantly less pronounced maximum at red colours compared to observations. The most massive galaxies with  $M_\star \sim 10^{12} M_\odot$  peak around u - i  $\sim 2.8$ . The  $M_\star = 10^{10.5} M_\odot$  to  $M_\star = 10^{11.0} M_\odot$  mass range shows a clear bimodal distribution with broad maxima at u - i  $\sim 1.5$  and u - i  $\sim 2.75$ . Lower mass systems around  $M_\star \sim 10^{10} M_\odot$  show a broad maximum at u - i  $\sim 1.4$ . Our low and high mass results agree reasonably well with observations and predictions from the recent semi-analytic models of Guo et al. (2011). However, we do not match the colours of intermediate mass systems. A more detailed study taking into account the effects of dust is required to understand this discrepancy better. We divide the galaxy population also into central and satellite galaxies finding that for all galaxies above  $M_\star \sim 10^9 M_\odot$  the red part of the g-r and u-i distribution is dominated by satellites. For galaxies more massive than  $M_\star \sim 10^{11} M_\odot$  we find however that centrals dominate the red maximum of the distribution in both colours. We have also inspected the red fraction of galaxies as a function of stellar mass, specific star formation rate, and BH mass. The most rapid transition from blue galaxies to red galaxies can be found as a function of specific star formation rate, where our model predicts a sharp transition from blue to red around  $10^{-2} \text{Gyr}^{-1}$ . The transition as a function of BH mass and stellar mass is significantly broader.

**The impact of environment on the galaxy population and mass and environment quenching:** We have studied galaxy colours (g-r) and red fractions as a function of stellar mass ( $M_\star$ ) and galaxy overdensity ( $1 + \delta$ ), where  $\delta$  was constructed based on the dis-



tance to the fifth nearest neighbouring galaxy with an r band magnitude brighter than  $-19.5$ . We recover qualitatively the observational trends of mass and environment quenching. Specifically, we recover the observational trends of Peng et al. (2010) when plotting the red fraction as a function of mass and galaxy overdensity. Interestingly, we also reproduce the drop in the red fraction around  $M_* \sim 10^{10} M_\odot$  for high galaxy overdensities  $1 + \delta \gtrsim 10^2$ , where a slightly shifted 0.9 red fraction contour line agrees remarkably well with our simulation predictions. We demonstrate that this high density drop in the red fraction is less pronounced once the environment is characterised with an estimator that is less contaminated by a remaining halo mass dependence ( $D_{1,1}$  taken from Haas et al. (2012) indicating that  $\delta$  is not ideal in probing environmental effects alone (see also the discussion in Haas et al. 2012)). Our model also reproduces the observed environment independence of star formation rates for star-forming galaxies in agreement with the findings of Peng et al. (2010). This demonstrates that high density environments increase the probability of galaxies being quenched, but does not directly affect the star formation rates of non-quenched, star-forming, galaxies.

**Morphology of galaxies:** The numerical resolution of Illustris is sufficient to study the internal structure of relatively more massive galaxies ( $M_* \gtrsim 10^{11}$ ), which are resolved with more than  $\sim 10^5$  stellar resolution elements. We have constructed small samples of red and blue galaxies (R-1 to R-42 and B-1 to B-42) which are well-resolved and representative of our galaxy population. A visual classification of these galaxies reveals that our model clearly yields a significant population of star-forming blue disk-like galaxies co-existing with quenched red elliptical galaxies. We have extended this classification to all galaxies with  $M_* \gtrsim 10^{11} M_\odot$  using a kinematic bulge-disk decomposition. We find that our simulation correctly describes the transition from late type galaxies to early types as a function of stellar mass. We have compared the relative fractions in both populations with the observational sample from Conselice (2006) and the semi-analytic prediction of Guo et al. (2011) finding good agreement among the three. Interestingly, our model predicts the same transition mass  $M_* \sim 10^{11} M_\odot$ , the mass where the fraction of early- and late-types both equals 50%, as the recent semi-analytic model of Guo et al. (2011) using very similar cuts in the bulge-to-disk ratios for the galaxy type classification.

**Circular velocity curves and Tully-Fisher relation:** We have constructed circular velocity curves for a few selected late-type spiral galaxies with halo masses between  $\sim 10^{12} M_\odot$  and  $\sim 10^{13} M_\odot$ . All selected galaxies show steeply rising circular velocity curves which then become flat towards larger radii. The gas contribution to the circular velocity profiles is not significant and typically is at most  $\sim 50 \text{ km s}^{-1}$  and in rare cases  $\sim 70 \text{ km s}^{-1}$ . Our model reproduces the observed stellar and baryonic Tully-Fisher relation reasonably well. We have demonstrated this based on a small subset of spiral galaxies. As a function of stellar mass these galaxies tend to lie a few  $\text{km s}^{-1}$  above the observed trend. The slope and spread of the baryonic Tully-Fisher relations is reproduced when compared to the observations of Avila-Reese et al. (2008) and Hall et al. (2012). However, we do not reproduce the steep slope and small scatter of the relation found by McGaugh (2012). Nevertheless, the baryonic Tully-Fisher of our selected sample agrees slightly better with observations than the recent high resolution simulations of Aumer et al. (2013).

**Stellar ages:** Our galaxy formation model works well for most of the observational probes considered here. However, the stellar ages

of low mass galaxies are not predicted correctly. Specifically, we recover the correct trend of downsizing with respect to stellar ages, but low mass galaxies ( $M_* \lesssim 10^{10.5} M_\odot$ ) are a factor two to three too old compared to observational constraints, which point towards very young stellar populations for these masses. In our simulation, these systems tend to form their stars too early. The agreement at higher masses, where our galaxies are resolved better, is good. Although the failure at low stellar masses could be related to resolution effects, we doubt that this can fully explain the discrepancy.

**Summary:** In summary we find that the Illustris simulation is able to reproduce many of the observed trends in the local Universe reasonably well. There are still some discrepancies related to the stellar ages of low mass galaxies and the quenching of massive galaxies, which require further investigation. We also stress that it is not advisable to tune galaxy formation models such that they reproduce any observation exactly. For example, the systematic errors at the bright end of the galaxy stellar mass function (Bernardi et al. 2013) have to be considered when constructing a galaxy formation model. The same is true for reproducing the stellar to halo mass relationship, which is also uncertain towards higher masses (Kravtsov et al. 2014). Different abundance matching results differ also towards lower halo masses (see Moster et al. 2013; Behroozi et al. 2013a), and they might even break down towards dwarf-scale masses (Sawala et al. 2014). Such systematic uncertainties have to be considered when trying to match observational data with semi-analytic models or hydrodynamical simulations. Special care needs to be taken when invoking new physical mechanisms for feedback or star formation to accommodate certain aspects of observational data if systematic errors have to be considered. Reproducing observational data perfectly does not imply a correct and physically meaningful model.

## 7 CONCLUSION AND OUTLOOK

We have demonstrated in this study that state-of-the-art hydrodynamical simulations like Illustris are capable of reproducing a significant amount of observational data both on large and on small scales. Those simulations have now reached the mass and spatial resolution of recent large-scale DM only simulations. Although not every observed relation is reproduced precisely by our model, it seems that the most important aspects of galaxy formation may have been identified. A model universe like Illustris can now be used to refine our understanding of galaxy formation. The way to move forward is to identify remaining problems of the model, where the predictions severely disagree with observational data. One such prediction is the age distribution of low mass galaxies, which conflicts with observations. Furthermore, at the massive end we find that our AGN feedback is not efficient enough to lead to sufficient quenching of massive galaxies. Understanding these problems will lead to better insights into the relevant physics.

Besides comparing to observational data it is crucial that galaxy formation models also make distinct predictions that can be tested in the future to falsify certain aspects of the model. Our galaxy formation model, for example, also follows the build-up and distribution of metals as described above. Metals can be found in many different “baryonic phases” in the Universe. They are produced in stars and distributed into the CGM and IGM via SN driven winds. We can use our simulation to predict in which baryonic phase we expect metals to be found at various redshifts. A first coarse attempt of this is presented in Figure 26, where we distin-

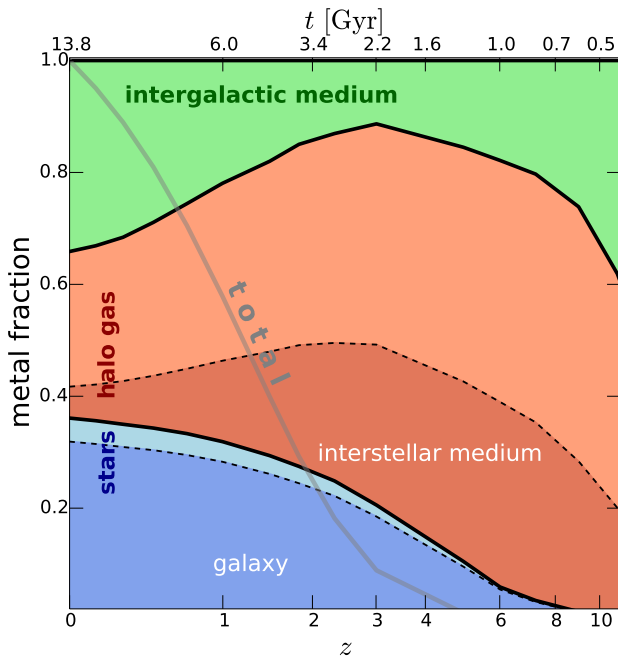


**Figure 26.** Fractional metal content in different baryonic phases as a function of time. We divide the gas in three main components: stars (stars bound to haloes), halo gas (gas bound to haloes), and unbound gas (intergalactic medium). Stars are further subdivided into stars belonging to the galaxy (within  $r_*$ ) and stars outside the galaxy. A similar division is made for the gas, where we divide between gas belonging to the interstellar medium, and other halo gas, which is gravitationally bound. The thick gray line shows the increase of the total metal content on the same linear scale normalised to unity at  $z = 0$ . Our simulation predicts “metal equipartition” at  $z \sim 0$  such that each baryon phase holds about one third of the total metal content in the Universe. At all other redshifts the situation is rather different, for example, at high redshifts halo gas largely dominates the metal budget.

guish three main baryonic phases: stars, gravitationally bound gas, and gas which is not bound to any halo. We further subdivide the stellar contribution into stars which belong to the galaxy ( $r < r_*$ ), and those which are part of the outer halo. We make an additional distinction for bound gas where we separate star-forming interstellar gas from non-star forming gas. Cold and dense gas forms stars, which subsequently synthesise metals. This explains why the contribution of metals in stars is increasing and the relative contribution in the gas phase is decreasing. SN driven winds enrich the intergalactic medium, leading to more metals in this diffuse phase at later times. Interestingly, our simulation predicts a kind of “metal equipartition” at  $z \sim 0$  such that each baryonic phase holds about one third of the total metal content in the Universe. At all other redshifts the situation is rather different, for example, at high redshifts halo gas largely dominates the metal budget. Our simulation provides therefore detailed predictions of the evolving metal abundances in all baryonic phases that can potentially be probed through upcoming observations allowing us to understand better the complicated “baryon cycle” of galaxies. It remains to be seen how well these predictions can be tested in the future and what physical insight can be extracted through even more detailed comparisons between simulations and observations.

## 8 DATA RELEASE AND ACCESS

The Illustris simulation data in the form of various group catalogues, merger trees (subhalo-, halo-, and galaxy-based), light-cone mock observations, pre-processed snapshot data in HDF5 format allowing access to every stored quantity at all redshifts, galaxy images, galaxy spectra and broad-band magnitudes, etc. will be made available in the near future. Data distribution will be handled through <http://www.illustris-project.org>. There we also provide additional visual material in the form of movies and images. The website also hosts a simulation explorer interface with query functionality to browse the simulation data interactively. This explorer provides 17.2 gigapixel images of the gas distribution (density, temperature, metallicity, etc.), stellar density, dark matter density, and SZ- and X-ray maps. It can be used interactively to query the group catalogues, merger trees, galaxy images, SMBH data etc. Galaxy images from an image post-processing pipeline (Torrey et al., in prep) are also available, resulting in galaxy image and spectral databases with a total data volume of about 1 petabyte in its final installation.

## ACKNOWLEDGEMENTS

MV thanks Qi Guo and Federico Marinacci for providing data. VS acknowledges support by the DFG Research Centre SFB-881 “The Milky Way System” through project A1, and by the European Research Council under ERC-StG EXAGAL-308037. GS acknowledges support from the HST grants program, number HST-AR-12856.01-A. Support for program #12856 (PI J. Lotz) was provided by NASA through a grant from the Space Telescope Science Institute, which is operated by the Association of Universities for Research in Astronomy, Inc., under NASA contract NAS 5-26555. LH acknowledges support from NASA grant NNX12AC67G and NSF grant AST-1312095. DX acknowledges support from the Alexander von Humboldt Foundation. Simulations were run on the Harvard Odyssey and CfA/ITC clusters, the Ranger and Stampede supercomputers at the Texas Advanced Computing Center as part of XSEDE, the Kraken supercomputer at Oak Ridge National Laboratory as part of XSEDE, the CURIE supercomputer at CEA/France as part of PRACE project RA0844, and the SuperMUC computer at the Leibniz Computing Centre, Germany, as part of project pr85je.

## REFERENCES

- Abadi, M. G., Navarro, J. F., Steinmetz, M., & Eke, V. R. 2003, *Astrophys. J.*, 597, 21
- Abel, T., & Wandelt, B. D. 2002, *MNRAS*, 330, L53
- Agertz, O., Teyssier, R., & Moore, B. 2011, *MNRAS*, 410, 1391
- Angulo, R. E., Springel, V., White, S. D. M., et al. 2012, *MNRAS*, 426, 2046
- Ascasibar, Y., Yepes, G., Gottlöber, S., & Müller, V. 2002, *A&A*, 387, 396
- Aumer, M., White, S. D. M., Naab, T., & Scannapieco, C. 2013, *MNRAS*, 434, 3142
- Avila-Reese, V., Zavala, J., Firmani, C., & Hernández-Toledo, H. M. 2008, *Astron. J.*, 136, 1340
- Baldry, I. K., Balogh, M. L., Bower, R. G., et al. 2006, *MNRAS*, 373, 469
- Baldry, I. K., Glazebrook, K., Brinkmann, J., et al. 2004, *Astrophys. J.*, 600, 681

- Baldry, I. K., Driver, S. P., Loveday, J., et al. 2012, *MNRAS*, 421, 621
- Barnes, J., & Hut, P. 1986, *Nature*, 324, 446
- Behroozi, P. S., Wechsler, R. H., & Conroy, C. 2013a, *Astrophys. J.*, 770, 57
- Behroozi, P. S., Wechsler, R. H., & Wu, H.-Y. 2013b, *Astrophys. J.*, 762, 109
- Bell, E. F., McIntosh, D. H., Katz, N., & Weinberg, M. D. 2003, *Astrophys. J. Suppl.*, 149, 289
- Bernardi, M., Meert, A., Sheth, R. K., et al. 2013, *MNRAS*, 436, 697
- Bernardi, M., Shankar, F., Hyde, J. B., et al. 2010, *MNRAS*, 404, 2087
- Blanton, M. R., Eisenstein, D., Hogg, D. W., Schlegel, D. J., & Brinkmann, J. 2005a, *Astrophys. J.*, 629, 143
- Blanton, M. R., Lupton, R. H., Schlegel, D. J., et al. 2005b, *Astrophys. J.*, 631, 208
- Bond, J. R., Kofman, L., & Pogosyan, D. 1996, *Nature*, 380, 603
- Booth, C. M., & Schaye, J. 2009, *MNRAS*, 398, 53
- Bower, R. G., Benson, A. J., Malbon, R., et al. 2006, *MNRAS*, 370, 645
- Boylan-Kolchin, M., Springel, V., White, S. D. M., Jenkins, A., & Lemson, G. 2009, *MNRAS*, 398, 1150
- Brook, C. B., Kawata, D., Gibson, B. K., & Flynn, C. 2004, *MNRAS*, 349, 52
- Brook, C. B., Stinson, G., Gibson, B. K., Wadsley, J., & Quinn, T. 2012, *MNRAS*, 424, 1275
- Bruzual, G., & Charlot, S. 2003, *MNRAS*, 344, 1000
- Bryan, G. L., & Norman, M. L. 1998, *Astrophys. J.*, 495, 80
- Cantalupo, S., & Porciani, C. 2011, *MNRAS*, 411, 1678
- Chabrier, G. 2003, *Pub. Astron. Soc. Pac.*, 115, 763
- Coil, A. L., Blanton, M. R., Burles, S. M., et al. 2011, *Astrophys. J.*, 741, 8
- Cole, S., Lacey, C. G., Baugh, C. M., & Frenk, C. S. 2000, *MNRAS*, 319, 168
- Colless, M., Dalton, G., Maddox, S., et al. 2001, *MNRAS*, 328, 1039
- Collins, D. C., Xu, H., Norman, M. L., Li, H., & Li, S. 2010, *Astrophys. J. Suppl.*, 186, 308
- Conselice, C. J. 2006, *MNRAS*, 373, 1389
- Cool, R. J., Moustakas, J., Blanton, M. R., et al. 2013, *Astrophys. J.*, 767, 118
- Courteau, S., Dutton, A. A., van den Bosch, F. C., et al. 2007, *Astrophys. J.*, 671, 203
- Crain, R. A., Theuns, T., Dalla Vecchia, C., et al. 2009, *MNRAS*, 399, 1773
- Croton, D. J., Springel, V., White, S. D. M., et al. 2006, *MNRAS*, 365, 11
- Cui, W., Borgani, S., Dolag, K., Murante, G., & Tornatore, L. 2012, *MNRAS*, 423, 2279
- Dalla Vecchia, C., & Schaye, J. 2008, *MNRAS*, 387, 1431
- . 2012, *MNRAS*, 426, 140
- Davé, R., Oppenheimer, B. D., & Finlator, K. 2011, *MNRAS*, 415, 11
- Davé, R., Cen, R., Ostriker, J. P., et al. 2001, *Astrophys. J.*, 552, 473
- Davis, M., Efstathiou, G., Frenk, C. S., & White, S. D. M. 1985, *Astrophys. J.*, 292, 371
- Davis, M., Faber, S. M., Newman, J., et al. 2003, in *Society of Photo-Optical Instrumentation Engineers (SPIE) Conference Series*, Vol. 4834, Discoveries and Research Prospects from 6- to 10-Meter-Class Telescopes II, ed. P. Guhathakurta, 161–172
- Debuhr, J., Quataert, E., & Ma, C.-P. 2011, *MNRAS*, 412, 1341
- Dekel, A., & Silk, J. 1986, *Astrophys. J.*, 303, 39
- Di Matteo, T., Colberg, J., Springel, V., Hernquist, L., & Sijacki, D. 2008, *Astrophys. J.*, 676, 33
- Di Matteo, T., Springel, V., & Hernquist, L. 2005, *Nature*, 433, 604
- Dolag, K., Borgani, S., Murante, G., & Springel, V. 2009, *MNRAS*, 399, 497
- Dolag, K., Jubelgas, M., Springel, V., Borgani, S., & Rasia, E. 2004, *Astrophys. J. Let.*, 606, L97
- Dubois, Y., Devriendt, J., Slyz, A., & Teyssier, R. 2012, *MNRAS*, 420, 2662
- Dubois, Y., & Teyssier, R. 2008, *A&A*, 477, 79
- Dubois, Y., Pichon, C., Welker, C., et al. 2014, arXiv:1402.1165
- Dutton, A. A., van den Bosch, F. C., Faber, S. M., et al. 2011, *MNRAS*, 410, 1660
- Elbaz, D., Daddi, E., Le Borgne, D., et al. 2007, *A&A*, 468, 33
- Ellis, R. S., McLure, R. J., Dunlop, J. S., et al. 2013, *Astrophys. J. Let.*, 763, L7
- Faucher-Giguère, C.-A., Lidz, A., Hernquist, L., & Zaldarriaga, M. 2008a, *Astrophys. J.*, 688, 85
- Faucher-Giguère, C.-A., Lidz, A., Zaldarriaga, M., & Hernquist, L. 2009, *Astrophys. J.*, 703, 1416
- Faucher-Giguère, C.-A., Prochaska, J. X., Lidz, A., Hernquist, L., & Zaldarriaga, M. 2008b, *Astrophys. J.*, 681, 831
- Ferland, G. J., Korista, K. T., Verner, D. A., et al. 1998, *Pub. Astron. Soc. Pac.*, 110, 761
- Few, C. G., Courty, S., Gibson, B. K., et al. 2012, *MNRAS*, 424, L11
- Gallazzi, A., Charlot, S., Brinchmann, J., White, S. D. M., & Tremonti, C. A. 2005, *MNRAS*, 362, 41
- Genel, S., Vogelsberger, M., Nelson, D., et al. 2013, *MNRAS*, 435, 1426
- Gerritsen, J. P. E., & Icke, V. 1997, *A&A*, 325, 972
- Giavalisco, M., Ferguson, H. C., Koekemoer, A. M., et al. 2004, *Astrophys. J. Let.*, 600, L93
- Gnedin, N. Y., & Hollon, N. 2012, *Astrophys. J. Suppl.*, 202, 13
- Governato, F., Brook, C., Mayer, L., et al. 2010, *Nature*, 463, 203
- Grogin, N. A., Kocevski, D. D., Faber, S. M., et al. 2011, *Astrophys. J. Suppl.*, 197, 35
- Guedes, J., Callegari, S., Madau, P., & Mayer, L. 2011, *Astrophys. J.*, 742, 76
- Guo, Q., White, S., Boylan-Kolchin, M., et al. 2011, *MNRAS*, 413, 101
- Haas, M. R., Schaye, J., & Jeason-Daniel, A. 2012, *MNRAS*, 419, 2133
- Hall, M., Courteau, S., Dutton, A. A., McDonald, M., & Zhu, Y. 2012, *MNRAS*, 425, 2741
- Hill, D. T., Kelvin, L. S., Driver, S. P., et al. 2011, *MNRAS*, 412, 765
- Hinshaw, G., Larson, D., Komatsu, E., et al. 2013, *Astrophys. J. Suppl.*, 208, 19
- Hogg, D. W., Blanton, M. R., Eisenstein, D. J., et al. 2003, *Astrophys. J. Let.*, 585, L5
- Hopkins, P. F., Keres, D., Onorbe, J., et al. 2013a, arXiv:1311.2073
- . 2013b, ArXiv e-prints
- Jenkins, A., Frenk, C. S., White, S. D. M., et al. 2001, *MNRAS*, 321, 372
- Jubelgas, M., Springel, V., & Dolag, K. 2004, *MNRAS*, 351, 423
- Jubelgas, M., Springel, V., EnBlin, T., & Pfrommer, C. 2008, *A&A*, 481, 33

- Kannan, R., Stinson, G. S., Macciò, A. V., et al. 2013, ArXiv e-prints, 1302.2618
- Katz, N. 1992, *Astrophys. J.*, 391, 502
- Katz, N., Hernquist, L., & Weinberg, D. H. 1992, *Astrophys. J. Let.*, 399, L109
- Katz, N., Weinberg, D. H., & Hernquist, L. 1996, *Astrophys. J. Suppl.*, 105, 19
- Kauffmann, G., White, S. D. M., & Guiderdoni, B. 1993, *MNRAS*, 264, 201
- Kauffmann, G., White, S. D. M., Heckman, T. M., et al. 2004, *MNRAS*, 353, 713
- Kawata, D., & Gibson, B. K. 2003, *MNRAS*, 340, 908
- . 2005, *MNRAS*, 358, L16
- Kay, S. T., Pearce, F. R., Frenk, C. S., & Jenkins, A. 2002, *MNRAS*, 330, 113
- Kennicutt, Jr., R. C. 1989, *Astrophys. J.*, 344, 685
- Kereš, D., Vogelsberger, M., Sijacki, D., Springel, V., & Hernquist, L. 2012, *MNRAS*, 425, 2027
- Khandai, N., Di Matteo, T., Croft, R., et al. 2014, arXiv:1402.0888
- Kim, J.-h., Abel, T., Agertz, O., et al. 2014, *Astrophys. J. Suppl.*, 210, 14
- Kimble, R. A., MacKenty, J. W., O’Connell, R. W., & Townsend, J. A. 2008, in *Society of Photo-Optical Instrumentation Engineers (SPIE) Conference Series*, Vol. 7010, *Society of Photo-Optical Instrumentation Engineers (SPIE) Conference Series*
- Klypin, A. A., Trujillo-Gomez, S., & Primack, J. 2011, *Astrophys. J.*, 740, 102
- Kobayashi, C. 2004, *MNRAS*, 347, 740
- Koekemoer, A. M., Faber, S. M., Ferguson, H. C., et al. 2011, *Astrophys. J. Suppl.*, 197, 36
- Kosowsky, A. 2003, *NewAR*, 47, 939
- Kravtsov, A., Vikhlinin, A., & Meshcheryakov, A. 2014, arXiv:1401.7329
- Kurosawa, R., & Proga, D. 2009, *MNRAS*, 397, 1791
- Lewis, A., & Challinor, A. 2011, *CAMB: Code for Anisotropies in the Microwave Background*, *astrophysics Source Code Library*
- Lia, C., Portinari, L., & Carraro, G. 2002, *MNRAS*, 330, 821
- LSST Science Collaboration, Abell, P. A., Allison, J., et al. 2009, ArXiv e-prints
- Lupton, R., Blanton, M. R., Fekete, G., et al. 2004, *Pub. Astron. Soc. Pac.*, 116, 133
- Marinacci, F., Pakmor, R., & Springel, V. 2014a, *MNRAS*, 437, 1750
- Marinacci, F., Pakmor, R., Springel, V., & Simpson, C. M. 2014b, arXiv:1403.4934
- McCarthy, I. G., Schaye, J., Font, A. S., et al. 2012, *MNRAS*, 427, 379
- McGaugh, S. S. 2012, *Astron. J.*, 143, 40
- McQuinn, M., Lidz, A., Zaldarriaga, M., et al. 2009, *Astrophys. J.*, 694, 842
- Mihos, J. C., & Hernquist, L. 1994, *Astrophys. J.*, 437, 611
- Milgrom, M. 1983, *Astrophys. J.*, 270, 365
- Moore, B., Ghigna, S., Governato, F., et al. 1999, *Astrophys. J. Let.*, 524, L19
- Mosconi, M. B., Tissera, P. B., Lambas, D. G., & Cora, S. A. 2001, *MNRAS*, 325, 34
- Moster, B. P., Naab, T., & White, S. D. M. 2013, *MNRAS*, 428, 3121
- Moustakas, J., Coil, A. L., Aird, J., et al. 2013, *Astrophys. J.*, 767, 50
- Munshi, F., Governato, F., Brooks, A. M., et al. 2013, *Astrophys. J.*, 766, 56
- Navarro, J. F., & White, S. D. M. 1993, *MNRAS*, 265, 271
- Nelson, D., Vogelsberger, M., Genel, S., et al. 2013, *MNRAS*, 429, 3353
- Ocvirk, P., Pichon, C., & Teyssier, R. 2008, *MNRAS*, 390, 1326
- Oesch, P. A., Bouwens, R. J., Illingworth, G. D., et al. 2013, arXiv:1309.2280
- Okamoto, T., Frenk, C. S., Jenkins, A., & Theuns, T. 2010, *MNRAS*, 406, 208
- Okamoto, T., Nemmen, R. S., & Bower, R. G. 2008, *MNRAS*, 385, 161
- Oppenheimer, B. D., & Davé, R. 2008, *MNRAS*, 387, 577
- Pakmor, R., Marinacci, F., & Springel, V. 2014, *Astrophys. J. Let.*, 783, L20
- Peng, Y.-j., Lilly, S. J., Kovač, K., et al. 2010, *Astrophys. J.*, 721, 193
- Perlmutter, S., et al. 1999, *Astrophys. J.*, 517, 565
- Petkova, M., & Springel, V. 2010, *MNRAS*, 410, 1851
- Piontek, F., & Steinmetz, M. 2011, *MNRAS*, 410, 2625
- Pizagno, J., Prada, F., Weinberg, D. H., et al. 2007, *Astron. J.*, 134, 945
- Planck Collaboration, Ade, P. A. R., Aghanim, N., et al. 2013, ArXiv e-prints
- Postman, M., Coe, D., Benítez, N., et al. 2012, *Astrophys. J. Suppl.*, 199, 25
- Predehl, P., Hasinger, G., Böhringer, H., et al. 2006, in *Society of Photo-Optical Instrumentation Engineers (SPIE) Conference Series*, Vol. 6266, *Society of Photo-Optical Instrumentation Engineers (SPIE) Conference Series*
- Puchwein, E., Baldi, M., & Springel, V. 2013, *MNRAS*
- Rahmati, A., Pawlik, A. H., Raicevic, M., & Schaye, J. 2013, *MNRAS*, 430, 2427
- Riess, A. G., Filippenko, A. V., Li, W., et al. 1999, *Astron. J.*, 118, 2675
- Rudd, D. H., Zentner, A. R., & Kravtsov, A. V. 2008, *Astrophys. J.*, 672, 19
- Ruhl, J., Ade, P. A. R., Carlstrom, J. E., et al. 2004, in *Society of Photo-Optical Instrumentation Engineers (SPIE) Conference Series*, Vol. 5498, *Z-Spec: a broadband millimeter-wave grating spectrometer: design, construction, and first cryogenic measurements*, ed. C. M. Bradford, P. A. R. Ade, J. E. Aguirre, J. J. Bock, M. Dragovan, L. Duband, L. Earle, J. Glenn, H. Matsuhara, B. J. Naylor, H. T. Nguyen, M. Yun, & J. Zmuidzinas, 11–29
- Sawala, T., Frenk, C. S., Crain, R. A., et al. 2013, *MNRAS*, 431, 1366
- Sawala, T., Frenk, C. S., Fattahi, A., et al. 2014, arXiv:1404.3724
- Scannapieco, C., Tissera, P. B., White, S. D. M., & Springel, V. 2005, *MNRAS*, 364, 552
- Scannapieco, C., Wadepuhl, M., Parry, O. H., et al. 2012, *MNRAS*, 423, 1726
- Schaye, J., & Dalla Vecchia, C. 2008, *MNRAS*, 383, 1210
- Schaye, J., Dalla Vecchia, C., Booth, C. M., et al. 2010, *MNRAS*, 402, 1536
- Schechter, P. 1976, *Astrophys. J.*, 203, 297
- Seager, S., Sasselov, D. D., & Scott, D. 1999, *Astrophys. J. Let.*, 523, L1
- . 2011, *RECFAST: Calculate the Recombination History of the Universe*, *astrophysics Source Code Library*
- Seljak, U., & Zaldarriaga, M. 1996, *Astrophys. J.*, 469, 437
- Shen, S., Wadsley, J., & Stinson, G. 2010, *MNRAS*, 407, 1581
- Sheth, R. K., & Tormen, G. 1999, *MNRAS*, 308, 119
- Sijacki, D., & Springel, V. 2006, *MNRAS*, 366, 397

- Sijacki, D., Springel, V., Di Matteo, T., & Hernquist, L. 2007, *MNRAS*, 380, 877
- Sijacki, D., Vogelsberger, M., Kereš, D., Springel, V., & Hernquist, L. 2012, *MNRAS*, 424, 2999
- Somerville, R. S., & Primack, J. R. 1999, *MNRAS*, 310, 1087
- Sommer-Larsen, J., Götz, M., & Portinari, L. 2003, *Astrophys. J.*, 596, 47
- Spergel, D., Flauger, R., & Hlozek, R. 2013, arXiv:1312.3313
- Springel, V. 2010, *MNRAS*, 401, 791
- Springel, V., Di Matteo, T., & Hernquist, L. 2005a, *MNRAS*, 361, 776
- Springel, V., & Hernquist, L. 2003a, *MNRAS*, 339, 289
- 2003b, *MNRAS*, 339, 289
- Springel, V., White, S. D. M., Tormen, G., & Kauffmann, G. 2001, *MNRAS*, 328, 726
- Springel, V., White, S. D. M., Jenkins, A., et al. 2005b, *Nature*, 435, 629
- Springel, V., Wang, J., Vogelsberger, M., et al. 2008, *MNRAS*, 391, 1685
- Staneck, R., Rudd, D., & Evrard, A. E. 2009, *MNRAS*, 394, L11
- Steinmetz, M., & Mueller, E. 1994, *A&A*, 281, L97
- Stinson, G., Seth, A., Katz, N., et al. 2006, *MNRAS*, 373, 1074
- Stinson, G. S., Bovy, J., Rix, H.-W., et al. 2013, *MNRAS*, 436, 625
- Sunyaev, R. A., & Zeldovich, I. B. 1980, *ARA&A*, 18, 537
- Teyssier, R., Fromang, S., & Dormy, E. 2006, *Journal of Computational Physics*, 218, 44
- Teyssier, R., Moore, B., Martizzi, D., Dubois, Y., & Mayer, L. 2011, *MNRAS*, 414, 195
- Thacker, R. J., & Couchman, H. M. P. 2000, *Astrophys. J.*, 545, 728
- Thacker, R. J., Scannapieco, E., & Couchman, H. M. P. 2006, *Astrophys. J.*, 653, 86
- Tinker, J., Kravtsov, A. V., Klypin, A., et al. 2008, *Astrophys. J.*, 688, 709
- Tornatore, L., Borgani, S., Dolag, K., & Matteucci, F. 2007, *MNRAS*, 382, 1050
- Torrey, P., Vogelsberger, M., Genel, S., et al. 2014, *MNRAS*, 438, 1985
- Torrey, P., Vogelsberger, M., Sijacki, D., Springel, V., & Hernquist, L. 2012, *MNRAS*, 427, 2224
- Tully, R. B., & Fisher, J. R. 1977, *A&A*, 54, 661
- Velliscig, M., van Daalen, M. P., Schaye, J., et al. 2014, arXiv:1402.4461
- Verheijen, M. A. W. 2001, *Astrophys. J.*, 563, 694
- Vogelsberger, M., Genel, S., Sijacki, D., et al. 2013, *MNRAS*, 436, 3031
- 2014a, *MNRAS*, 438, 3607
- Vogelsberger, M., Sijacki, D., Kereš, D., Springel, V., & Hernquist, L. 2012, *MNRAS*, 425, 3024
- Vogelsberger, M., Genel, S., Springel, V., et al. 2014b, *Nature*, 435, 629
- Warren, M. S., Abazajian, K., Holz, D. E., & Teodoro, L. 2006, *Astrophys. J.*, 646, 881
- Weiner, B. J., Phillips, A. C., Faber, S. M., et al. 2005, *Astrophys. J.*, 620, 595
- Weinmann, S. M., Pasquali, A., Oppenheimer, B. D., et al. 2012, *MNRAS*, 426, 2797
- White, S. D. M. 1996, in *Cosmology and Large Scale Structure*, ed. R. Schaeffer, J. Silk, M. Spiro, & J. Zinn-Justin, 349
- White, S. D. M., & Frenk, C. S. 1991, *Astrophys. J.*, 379, 52
- White, S. D. M., & Rees, M. J. 1978, *MNRAS*, 183, 341
- Wiersma, R. P. C., Schaye, J., & Smith, B. D. 2009a, *MNRAS*, 393, 99
- Wiersma, R. P. C., Schaye, J., Theuns, T., Dalla Vecchia, C., & Tornatore, L. 2009b, *MNRAS*, 399, 574
- Woo, J., Dekel, A., Faber, S. M., et al. 2013, *MNRAS*, 428, 3306
- Wu, H.-Y., Hahn, O., Wechsler, R. H., Mao, Y.-Y., & Behroozi, P. S. 2013, *Astrophys. J.*, 763, 70
- Wu, H.-Y., Zentner, A. R., & Wechsler, R. H. 2010, *Astrophys. J.*, 713, 856
- Xu, G. 1995, *Astrophys. J. Suppl.*, 98, 355
- York, D. G., Adelman, J., Anderson, Jr., J. E., et al. 2000, *Astron. J.*, 120, 1579
- Zahid, H. J., Torrey, P., Vogelsberger, M., et al. 2014, *Ap&SS*, 349, 873
- Zel'dovich, Y. B. 1970, *A&A*, 5, 84